TOWARDS IDENTIFYING DISINFECTANTS AND QUANTIFYING DISINFECTANT LEVELS IN WATER.

TOWARDS IDENTIFYING DISINFECTANTS AND QUANTIFYING DISINFECTANT LEVELS IN WATER.

By MD OMAR SHARIF, B.SC.

A Thesis Submitted to the School of Graduate Studies in Partial Fulfillment of the Requirements for the Degree Master of Science

Department of Chemistry and Chemical Biology, McMaster University.

MASTER OF SCIENCE (August 2017)

TITLE: Towards Identifying Disinfectants and Quantifying Disinfectant Levels in Water.

AUTHOR: Md Omar Sharif

SUPERVISOR: Dr. Peter Kruse

NUMBER OF PAGES: 173, xix

ABSTRACT

Disinfectants are added to the water distribution system and swimming pools to control the growth of pathogenic microorganisms in water. High disinfectant levels are health hazards since they produce disinfectant by-products which are carcinogens. Thus, monitoring the amount of residual disinfectants present and maintaining an optimal amount of residual disinfectants throughout the distribution network is very crucial for safe water distribution. Colorimetric measurements are the current standard for measuring disinfectant levels in water. However, it is very difficult to integrate colorimetric measurements into automated monitoring devices. Redox active molecules like the phenyl-capped aniline tetramer (PCAT) can be incorporated as a dopant into a single wall carbon nanotube sensor for detecting oxidant in drinking water.[1] The sensor works on the principle of oxidizing adsorbed redox molecules on carbon nanotubes by oxidant present in drinking water thus changing the resistivity of the carbon nanotube film. Most commonly used disinfectants are HOCl, Cl_2, ClO_2, Chloramine, $KMnO_4$, HOBr, H_2O_2, O_3, Br_2, I_2, etc. They all are oxidizing agents and can be distinguished from one another as they have different oxidation potentials. For water treatment purposes, it is not enough to know the disinfectant level, but it is also very important to identify which disinfectant is present. Currently, there is no standard method for distinguishing different disinfectants presents in water. The development of sensor arrays based on redox active molecules having different redox potentials is a potential pathway towards differentiating between different disinfectants in water. Different aniline oligomers were synthesized to create a library of redox active molecules. Redox properties of these molecules have been determined, and expected results were

compared with the sensor performance. In the future, these sensors can be incorporated into a reliable, resettable and reagent free sensor array for monitoring and distinguishing different disinfectants in water. Being able to constantly monitor the disinfectant level and identifying the disinfectant present in water will enable us to design an improved and sustainable disinfecting system.

ACKNOWLEDGEMENTS

First of all, I would like to thank my supervisor Dr. Peter Kruse for giving me the opportunity to work under his mentorship. I am very grateful to him for his continuous support, guidance, inspiration and thoughtful discussions.

I would also like to thank Dr. Ravi Selvaganapathy and Dr. David Emslie for their valuable advice and technical supports over two years.

I wish to give my special thanks to the Ana and Caroline for helping me with the experiments and in the completion of this thesis project.

I would like to thank my colleague Amir, Aditya, Ning, Enamul and Tanzina for their support and friendship.

I would like to take this chance and express my indebtedness to three special persons in my life. My younger brother Shamim Osman Arif for all his supports and sacrifices, my uncle Abdul Kader for his guidance during my undergraduate study and my senior Mohammed Fahad Hasan for inspiring me in pursuing the higher study.

I am very grateful to my family for their continuous supports and putting all their trusts in me. I would not be where I am today without them, and I wish to make them happy with more successes.

To my younger brother, Shamim Osman Arif

AND

To my Family

Table of Contents

ABSTRACT ..... **III**

ACKNOWLEDGEMENTS ..... **V**

LIST OF FIGURES ..... **XI**

LIST OF TABLES ..... **XVII**

LIST OF ABBREVIATIONS ..... **XVIII**

DECLARATION OF ACADEMIC ACHIEVEMENT ..... **XIX**

CHAPTER 1: INTRODUCTION **1**

1.1. DISINFECTANTS 1

1.2. DISINFECTANT MONITORING 3

1.3. DISINFECTANT CHEMISTRY 7

1.4. CHEMIRESISTIVE REDOX SENSOR 12

1.5. CHEMIRESISTIVE PH SENSOR 16

1.6. THESIS OVERVIEW 17

CHAPTER 2: CHARACTERIZATION TECHNIQUES **19**

2.1. ELECTROCHEMICAL METHODS AND TECHNIQUES 19

2.1.1. CYCLIC VOLTAMMETRY 19

2.1.2. DIFFERENTIAL PULSE VOLTAMMETRY 22

2.1.3. AQUEOUS VS NON-AQUEOUS REFERENCE ELECTRODE 24

2.2. UV VISIBLE SPECTROSCOPY 25

2.3. CONDUCTIVITY MEASUREMENT 27

2.3.1. TWO PROBE MEASUREMENTS 28

2.3.2. FOUR PROBE MEASUREMENTS 28

CHAPTER 3: SYNTHESIS AND CHARACTERIZATION OF REDOX ACTIVE ANILINE OLIGOMERS AND PYRENATED NEUTRAL RED 30

3.1. INTRODUCTION 30

3.2. SYNTHESIS AND CHARACTERIZATION 33

3.2.1. PHENYL CAPPED ANILINE TETRAMER (PCAT) AND ITS OXIDATION STATES: 33

3.2.1.1. LEUCOEMERALDINE BASE 35

3.2.1.2. EMERALDINE BASE 37

3.2.1.3. PERNIGRANILINE BASE 41

3.2.2. N^1,$N^{1'}$-(ANTHRACENE-9,10-DIYL)-BIS (N^4-PHENYL BENZENE-1,4-DIAMINE) (APCAT) SYNTHESIS: 42

3.2.3. N, N-DIPHENYL-P-PHENYLENEDIAMINE (DPPD) 47

3.2.4. N,N'-DIPHENYL-4,4'-BIPHENYLENEDIAMINE (SDPPD) 48

3.2.5. CRYSTAL VIOLET 49

3.3. NEUTRAL RED DERIVATIVES 50

3.3.1. METHYL PYRENATED NEUTRAL RED 50

3.3.2. PYRENATED NEUTRAL RED 56

CHAPTER 4: ON THE ROLE OF IMPURITIES IN THE ELECTRIC AND SENSING PROPERTIES OF NANOCARBON FILMS 58

4.1. INTRODUCTION 58

4.2. EXPERIMENTAL 59

4.2.1. SENSOR FABRICATION 59

4.2.2. CONDUCTIVITY MEASUREMENT 60

4.2.3. ANALYTE PREPARATION 61

4.3. RESULTS AND DISCUSSION: 61

4.3.1. SENSING COMPARISON 61

4.3.2. ROLE OF PCAT IN SENSING RESPONSE 65

4.3.3. ROLE OF SUBSTRATE FILM THICKNESS 69

4.3.4. EFFECT OF METHANOL 73

4.4. SUMMARY: 75

CHAPTER 5: IDENTIFICATION AND QUANTIFICATION OF DISINFECTANTS BASED ON REDOX CHEMIRESISTIVE SENSORS. 77

5.1. INTRODUCTION 77

5.2. EXPERIMENTAL 79

5.2.1. MATERIALS 79

5.2.2. UV-VIS SPECTROSCOPY 79

5.2.3. ELECTROCHEMISTRY 80

5.2.4. CONDUCTIVITY MEASUREMENT 81

5.2.5. ANALYTE PREPARATION 81

5.2.6. SENSOR PROGRAMMING WITH REDOX-ACTIVE MOLECULE 82

5.3. MOLECULE CHARACTERIZATION 83

5.3.1. HOMO-LUMO GAP FROM UV-VIS 83

5.3.2. ELECTROCHEMICAL CHARACTERIZATION 90

5.3.3. RANKING OF MOLECULE BY EASE OF OXIDATION AND REDUCTION 110

5.4. SENSOR PERFORMANCE 112

5.4.1. SENSOR CALIBRATION AGAINST FREE CHLORINE AND POTASSIUM PERMANGANATE 112

5.4.2. IMPACT OF PH AND ORP ON SENSING RESPONSE 118

5.4.3. Electrochemical Measurement without Reference Electrode? 125
5.4.4. Effect of Buffer 125
5.4.5. Stability of Free Chlorine: 127
5.5. DISTINGUISHING DISINFECTANTS 129
5.5.1. Distinguishing between Free Chlorine and Potassium Permanganate 129
5.5.2. DPPD as possible pH sensor 138
5.5.3. Distinguishing between Free Chlorine and Hydrogen Peroxide 140
5.6. SUMMARY 142
CHAPTER 6: SUMMARY AND FUTURE WORK 144
6.1. SUMMARY 144
6.2. FUTURE WORK 145
BIBLIOGRAPHY 147
APPENDIX 1: STANDARD OPERATING PROCEDURE FOR SENSOR FABRICATION 160
APPENDIX 2: STANDARD OPERATING PROCEDURE FOR SENSOR MEASUREMENT 168

LIST OF FIGURES

Figure 1: Hach Pocket Colorimeter™ II kit for measuring chlorine concentration. (Image source: Hach) 4

Figure 2 : Rio Olympic green swimming pool, 2016 (Source: Adam Pretty/Getty Images, used with permission from Adam Pretty) 6

Figure 3: Distribution of $HOCl/OCl^-$ at different pH (Source: Dr. David A. Reckhow, used with permission) 8

Figure 4: Relation between free chlorine concentration, ORP, and pH (Source: Santa Barbara Control Systems) 10

Figure 5: ORP values for different disinfectants at different concentration. (Source: DOI: http://dx.doi.org/10.5942/jawwa.2014.106.0002) 11

Figure 6: Colorimetric DPD method reaction 12

Figure 7: Schematic mechanism of nanotube based redox chemiresistive sensor for measuring oxidizing agents. 14

Figure 8: Cyclic voltammogram of ferrocene 21

Figure 9: Differential Pulse Voltammetry waveform (Source: Bioanalytical Systems, Inc.) 22

Figure 10: Ferrocene differential pulse voltammogram oxidation peak 23

Figure 11: Possible electron transition in UV-Visible spectroscopy 26

Figure 12: UV–VIS spectrum of phenyl/phenyl end-capped tetra aniline in the emeraldine oxidation state in DMSO solution.[58] 27

Figure 13: Two probe measurement terminal set up 28

Figure 14: Four probe measurement terminal set up 29

Figure 15: Schematic of C-N cross coupling reaction 30

Figure 16: Redox active molecules 31

Figure 17: Pyrenated neutral red derivatives 32

Figure 18: Synthesis of Phenyl Capped Aniline Tetramer in its leucoemeraldine state 33

Figure 19: Mass spectrum of PCAT leucoemeraldine base 35

Figure 20: 1-H NMR spectrum of leucoemeraldine base 36

Figure 21: ^{1}H NMR Spectrum of leucoemeraldine base elaborated 37

Figure 22: ^{1}H NMR spectrum of PCAT emeraldine base 39

Figure 23: ^{1}H NMR peak integration of PCAT emeraldine base and leucoemeraldine base 40

Figure 24: Mass spectrum of PCAT pernigraniline base 40

Figure 25: ^{1}H NMR spectrum of PCAT emeraldine base 41

Figure 26: Synthesis of Anthracene substituted Phenyl Capped Aniline Tetramer 42

Figure 27: Mass spectrum of synthesized APCAT 44

Figure 28: ^{1}H NMR spectrum of synthesized APACT 45

Figure 29: UV spectra of PCAT and APCAT emeraldine base 46

Figure 30: ^{1}H NMR spectrum of DPPD 47

Figure 31: ^{1}H NMR spectrum of SDPPD 48

Figure 32: ^{1}H NMR spectrum of Crystal Violet 49

Figure 33: Synthesis of methyl pyrenated neutral red 51

Figure 34: Mass spectrum of methyl pyrenated neutral red 51

Figure 35: ^{1}H-MMR spectrum of methyl pyrenated neutral red.....52

Figure 36: ^{1}H NMR spectrum of neutral red base 53

Figure 37: ^{1}H NMR spectra comparison of neutral red derivative (black) and neutral red (red).....54

Figure 38: UV-Vis spectroscopy comparison of neutral red and neutral red derivative ...55

Figure 39: Synthesis of pyrenated neutral red 56

Figure 40: Mass spectrum of pyrenated neutral red derivative.....57

Figure 41: 1H NMR spectroscopy of pyrenated neutral red derivate 57

Figure 43: Comparison of blank and PCAT sensors from HiPco PO257 SWCNT.....62

Figure 44: Sensing comparison of TUBALL carbon nanotubes blank and PCAT sensors 63

Figure 45: Sensing comparison from 95% semiconducting SWCNT blank and PCAT sensors.....64

Figure 46: Sensing comparison between three different nanocarbon substrates with PCAT 68

Figure 47: Sensing response comparison of a thin film carbon nanotube sensors 69

Figure 48: Morphology of a thick carbon nanotube film. A) Bulk film morphology, B) Aggregated nanotube bundles on the surface, C) Nanotube bundles, D) Nanotube film morphology at the contact.....71

Figure 49: Effect of film thickness on the time constant of sensing response.....73

Figure 50: Sensing response comparison of HiPco PO343 SWCNT blank with and without methanol contact.....74

Figure 51: Redox active molecules 78

Figure 52: Sensor programming with redox active molecule 82

Figure 53: UV-Vis spectrum of DPPD in acetonitrile. 84

Figure 54: UV-Vis spectrum of SDPPD in acetonitrile. 85

Figure 55: UV-Vis spectrum of Leucoemeraldine PCAT base in acetonitrile. 86

Figure 56: UV-Vis spectrum of emeraldine PCAT base in acetonitrile. 87

Figure 57: UV-Vis spectrum of emeraldine APCAT base in acetonitrile. 88

Figure 58: UV-Vis spectrum of crystal violet in acetonitrile 89

Figure 59: Cyclic voltammogram of PCAT in acetonitrile 90

Figure 60: PCAT redox process mechanism 92

Figure 61: Differential pulse voltammogram oxidation scan of PCAT in acetonitrile 93

Figure 62: Differential pulse voltammogram reduction scan of PCAT in acetonitrile 94

Figure 63: Cyclic voltammogram of DPPD in acetonitrile 95

Figure 64: DPPD redox process mechanism 96

Figure 65: Differential pulse voltammogram oxidation scan of DPPD in acetonitrile 97

Figure 66: Differential pulse voltammogram reduction scan of DPPD in acetonitrile 98

Figure 67: Cyclic voltammogram of SDPPD in acetonitrile 99

Figure 68: SDPPD redox process mechanism 100

Figure 69: Differential pulse voltammogram oxidation scan of SDPPD in acetonitrile 101

Figure 70: Differential pulse voltammogram reduction scan of SDPPD in acetonitrile 102

Figure 71: Cyclic voltammetry of APCAT in acetonitrile 103

Figure 72: Differential pulse voltammogram oxidation scan of APCAT in acetonitrile 104

Figure 73: APCAT redox process mechanism.....105

Figure 74: Differential pulse voltammogram reduction scan of APCAT in acetonitrile.106

Figure 75: Cyclic voltammogram of Crystal Violet in acetonitrile 107

Figure 76: Differential pulse voltammogram oxidation scan of Crystal Violet in acetonitrile.....108

Figure 77: Differential pulse voltammogram oxidation scan of PCAT in acetonitrile....109

Figure 78: Crystal Violet redox process mechanism 110

Figure 79: PCAT sensing response for two different disinfectants 112

Figure 80: DPPD sensing response for two different disinfectants 114

Figure 81: SDPPD sensing response for two different disinfectants 115

Figure 82: APCAT sensing response for two different disinfectants 116

Figure 83: Crystal violet sensing response for two different disinfectants.....117

Figure 84: PCAT sensor response for 1 ppm free chlorine and 1 ppm KMnO4 at different pH.....119

Figure 85: DPPD sensor response for 1 ppm free chlorine and 1 ppm KMnO4 at different pH.....121

Figure 86: SDPPD sensor response for 1 ppm free chlorine and 1 ppm KMnO4 at different pH. 122

Figure 87: APCAT sensor response for 1 ppm free chlorine and 1 ppm KMnO4 at different pH 123

Figure 88: Crystal Violet sensor response for 1 ppm free chlorine and 1 ppm KMnO4 at different pH 124

Figure 89: Current measurement for different buffer concentration.....126

Figure 90: Comparison of sensing response for pH and buffer concentration 127

Figure 91: Relationship between sensor response and measured ORP values for free chlorine and $KMnO_4$ analytes 130

Figure 92: Relationship between sensor response and literature ORP values for free chlorine and $KMnO_4$ analytes 131

Figure 93: Relationship between the deviation from ORP and oxidation potential for measured ORP values 132

Figure 94: Relationship between the deviation from ORP and oxidation potential for literature ORP values 133

Figure 95: pH sensing comparison of DPPD sensor and pristine carbon nanotubes.....139

Figure 96: PCAT sensor response for hydrogen peroxide and free chlorine.....141

Figure 97: Emeraldine APCAT sensor response for hydrogen peroxide and free chlorine 142

Figure 42: Keithley 2450 SourceMeter user interface.....172

LIST OF TABLES

Table 1: Standard electrode potentials of some common disinfectants 7

Table 2: Differential pulse voltammetry peaks for different redox active molecule. 110

Table 3: Measured and literature ORP values for different analytes. 129

Table 4: Characteristic constants for different disinfectants 135

Table 5: Stability of free chlorine and oxidation reduction potential of analyte. 128

LIST OF ABBREVIATIONS

APCAT	Anthracene substituted Phenyl Capped Aniline Tetramer
CV	Cyclic Voltammetry
DPD	N, N-diethyl-p-phenylenediamine
DPPD	N, N-Diphenyl-p-phenylenediamine
DPV	Differential Pulse Voltammetry
EPA	Environmental Protection Agency
HOMO	Highest Occupied Molecular Orbital
LUMO	Lowest Unoccupied Molecular Orbital
NR	Neutral Red
ORP	Oxidation Reduction Potential
PCAT	Phenyl Capped Aniline Tetramer
ppm	parts per million
SDPPD	N, N′-Diphenyl benzidine
SOP	Standard Operating Procedure
TBAP	Tert Butyl Ammonium Perchlorate
UV-Vis	Ultra Violet-Visible

DECLARATION OF ACADEMIC ACHIEVEMENT

The research work presented here was conducted at the Department of Chemistry and Chemical Biology, McMaster University between September 2015 to August 2017. The experimental work in chapter 4 was done by me and by Ana Zubiarrain Laserna under my supervision. The chapter 5 experimental was done by me and by Caroline Wojnas under my supervision. Appendix 1 is reprinted from the work of Dr. Aditya Aryasomayajula with his permission. All the experimental design and data analysis were done by me. No part of this research work has been submitted previously for a degree.

CHAPTER 1: INTRODUCTION

1.1. DISINFECTANTS

Water is the most important resource for life, and water safety is directly related to public health. Residual disinfectant concentration is an important water quality parameter. Disinfectants are added to drinking water, swimming pool and spa water, wastewater etc. Any natural source of water - whether it is ground water or lake water - must go through a treatment procedure before it is considered safe to use. Disinfectants are used for deactivation and destruction of pathogenic microorganisms during the water purification process at water treatment facilities. Disinfectants are also added to the treated water during water distribution ("residual disinfectant") to inhibit the regrowth of microorganisms. Overall, disinfectants make water biologically stable and pathogen free.[2,3]

Chemical disinfectants are historically used for disinfecting water. Of these, chlorine is the most widely used chemical disinfectant for water treatment. Chlorine is either used as liquefied chlorine gas or as sodium hypochlorite solution. Other chemical disinfectants are ClO_2, Chloramines, Br_2, I_2, H_2O_2, O_3, and $KMnO_4$. Use of disinfectant is regulated due to the formation of disinfectant by-products.[4] Disinfectants react with organic compounds present in the water and create disinfectant by-products. Disinfectant by-products are health hazards and to minimize the by-product formation an optimal level of disinfectants is used in water.[5,6] The most well-known disinfectant by-products are trihalomethane (THM) compounds and they are carcinogens.[7,8] Disinfectants are added during two stages, at the primary stage during water treatment to destroy pathogens, and at

the secondary stage at the distribution inlet to attain the appropriate residual disinfectant concentration. Chlorine is commonly used both as a primary disinfectant and a secondary disinfectant. There are alternatives to chlorine as primary disinfectants to minimize the production of disinfectant by-products. Ozone is very effective as a primary disinfectant and has the benefit of removing organic micropollutants from the water.[9] Among the non-chemical disinfectants, UV has been used for many years in drinking water and wastewater treatment.[10] UV is becoming more popular as it reduces the use of chemical disinfectants thus minimizing the potential for by-product formation.[11] UV disinfection is not suitable for water distribution as it doesn't provide any residual disinfectants. There are several key factors that influence the selection of a disinfectant:[12]

- The effectiveness of the disinfectant in destroying pathogens of concern;
- The quality of the water to be disinfected;
- The formation of undesirable by-products as a result of disinfection;
- The ability to easily verify the operation of the chosen disinfection system by reference to system validation, collation of monitoring data and alarm generation;
- The ease of handling, and health and safety implications of a disinfectant;
- The preceding treatment processes;
- The overall cost.

Disinfectant regulations consider disinfectant depletion in water distribution system besides potential disinfectant by-product formation. Disinfectant depletion is very common, and maintaining an optimal level of residual disinfectant is very crucial to inhibit the regrowth of pathogens.[13] Disinfectants can deplete for several reasons. Disinfectants are oxidizing agents and strong electron acceptors thus they can react easily. For example, the presence of a biofilm in the water distribution network may cause disinfectant depletion.[14,15] Other factors such as photodegradation, pH, and temperature also play a role in disinfectant depletion.

1.2. DISINFECTANT MONITORING

Insufficient disinfectants could lead to regrowth of pathogens during the water distribution which imposes a serious risk to human health.[16] Therefore, it is necessary to monitor the residual disinfectants in the water stream. Monitoring is mainly done at the treatment facilities where the water enters the supply line, and at several point locations within the distribution network. The monitoring method depends mainly on the type of disinfectant used to treat the water. Colorimetric, titrimetric, and electrochemical methods are most commonly used for disinfectant monitoring. Among the different disinfectant monitoring methods, chlorine monitoring is most developed. There are several EPA-approved analytical techniques for monitoring chlorine.[17] The most common techniques are DPD colorimetric, DPD ferrous and amperometric methods. There are other established methods for monitoring different disinfectants.[12] For example, DPD reagent, Lissamine Green B, and amperometric methods are used for monitoring chlorine dioxide. The thiosulfate titration method is used for hydrogen peroxide monitoring, and a spectroscopic method is

available for potassium permanganate. UV disinfectant monitoring is usually done by measuring the intensity of UV lamp. Also, monitoring the micro-organisms in the supplied water gives an assessment of disinfectant levels in water.

Figure 1: Hach Pocket Colorimeter™ II kit for measuring chlorine concentration. (Image source: Hach)

Even though there are several well-developed methods for monitoring disinfectants, there are some drawbacks of these methods for effective disinfectant monitoring. For example, the chlorine DPD method is a colorimetric method and needs spectroscopic readout devices. Spectroscopic analysis methods suffer from interference from turbidity and organic content present in water. The DPD method also experiences interference from oxidized manganese, which can give misleading results. The DPD Ferrous method is a titrimetric method and needs a laboratory to do the analysis. This is a time-consuming

process and none of these colorimetric and titrimetric methods are suitable for automated disinfectant monitoring. Electrochemical methods are useful for automated monitoring, but they need reference electrodes. Reference electrodes are not very reliable for long periods of time. Therefore, there is a significant need for a reliable monitoring system that will be cheap, easy to handle and automated.

The lack of proper disinfectant monitoring systems poses a serious public health risk. Two examples of poorly monitored disinfectant systems are discussed here. The first is the Walkerton Tragedy, which happened in Walkerton, Ontario in May 2000.[18] The underground water reservoir well was contaminated with two pathogens. These were *E. Coli* O157: H7 and *Campylobacter jejuni* from nearby agricultural runoff due to heavy flooding. Even though the routine chlorinator was on, it was not enough to kill the large incoming pathogen contamination. The consequence was a pathogen outbreak throughout the water distribution network. Severe bloody diarrhea and other gastrointestinal infections were seen from drinking contaminated water. The consequence was 5 people dead, and 2,500 people ill with different gastrointestinal diseases. After investigating this catastrophic event, it was found that there was a severe lack of due diligence in disinfectant monitoring.[18] This event heightened public awareness of the importance of constant drinking water quality monitoring, and illustrated the need for a real-time automated monitoring system.

Another recent example of a poorly monitored disinfection system is the Rio 2016 Olympics' green swimming pool. According to Olympic officials, 160 liters of hydrogen

peroxide was mistakenly added to a chlorinated swimming pool without knowing which disinfectant was used for the pool disinfection. Hydrogen peroxide and sodium hypochlorite react with each other to produce oxygen, sodium chloride, and water. The consequence was hydrogen peroxide disabling the residual chlorine in the pool, and there was not enough disinfectant to inhibit the regrowth of microorganism. The swimming pool was an outdoor swimming pool and the athletes were already using the pool. Thus, there was enough biological matter in the pool to proliferate the growth of green algae, causing the pool turning green. This story emphasizes the importance of distinguishing between various disinfectants, in addition to constant monitoring.

Figure 2 : Rio Olympic green swimming pool, 2016 (Source: Adam Pretty/Getty Images, used with permission from Adam Pretty)

1.3. DISINFECTANT CHEMISTRY

pH is a very important water quality parameter which plays a significant role in disinfectant chemistry and must be reported with disinfectant monitoring. In general, disinfectant chemistry is complex, and the oxidizing power of most of the disinfectants depends on pH. Disinfectants undergo different reactions based on pH. Examples of pH dependent oxidation reactions are shown in Table 1. The standard half reaction potentials given are relative to hydrogen at standard conditions which are defined as 1 M concentration of each participating chemical species, 1 atm pressure and 25 °C temperature. The half reaction potential is the 'potential' of a chemical species of losing or gaining electrons at an electrode.

Table 1: Standard electrode potentials of some common disinfectants

Disinfectant	Reduction half reaction	Standard Potential
Hypochlorous acid	$HOCl + H^+ + 2e^- \longrightarrow Cl^- + H_2O$	$E^o = 1.49V$
Hypochlorite	$OCl^- + H_2O + 2e^- \longrightarrow Cl^- + 2OH^-$	$E^o = 0.9V$
Monochloramine (acidic)	$NH_3Cl^+ + H^+ + 2e^- \longrightarrow Cl^- + NH_4^+$	$E^o = 1.4V$
Monochloramine (basic)	$NH_2Cl + 2H_2O + 4e^- \longrightarrow Cl^- + NH_3 + 2OH^-$	$E^o = 0.75V$
Permanganate (acidic)	$MnO_4^- + 8H^+ + 5e^- \longrightarrow Mn^{2+} + 4H_2O$	$E^o = 1.49V$
Permanganate (basic)	$MnO_4^- + 2H_2O + 3e^- \longrightarrow MnO_2 + 4OH^-$	$E^o = 0.58V$
Hydrogen Peroxide (acidic)	$H_2O_2 + 2H^+ + 2e^- \longrightarrow 2H_2O$	$E^o = 1.76V$
Hydrogen Peroxide (basic)	$HO_2^- + H_2O + 2e^- \longrightarrow 3OH^-$	$E^o = 0.87V$

Disinfectants dissociate into different active species at different pH. For example, HOCl is a weak acid and dissociates in water depending on the pH. The distribution of HOCl and OCl^- is shown in Figure 3. It shows that OCl^- is the dominant species at high pH and at low pH the dominant species is HOCl.

$$HOCl \rightleftharpoons OCl^- + H^+$$

$$K_{HOCl} = \frac{[OCl^-][H^+]}{[HOCl]}$$

$K_{HOCl} = 5.6 \times 10^{-8}$ at 25°C

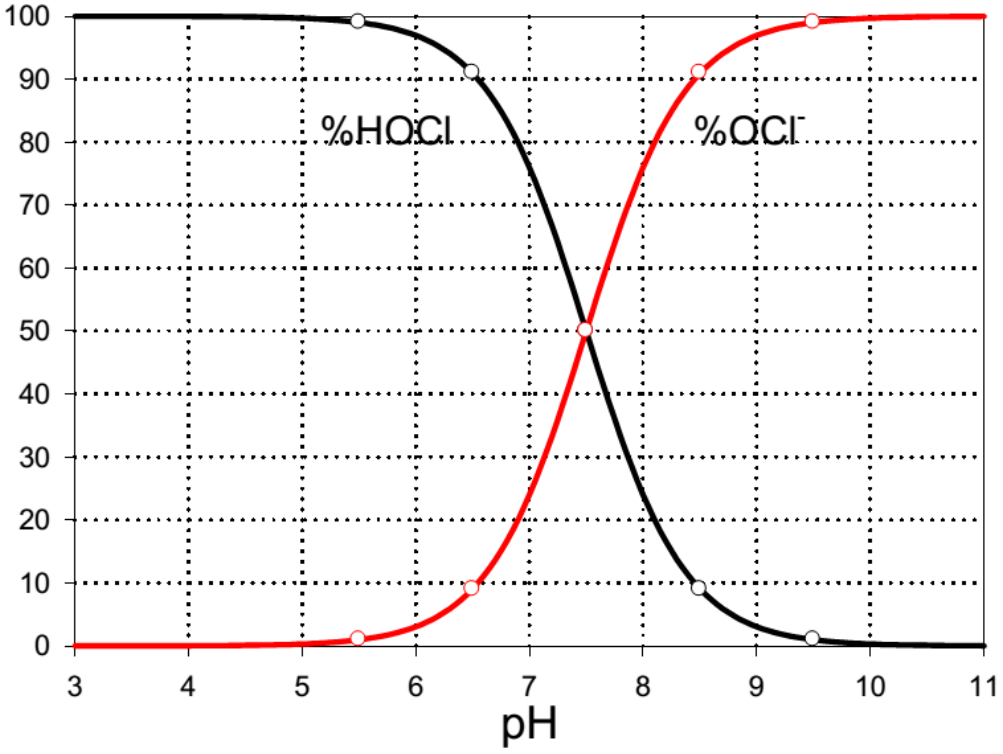

Figure 3: Distribution of HOCl/OCl^- at different pH (Source: Dr. David A. Reckhow, used with permission)

Another very important parameter along with pH is the oxidation reduction potential (ORP) of disinfectants. All disinfectants are oxidizing agents with different redox potentials. It has been debated in the literature whether disinfectant concentration or the power of the disinfectant should be measured?[19] Power of disinfectant can be quantified by measuring the oxidation reduction potential (ORP) of a solution which is associated with the pH and the concentration of the disinfectant.[20,21] ORP measurement is an electrochemical method for measuring disinfectant power in aqueous media. It works based on the potential difference between a platinum working electrode and a reference electrode. ORP behavior at an electrode can be explained with the Nernst equation.

$$E_{mv} = E_o + 2.3026\frac{RT}{nF}\log\frac{[\text{Oxidizer}]^o}{[\text{Reducer}]^r}$$

o, r = stoichiometric coefficient

For the hypochlorous acid oxidation reaction, the Nernst equation can be written as follows

$$HOCl + H^+ + 2e \longrightarrow Cl^- + H_2O$$

$$E_{mv} = E_o + 29.58\log\frac{[HOCl][H^+]}{[Cl^-]}$$

The relation between HOCl concentration and pH can be rearranged which shows that at a constant concentration with a change in pH the oxidation potential changes.

$$E_{mv} = E_o + 29.58\log[HOCl] - 29.58pH - 29.58\log[Cl^-]$$

The relation between ORP, ppm, and pH for free chlorine is shown below in Figure 4. The figure shows the change in ORP value for both pH and different chlorine concentration.

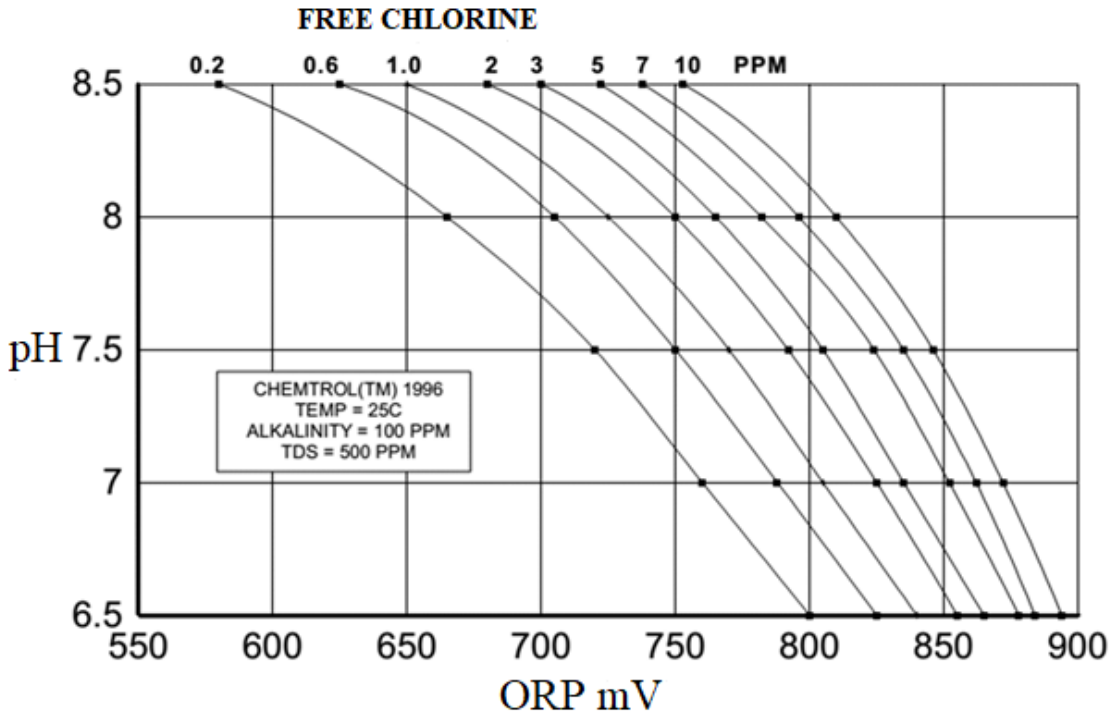

Figure 4: Relation between free chlorine concentration, ORP, and pH (Source: Santa Barbara Control Systems)

Based on the ORP values of a disinfectant solution it is possible to differentiate between different disinfectants. A typical sensor response for different disinfectants from ORP measurements is shown in Figure 5.

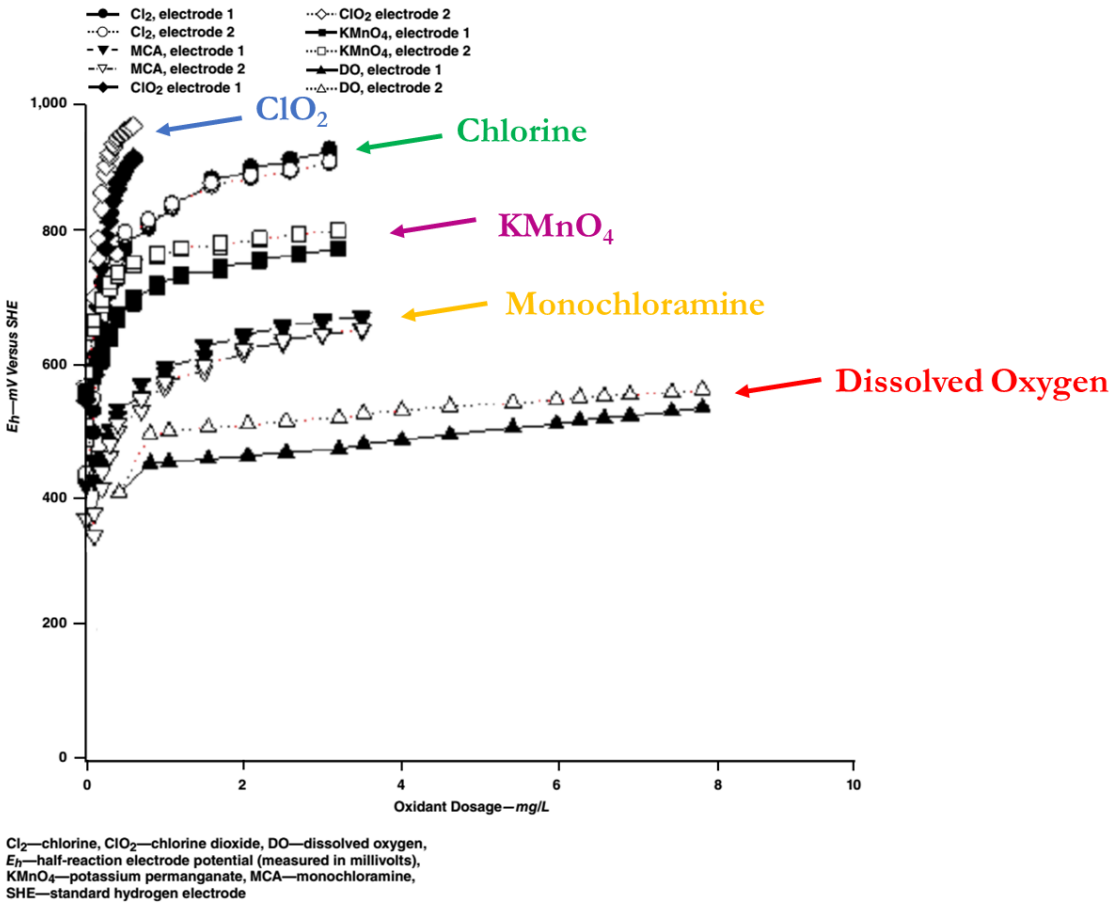

Figure 5: ORP values for different disinfectants at different concentration. (Source: DOI: http://dx.doi.org/10.5942/jawwa.2014.106.0002)

1.4. CHEMIRESISTIVE REDOX SENSOR

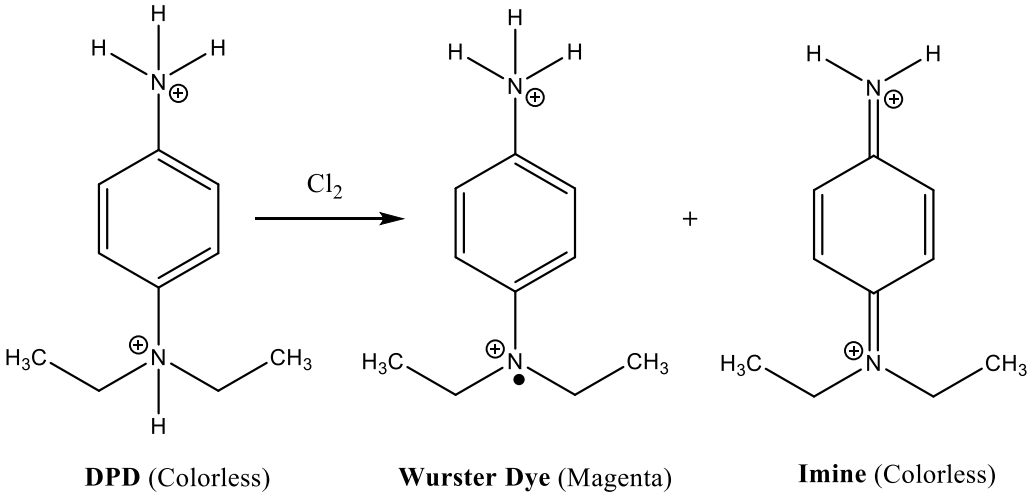

Figure 6: Colorimetric DPD method reaction

The DPD colorimetric method uses a redox indicator N,N-Diethyl-*p*-phenylenediamine for chlorine measurement and the change of redox behavior is measured spectroscopically. It should be advantageous to be able to measure the change of redox potential at the surface of a nanoelectronic device. Nanoelectronics has seen many application based on devices made from single or few molecules.[22] Redox-active molecules have device-like functionalities, leading to many potential applications such as molecular switches,[23–25] logic gates,[26] memory elements,[27] sensors[28–30] etc. Most common redox-active species are conjugated polymers with redox-active groups, rotaxanes, ferrocenes and coordination complexes.[26–34] These molecules are very responsive to outside stimuli and can be switched controllably and reversibly between the different oxidation states both chemically and electrochemically. Commonly these molecules are incorporated into electrode surfaces or adsorbed onto different substrates to act as molecular devices.

Redox-active molecules have been used for switchable carbon nanotube doping and could be a potential lead in sensing redox agents.[35]

Polyanilines are a class of redox active conjugated polymers which has seen applications in the fields of electroluminescence, photovoltaic cells, field effect transistors, corrosion inhibition, sensors etc.[36–41] Polyaniline has characteristics of both of an organic polymer and a semiconductor. However, polyaniline is difficult to use in nano devices due to its poor solubility and poor processability. Oligoanilines have similar properties and applications as polyaniline. The conjugated oligomers have several advantages in terms of control and synthesis which make them more favorable for use in nanodevices. Additionally, oligomers are easier to engineer, and they have defined physical and chemical properties.

Carbon nanotubes and two-dimensional materials like graphene are promising substrates for incorporating aniline oligomers into molecular devices. These substrates have some exceptional structural and electronic properties and have seen many applications in the fields of nanoelectronics, field effect transistors etc.[42–44] Carbon nanotubes are usually metallic or semiconducting with a narrow bandgap. A small change in doping characteristics changes the resistance of the carbon nanotube films. Studies have been done on carbon nanotube and polyaniline doping for several potential applications. Researchers have reported carbon nanotube doped polyaniline and carbon nanotube/polyaniline composites for possible applications as biosensor[45] and gas sensors.[46,47] It has been shown that a charge transfer complex forms between the nanotube and polyaniline.[35]

The likely interactions of aniline oligomers and substrates will be noncovalent functionalization and a charge transfer complex. Carbon nanotubes are reported to behave as electron acceptors whereas the behavior of the oligoanilines differs based on the oxidation states. For example, oligoaniline in the leucoemeraldine state is a good electron donor and n-dopes carbon nanotubes. In the leucoemeraldine state oligoanilines are structurally amine chain. In contrast, the emeraldine base acts as a p-dopant. In the emeraldine state oligoanilines contain equal amounts of amine and imine group. Based on the differential doping of carbon nanotubes by the different forms of the oligoanilines our group has reported a carbon nanotube based chemiresistive sensor for measuring free chlorine concentration in drinking water.[1]

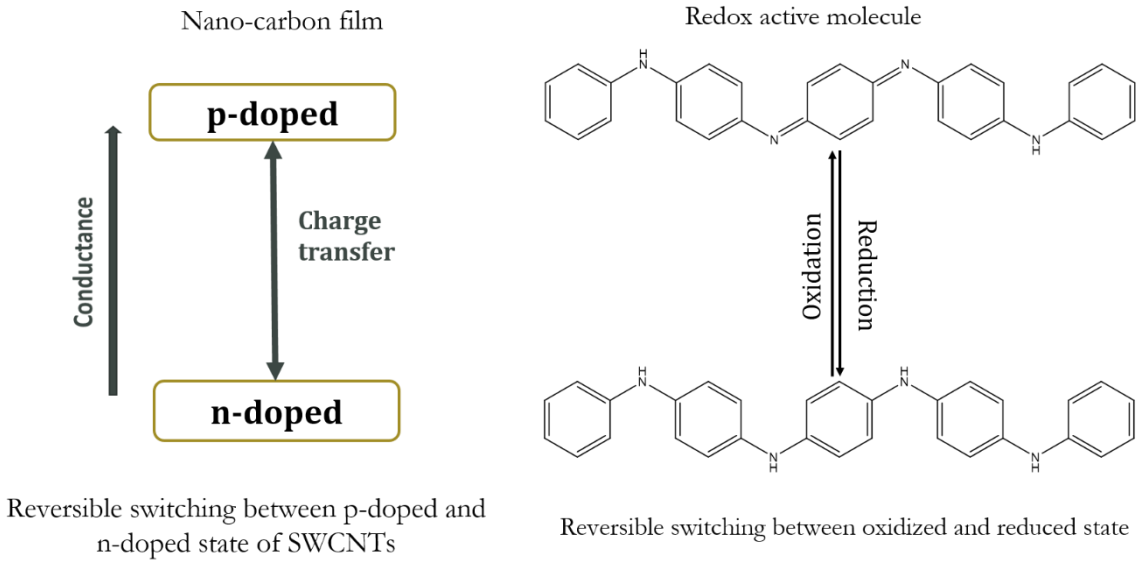

Figure 7: Schematic mechanism of nanotube based redox chemiresistive sensor for measuring oxidizing agents.

The sensor is fabricated from a functionalized carbon nanotube film. Nanotubes are functionalized non-covalently by redox active oligoaniline. When analytes with oxidizing agents are exposed to oligoaniline functionalized carbon nanotubes, the oligoanilines get oxidized. Changes in oxidation states change the doping characteristics which changes the electronic behavior of the nanotubes. The change in resistance of the nanotubes film is associated with the presence of an oxidizing agent in the water. The change in film resistance is found to be in a logarithmic relation with the concentration of the disinfectant present. The sensor is a reagent free sensor and can be regenerated both electrochemically and chemically.

My aim for this M.Sc. thesis is to work towards identification and quantification of disinfectants using a redox chemiresistive sensor. Oligoanilines are active molecules for our sensor and all the disinfectants differ in their redox potential. A sensor array with different redox active molecules having different redox potentials could be a way to differentiate between different disinfectants. If an oxidizing agent is not strong enough to oxidize a particular redox active molecule we expect it to have no sensing response. On the other hand, a stronger oxidizing agent will get a response from most sensors. Our goal is to work towards making a sensor array which will behave like a redox potential scale. Studies will also be done to quantify sensor behavior with regards to disinfectant chemistry at different pH.

1.5. CHEMIRESISTIVE pH SENSOR

pH has a significant role in disinfectant chemistry and it is necessary to monitor pH while monitoring the disinfectant. Electrochemical and fluorescence methods are commonly used for the pH measurement.[48–51] Electrochemical pH meters need frequent calibration and are very sensitive to other interfering metal ions present in the solution. Optical methods are not always reliable due to inaccuracies from the readout devices. There is a substantial need for a low-cost reliable pH measurement method.

Immobilization of pH indicators onto different substrates was tried before for optical pH sensing and this is the most promising pathway towards a low-cost reliable pH sensor.[52] Immobilized pH indicator on a carbon nanotube film and conductivity measurement of that film could be our potential lead to a pH sensor. pH indicators work on the principle of acid base switching depending on the pH of the solution. An interesting indicator is Neutral Red (NR) which has a pH range of 6.8 to 8 and a conjugated system which may facilitate adsorption onto carbon nanotubes. If we could use the idea of charge transfer between the acid and conjugated base adsorbed on the carbon nanotubes, therefore, we will be able to measure the pH of a solution.

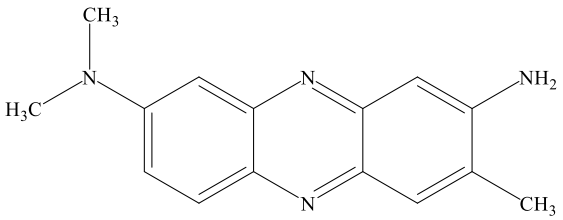

Neutral Red

Experiments were done by another group member to prove the principle of chemiresistive pH measurement and they showed satisfactory results with one drawback. Even though the sensor initially works fine, it stops working after several runs. The reason may be that NR is washed off from the sensor due to the protonated forms of NR having insufficient binding interactions with the carbon nanotubes. It is our goal to engineer the NR molecule for better π-π interactions with the nanotubes for a chemiresistive pH sensor. The pH sensor will be integrated with our proposed redox sensor array for total disinfectant monitoring.

1.6. THESIS OVERVIEW

Chapter 1 gives a brief overview of the role of disinfectants used for water treatment, the importance of constant disinfectant monitoring and importance of differentiating between the disinfectants. The importance of pH monitoring is also illustrated with the effect of pH in disinfectant chemistry. Our approach to disinfectant monitoring and the sensing mechanism is explained in this chapter. Chapter 2 discusses two commonly used electrochemical analysis methods: Cyclic voltammetry and differential pulse voltammetry, as well as UV-Vis spectroscopic analysis and the conductivity measurement. The C-N coupling synthesis of some redox active molecules and pH indicator neutral red derivatives are discussed in chapter 3, including their characterization. Chapter 4 discusses selecting suitable sensor substrate materials for studying the interaction with redox-active molecules. Substrate film thickness, redox active molecule interactions with the substrate and the role of impurities present in the substrate are explored in this chapter. Chapter 5 details the results of sensor performance for redox-active molecules against two different

disinfectants. Possibilities of differentiating between disinfectants and a pH sensor application will also be discussed. In chapter 6, a summary of the thesis and discussion of future work will be given. Standard Operating Procedures (SOP) for sensor fabrication and for sensor measurement are given in Appendix 1 and Appendix 2.

CHAPTER 2: CHARACTERIZATION TECHNIQUES

2.1. ELECTROCHEMICAL METHODS AND TECHNIQUES

The electrochemical analysis gives valuable information on the quantitative determination of metal ions, oxidation-reduction processes, and complex formation of a chemical species. The electrochemical analysis is widely used in the field of quantitative determination of metal ions and organic compounds, studies of redox potentials and reaction kinetics. Several methods are well-developed for electrochemical analysis. We will discuss the two most common voltammetric methods cyclic voltammetry and differential pulse voltammetry.[53,54] Both of these methods were used to characterize the redox-active molecules studied in this thesis.

2.1.1. CYCLIC VOLTAMMETRY

Cyclic voltammetry is a widely used electrochemical analytical tool for characterizing redox active molecules.[55,56] This will give useful information about the electron transfer processes during a redox reaction as well as redox potentials. Cyclic voltammetry is usually done in an electrochemical cell with three electrodes immersed in an unstirred analyte and nonreactive supporting electrolyte. Among the electrodes, one is the working electrode (usually platinum, gold or glassy carbon) where the oxidation-reduction reactions occur. Common reference electrodes are the standard hydrogen electrode, $Ag/AgNO_3$, Ag/AgCl or the saturated calomel electrode (i.e., Hg/Hg_2Cl_2) which all provide a potential calibration against the working electrode. The standard hydrogen electrode is very difficult to use, hence the most common reference electrodes are Ag/AgCl and saturated calomel electrode.

The third one is a counter electrode which is normally a platinum wire to facilitate the current flow from the working electrode. A potential is applied across the working and reference electrodes which is called *excitation signal* and the current that is measured across the working electrode and counter electrode can be regarded as the *response signal*. A potential sweep is done reversibly and the current is measured during the potential change. A typical voltammogram is shown in Figure 8.

The important parameters in cyclic voltammetry are anodic peak current i_{pa}, cathodic peak current i_{pc}, anodic peak potential E_{pa} and cathodic peak potential E_{pc}. These parameters are labeled in a voltammogram. For a reversible redox couple, the average of cathodic and anodic peak is usually used to calculate the formal reduction potential.

$$E^{\circ}{}_{1/2} = \frac{E_{pa} + E_{pc}}{2}$$

This approximation is accurate when the electron transfer process is reversible and the diffusion coefficients for oxidizing and reducing species are the same. The number of electrons transferred in a redox reaction for a reversible couple can be calculated from the peak separation.

$$\Delta E_p = E_{pa} - E_{pc} \cong \frac{0.059}{n}\,\mathrm{V}$$

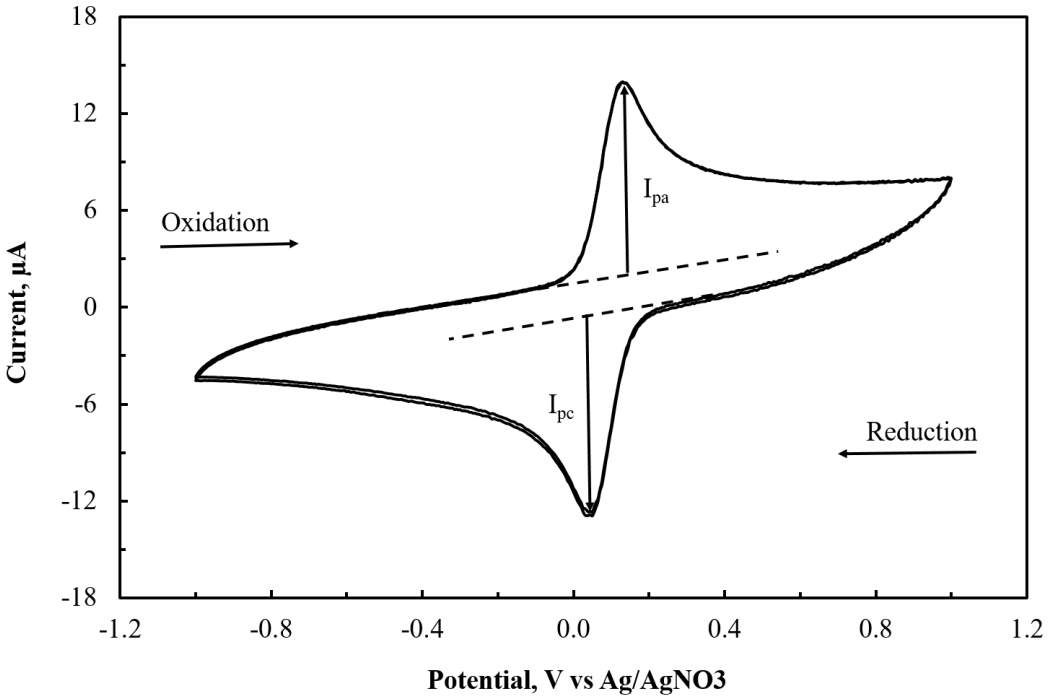

Figure 8: Cyclic voltammogram of ferrocene

The peak current for a reversible system is described by the *Randles-Sevcik* equation for the forward sweep,

$$i_p = 2.69\times10^5 n^{3/2} A D^{1/2} C v^{1/2}$$

Where i_p is peak current is (A), *n* is number of electron. *A* is electrode surface (cm^2), *D* is diffusion constant (cm^2/s), *C* is concentration (mol/cm^3) *v* is scan rate (V/s). Accordingly, i_p increases with $v^{1/2}$ and proportional to concentration.

2.1.2. DIFFERENTIAL PULSE VOLTAMMETRY

Differential pulse voltammetry (DPV) is more sensitive than cyclic voltammetry and extremely useful to detect trace levels of organic and inorganic analytes. DPV was developed from linear sweep voltammetry and staircase voltammetry. In this technique, small constant amplitude potential pulses are superimposed upon a staircase waveform of constant height. The potential wave form for DPV is shown in Figure 9. The current is measured immediately before the pulse is applied and at the end of the pulse.

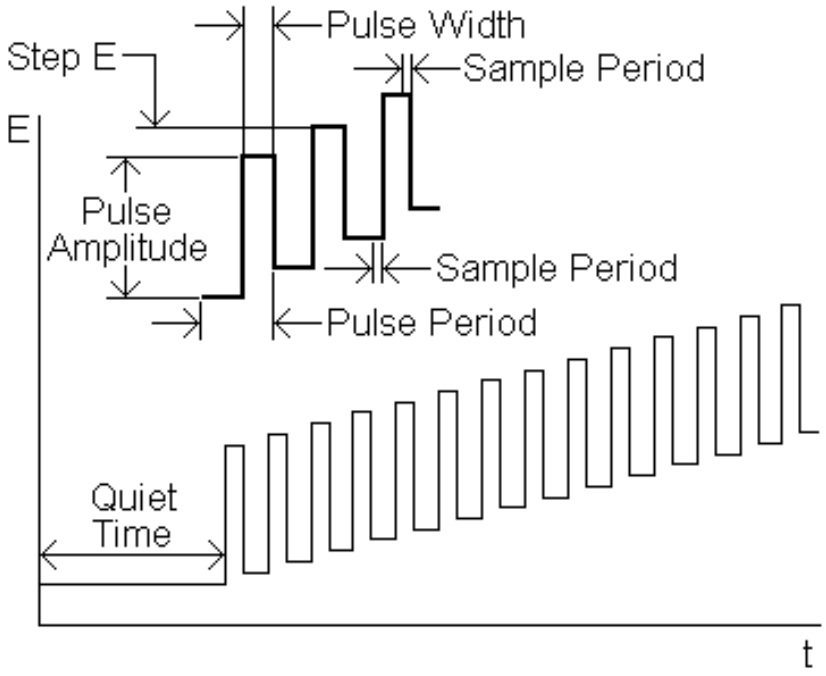

Figure 9: Differential Pulse Voltammetry waveform (Source: Bioanalytical Systems, Inc.)

Some of the important parameters of differential pulse voltammetry are:

- The Pulse Amplitude, ΔE is the applied potential (in mV) and the Step, E is the height of staircase wave form (in mV).

- The Pulse Width is the length of time (in ms) of pulse potential applied.
- Pulse Period is the time (in ms) needed for one cycle of potential variation.
- Pulse Period must be at least twice the Pulse Width.
- Sample Period is the time (in ms) at which current is measured.

The analysis of the redox potential from pulse voltammetry is simpler than for cyclic voltammetry. A differential pulse voltammogram is plotted as the difference in current against the applied potential. The differential waveform is symmetric for a reversible reaction and the redox potential is very close to the peak maximum.[57] A ferrocene differential pulse voltammogram oxidation peak is shown in Figure 10.

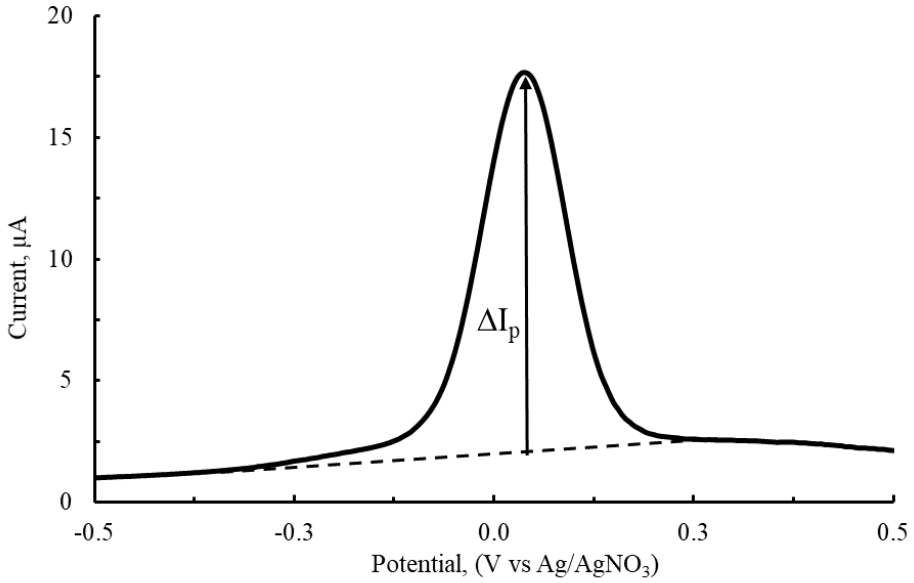

Figure 10: Ferrocene differential pulse voltammogram oxidation peak

In DPV for a reversible couple, the redox potential is almost coincident with peak potential and expressed as $E_{1/2} = E_{peak} + E_{pulse}/2$.

E_{pulse} is usually very small (for example 50mV). DPV is done in the same three electrode configuration as CV. The methods require a working electrode, a reference electrode, and a counter electrode.

2.1.3. AQUEOUS VS NON-AQUEOUS REFERENCE ELECTRODE

There are a few disadvantages to using the aqueous Ag/AgCl and saturated calomel reference electrodes for organic solvents. The junction potential across the salt bridge could result in a misleading electrochemical analysis. Precipitation of the electrolyte and contamination of the sample is a more serious problem in the case of using an aqueous electrode. KCl/ NaCl electrolytes are commonly used in making reference electrodes and they are not very soluble in organic solvents. Prolonged immersion of an aqueous electrode into organic solvents may cause electrolyte precipitation. The precipitation could lead to an increase in reference electrode impedance and changes the liquid junction potential, this causes a change in reference potential with time. Also, sample contamination from the reference electrode could cause serious problems. For example, many organometallic compounds are reactive to water thus using an aqueous reference electrode must be avoided. Therefore, it is better to use a non-aqueous reference electrode for organic electrochemistry. Two possibilities are the use of a pseudo reference electrode or the use of a Ag/Ag^+ electrode. Pseudo reference electrodes are easy to make simply by immersing metal into solution. Even though pseudo reference electrodes give constant potentials, their

potential is unknown and depends on the solution. The potential is reported relative to the redox potential of an internal reference compound.

The Ag/Ag+ reference electrode is made by immersing a silver wire in a solution of a suitable silver salt and base electrolyte into a suitable organic solvent. Suitable organic solvents are acetonitrile, dimethylsulfoxide, methanol, ethanol, and tetrahydrofuran. The potentials of silver/ silver ion electrode depend on the solvent, the concentration of silver ions and the concentration of the base electrolyte.

2.2. UV VISIBLE SPECTROSCOPY

The Highest Occupied Molecular Orbital (HOMO) and Lowest Unoccupied Molecular Orbital (LUMO) gap is an important parameter of redox active molecules in terms of their optoelectronic and chromophore properties. Redox active molecules for this research project will have a conjugated structure. We need to know how conjugation changes with chain length, and different substituent groups at the central ring. UV/Visible spectroscopy is a widely used analytical tool to obtain the HOMO-LUMO gaps of organic molecules. When ultraviolet and visible range light is absorbed by the molecule, electronic transitions happen between molecular orbitals. Some possible electronic transitions are shown in Figure 11. Light energy is absorbed during electron transitions.

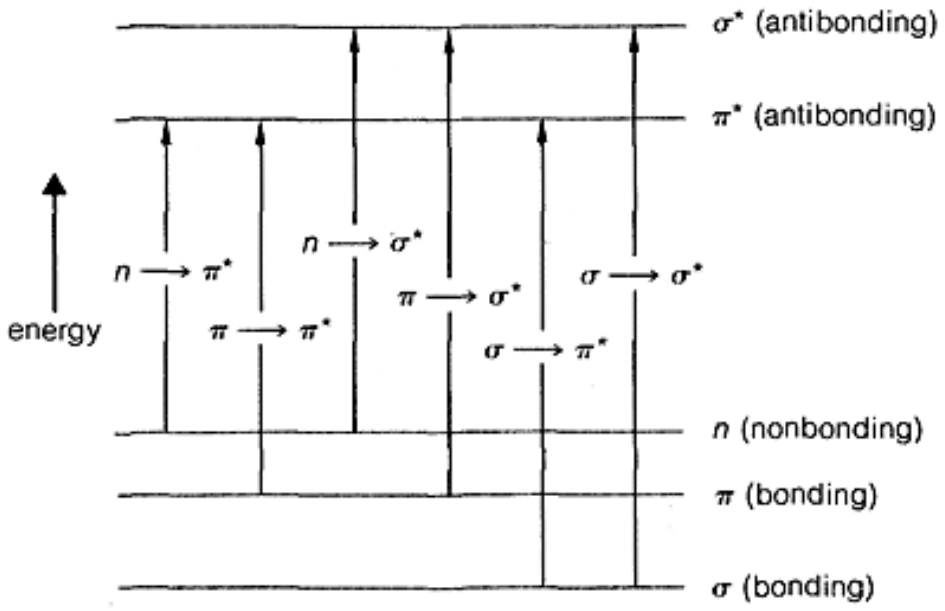

Figure 11: Possible electron transition in UV-Visible spectroscopy

Most probable transitions are $n \longrightarrow \pi^*$, $\pi \longrightarrow \pi^*, n \longrightarrow \sigma^*$ and they are important in terms of spectroscopy. An electronic transition results in an absorption maximum in UV-VIS spectrum corresponding to the absorbed energy during the electron transition. The energy associated with these maxima is used to calculate the energy gap between the molecular orbitals. Electrons from the highest occupied molecular orbital jump to the lowest unoccupied molecular orbital which normally gives an absorption maximum. Absorption maximum at low energy peak will be used to calculate the HOMO-LUMO gap.

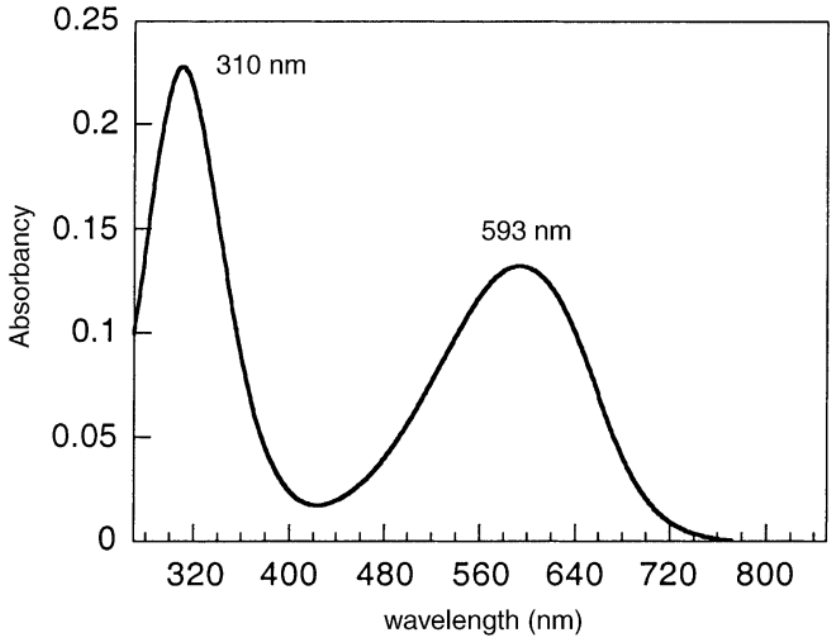

Figure 12: UV–VIS spectrum of phenyl/phenyl end-capped tetra aniline in the emeraldine oxidation state in DMSO solution.[58]

2.3. CONDUCTIVITY MEASUREMENT

Changes in electrical resistivity are an indicator of changes in the electronic structure of a material. Primarily electrical resistivity indicates a change in carrier density in response to changes in doping level for semiconducting materials. Any charge transfer thus changes the carrier density and can be measured by measuring the resistance of the materials. There are several resistivity measurement techniques available depending on the sample materials.[59–61] The most common techniques are two probe and four probe measurements.

2.3.1. TWO PROBE MEASUREMENTS

This is the simplest way to measure the resistance of a material. Usually, a voltage V is applied across the two terminals and current I is measured. The resistivity is thus calculated as, $\rho = \frac{VA}{IL}$, where ρ is resistivity, V is voltage applied, A is area of the specimen, I is current and L is length of the specimen. Two probe measurement is useful when the sample has high resistance.

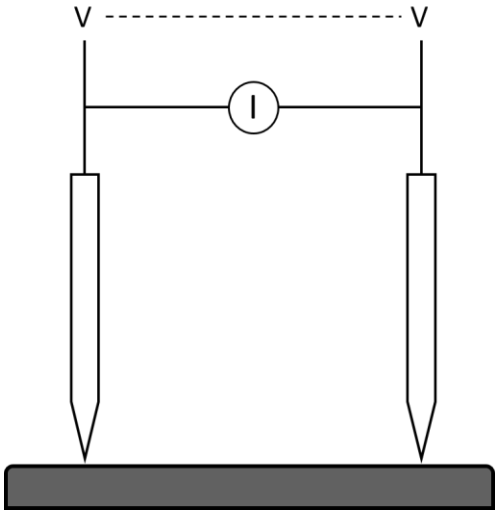

Figure 13: Two probe measurement terminal set up

2.3.2. FOUR PROBE MEASUREMENTS

Four probe measurements are widely used to measure the resistance of semiconducting materials. Usually, when we use a simple ohmmeter to measure the resistance of a sample it also measures the resistance of the terminal leads and contacts. The contact resistance could lead to inaccurate resistance measurements for semiconducting materials where the contact area is very small.

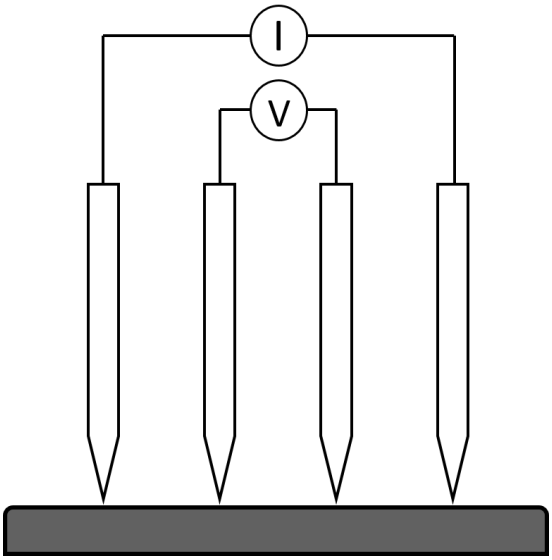

Figure 14: Four probe measurement terminal set up

With a four-point probe measurements technique, two points are connected at the edge of the specimen and a current is passed through it. The voltage drop is measured across the two inner contacts. Four probe measurements eliminate the contact resistance error, thus giving a more accurate resistivity measurement.

A simple two probe measurement will be used for this research project because, in our sensor geometry, the contact area has been sealed off from the sensing area. Thus, it is deemed that contact resistance will always be constant regardless of the conductance of the sensing film.

CHAPTER 3: SYNTHESIS AND CHARACTERIZATION OF REDOX ACTIVE ANILINE OLIGOMERS AND PYRENATED NEUTRAL RED

3.1. INTRODUCTION

Aniline compounds are of great importance in the field of electronic materials. Synthesis of anilines via the C-N cross-coupling route has been practiced for a long time. Among the various cross-coupling aminations, Buchwald-Hartwig coupling[62–66], and Ullman-type amination[67–69] are the most prominent. In these types of reactions, aryl halides are usually coupled with amines in the presence of catalysts. The reaction schematics are shown below.

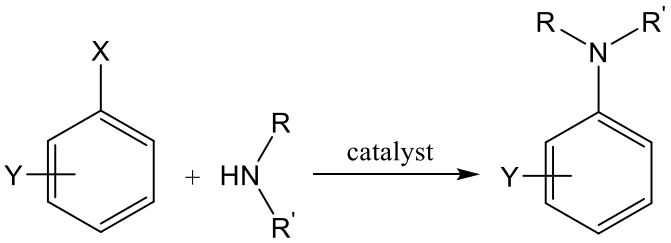

Figure 15: Schematic of C-N cross coupling reaction

Four of our targeted redox active molecules are aniline compounds. DPPD and SDPPD are readily available from Sigma-Aldrich. PCAT and APCAT can be synthesized by following palladium catalyzed Buchwald-Hartwig coupling of N-Phenyl-p-phenylenediamine and a suitable dibromo aryl. APCAT will be synthesized by following Buchwald-Hartwig amination. There is a direct synthesis process available for PCAT from the coupling of N-Phenyl-p-phenylenediamine and hydroquinone in presence of a condensating agent.[58] This reaction doesn't need a catalyst and the work-up of the reaction

mixture is relatively easier than for the Buchwald-Hartwig amination. Crystal violet is a triaryl methane redox active compound that is available from Sigma-Aldrich.

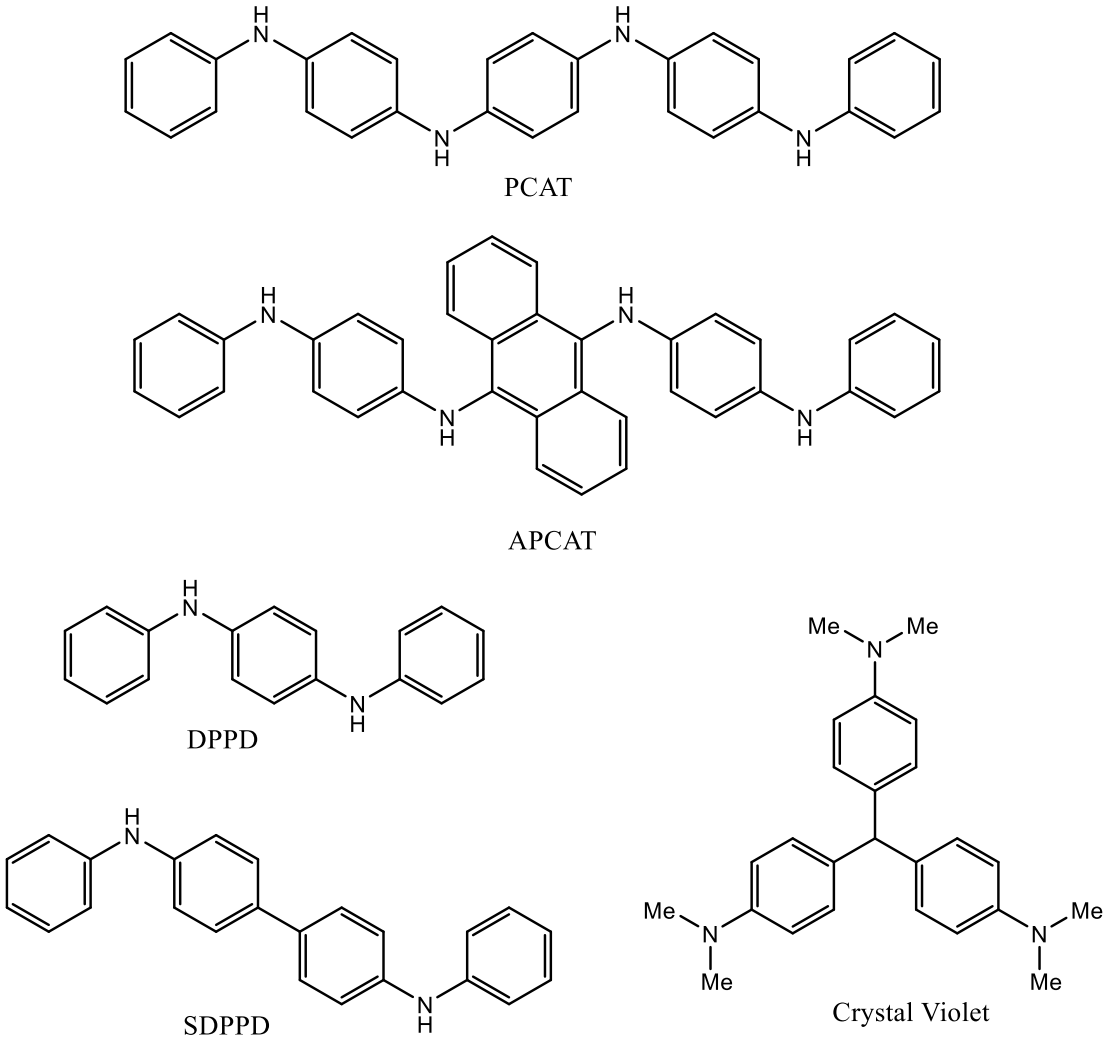

Figure 16: Redox active molecules

For the pH indicator project, a large nonpolar ring such as pyrene could be introduced to the neutral red by following palladium catalyzed Buchwald-Hartwig

amination.[70,71] Bromopyrene and neutral red will be coupled together in this one step synthesis process. Bromomethyl pyrenated neutral red will be synthesized from N-alkylation of Neutral red and 1-bromomethyl pyrene in presence of a base. Cesium bases were reported to be an efficient chemoselective agent for direct mono N-Alkylation of primary amines and alkyl halides.[72,73]

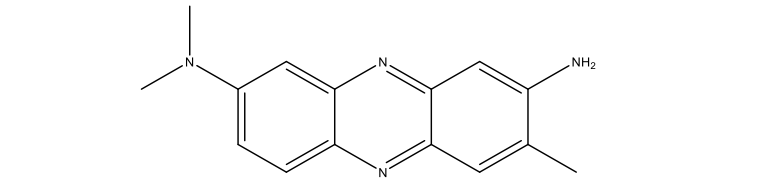

Neutral Red

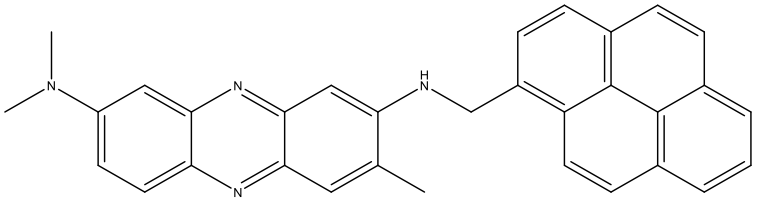

Methyl Pyrenated Neutral Red

Figure 17: Pyrenated neutral red derivatives

3.2. SYNTHESIS AND CHARACTERIZATION

3.2.1. PHENYL CAPPED ANILINE TETRAMER (PCAT) AND ITS OXIDATION STATES:

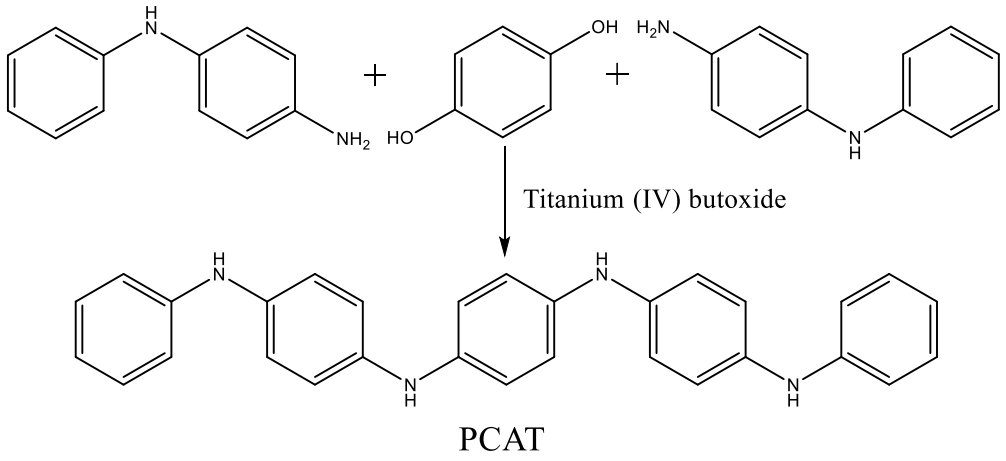

Figure 18: Synthesis of Phenyl Capped Aniline Tetramer in its leucoemeraldine state

N^1,$N^{1'}$-(1,4-phenylene)-bis(N^4-phenyl benzene-1,4-diamine), was synthesized by a coupling reaction of N-Phenyl-p-phenylenediamine and hydroquinone in a controlled argon atmosphere in presence of titanium (IV) butoxide as a coupling agent. The synthesis was followed as reported by MacDiarmid[58] with slight modification. Toluene was used instead of benzene for this synthesis, as benzene is a designated substance and has regulated use. N-Phenyl-p-phenylenediamine, hydroquinone, titanium(IV) butoxide, anhydrous toluene and DMF all were purchased from Sigma-Aldrich. A 250 ml round bottom flask was equipped with a Teflon stirring bar and water-cooled reflux condenser capped with a rubber septum. 9.2 g (0.050 moles) solid N-Phenyl-1,4-phenylenediamine was added to the flask. The reaction flask was purged with argon and kept under a positive pressure using argon balloons. The flask was heated to 70 ^{0}C in an oil bath on a magnetic stirring plate.

100ml anhydrous toluene was added with a syringe through the septum, a black solution was formed. Another 100 ml round bottom flask was equipped with Teflon stirring bar and rubber septum. 1.38 g (0.0125 moles) hydroquinone was added to the flask and the flask was purged with argon. The flask environment was protected it with argon balloons connected through a rubber septum. The flask was placed in a preheated 70 ^{0}C oil bath on a magnetic stirring plate. 40 ml anhydrous toluene was added through a syringe to the flask. Hydroquinone doesn't dissolve in the toluene immediately. 25.6 ml colorless liquid titanium (iv) n-butoxide was added to the flask using a syringe, an orange solid formed in the solution. Hydroquinone and titanium (iv) n-butoxide were stirred for 30 minutes and an orange-red solution was formed. The orange-red solution was then added to the black solution of N-Phenyl-p-phenylenediamine using a cannula transfer. The empty bottle of the orange-red solution was washed with 10 ml anhydrous toluene and added to the final reaction mixture. The reaction system was then stirred for 16 hours at 70 ^{0}C under the protection of argon.

A crystalline precipitate formed during this time. The reaction flask was then cooled to room temperature under argon. White needle-shaped microscopic crystals were collected on a fritted Buchner funnel by vacuum filtration using an air pump. The precipitate was washed with laboratory grade toluene until the dark-brown red filtrate become colorless. Around 650 ml toluene was used. After washing the precipitate was kept under suction for 10 minutes. The precipitate was then dissolved in 120 ml of DMF and stirred for 10 min, a dark blue solution formed. The solution was vacuum filtrated on a Buchner funnel (~4.25 cm) with #1 Whatman filter paper using an air pump. The filtrate was added to 1200 ml

deionized water in a 2000 ml beaker drop by drop during 2 hours. The solution was stirred for 15 hours. A greenish precipitate formed. The precipitate was collected on a Buchner funnel (~9cm) with a #1 Whatman filter paper by vacuum filtration. The precipitate was washed with 100ml deionized water. After washing, the solution remains under suction for 10 minutes. The precipitate was then transferred on the filter paper to a desiccator and kept under vacuum for 48 hours at room temperature. The dry precipitate was pulverized by mortar and pestle into a fine powder and was further dried under vacuum for another 48 hours. As prepared aniline tetramer was found in its leucoemeraldine base form.

3.2.1.1. LEUCOEMERALDINE BASE

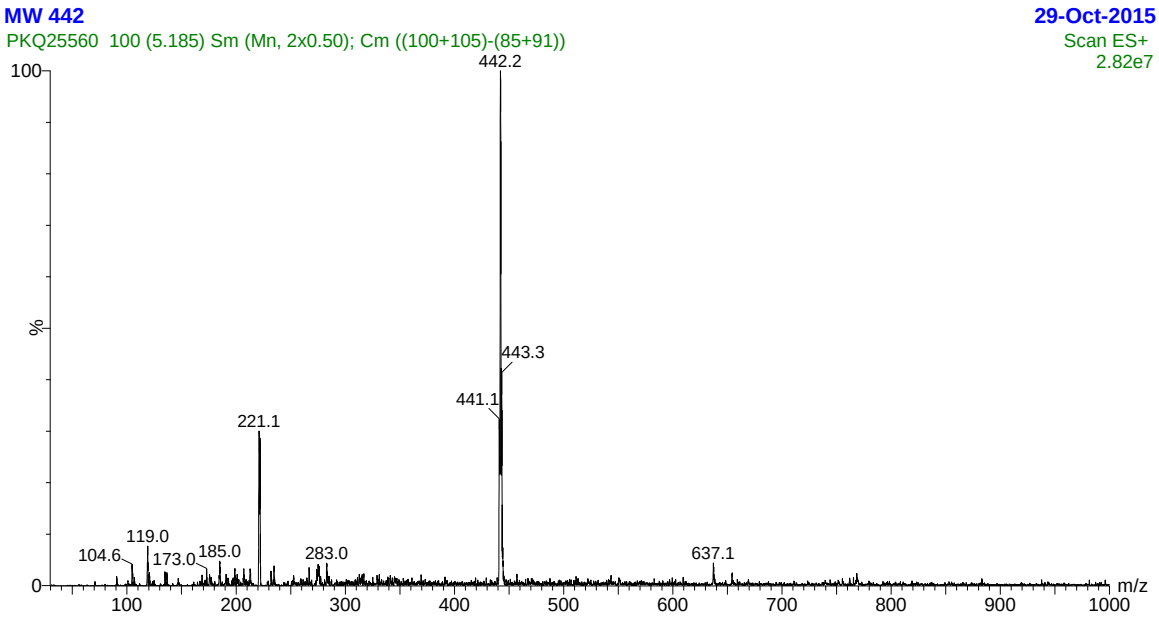

Figure 19: Mass spectrum of PCAT leucoemeraldine base

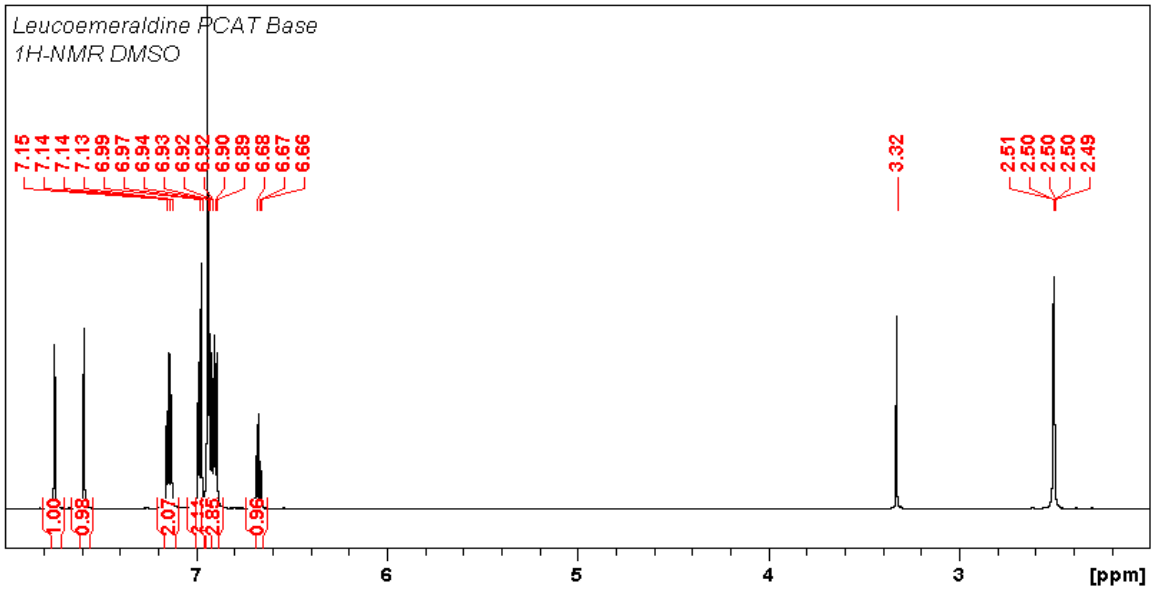

Figure 20: 1-H NMR spectrum of leucoemeraldine base

Leucoemeraldine base was characterized using mass spectrometry and nuclear magnetic resonance spectroscopy. The calculated mass is 442.2157 and the mass found was 442.2. The mass spectrum and NMR spectrum are shown above. NMR spectrum for leucoemeraldine base found ^{1}H NMR (600MHz, DMSO)δ: 7.74(2H^{b},s), 7.59(2H^{a},s), 7.14(4H^{d},t), 6.97(4H^{e},d), 6.94(12H^{,f,g},m), 6.67(2H^{c},t)ppm.

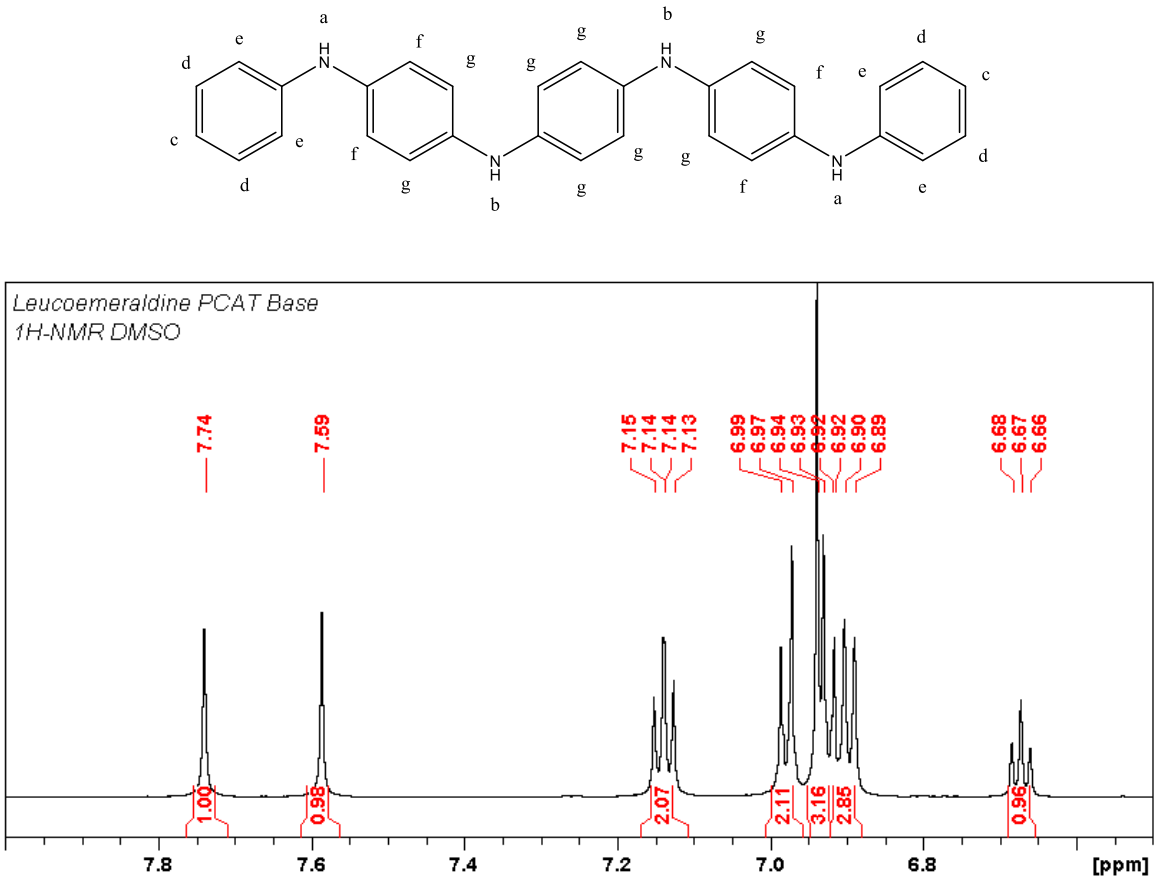

Figure 21: ^{1}H NMR Spectrum of leucoemeraldine base elaborated

3.2.1.2. EMERALDINE BASE

PCAT emeraldine and pernigraniline base were synthesized by oxidation with different proportional amounts of ammonium persulfate. The oxidation chemistry of ammonium persulfate is according to $S_2O_8^{2-} + 2H^+ + 2e^- \longrightarrow 2HSO_4^-$, which is a two-electron process. Oxidation of leucoemeraldine base to emeraldine is also a two-electron process. Thus, the oxidizing agent is used in a 1:1 molar ratio. For the pernigraniline base, the oxidation process needs four electrons. The oxidizing agent is used in a 1:2 molar ratio. Both

oxidation processes are similar except the molar ratio of ammonium persulfate used. The process for synthesizing emeraldine base from the leucoemeraldine base is given below.

A solution of ammonium persulfate (0.78 g, 3.4 mmol, 1 eq.) in hydrochloric acid (100 mL, 1 M) was made. Another solution of the leucoemeraldine base state (1.5 g, 3.4 mmol, 1 eq.) was made with DMF (100 mL). Ammonium persulfate solution is added dropwise and the resulting solution is kept under stirring for 60 min. The solution was then poured into stirred deionized water (800 mL) and stirred for 15 min. The resulting deep green precipitate was collected by vacuum filtration using no.1 Whatman filter paper. The precipitate was treated with acetone (200 mL) and ammonium hydroxide (100 mL, 2 M), with stirring, for 16 hours. After removal of acetone from the mixture under reduced pressure, the residue was filtered to afford the product, in the emeraldine base form.

Emeraldine base was characterized by mass spectrometry and NMR spectroscopy. The calculated mass of the emeraldine base is 440.2071 and found was 441.2079 as MH^+. Analyzing the NMR spectrum in Figure 22, we can see that the oxidation process gave a mixture of leucoemeraldine and emeraldine bases. Emeraldine base also exists in its two isomers shown below. Therefore, the NMR spectrum is composed of many peaks. However, we can clearly assign the characteristic leucoemeraldine base peaks for proton adjacent to nitrogen at 7.74 ppm and 7.58 ppm (shown in Figure 23).

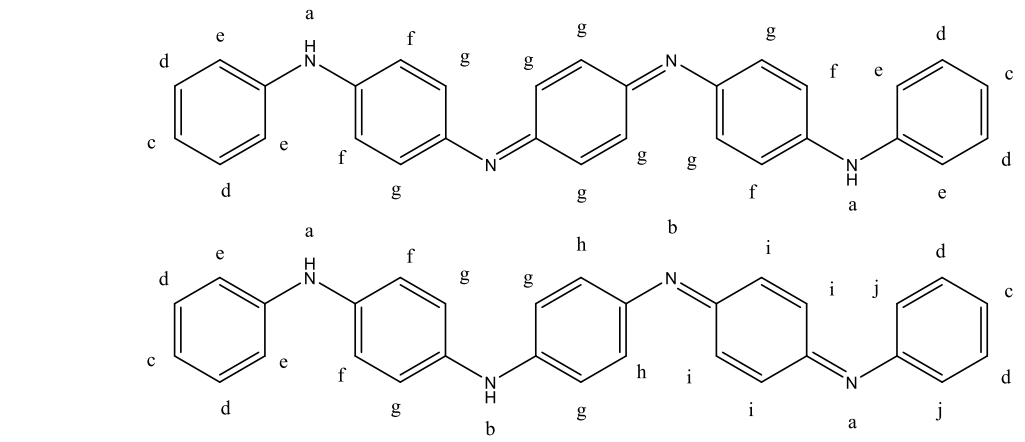

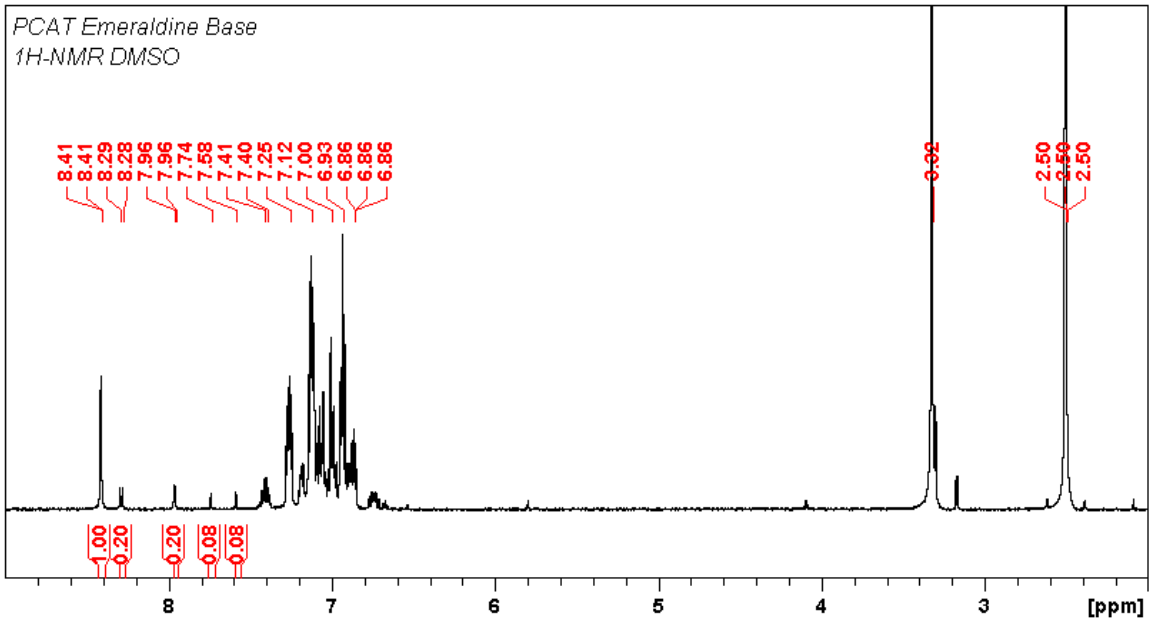

Figure 22: ^{1}H NMR spectrum of PCAT emeraldine base

By taking the comparative integration of leucoemeraldine and emeraldine peaks in Figure 23 the calculated conversion was found to be 90%. We also compared emeraldine peaks at 7.96 ppm, 8.29 ppm, and 8.41 ppm to calculate the ratio of isomers. The Isomer ratio was found to be 72.5:28.5 which is consistent with the reported literature.[74]

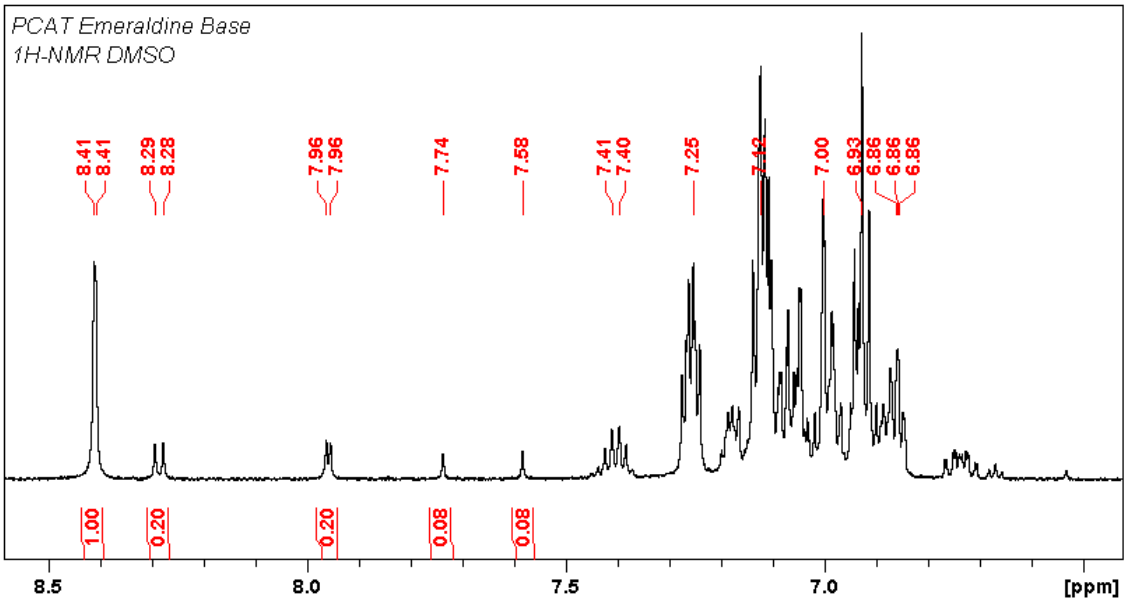

Figure 23: ^{1}H NMR peak integration of PCAT emeraldine base and leucoemeraldine base

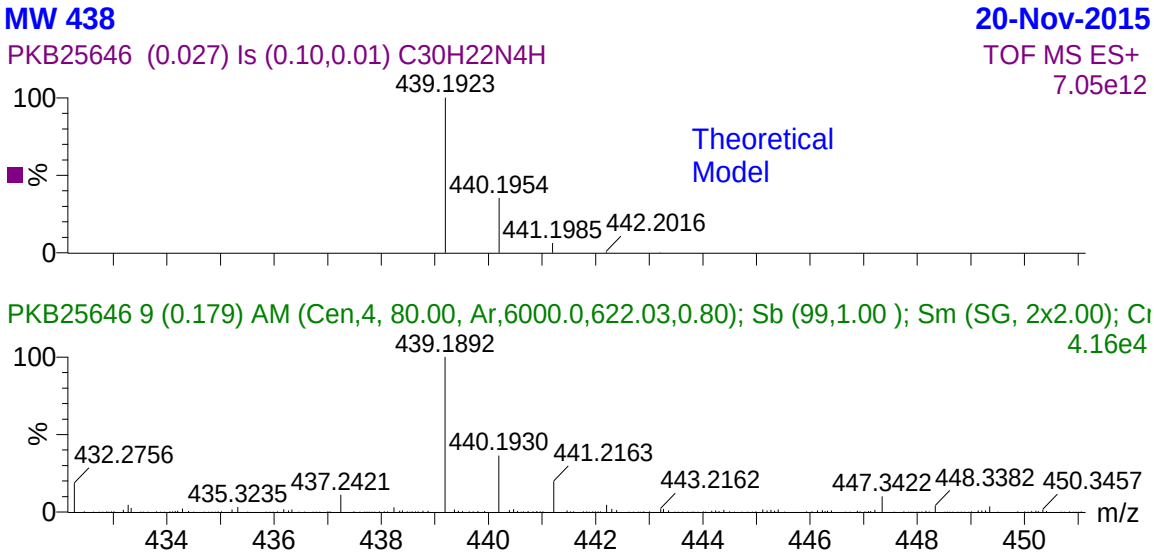

Figure 24: Mass spectrum of PCAT pernigraniline base

3.2.1.3. PERNIGRANILINE BASE

PCAT Pernigraniline base was synthesized by following the same procedure as the emeraldine base with a 1:2 ratio of leucoemeraldine base and an oxidizing agent. The pernigraniline base was characterized by mass spectrometry and NMR spectroscopy. The calculated mass is 438.18 and the mass spectrum shows the presence of molecular weight 439.13 as MH^+. The NMR data doesn't show any significant spectrum for the pernigraniline base and the reason might be due to the delocalized electron resonance in the pernigraniline structure.

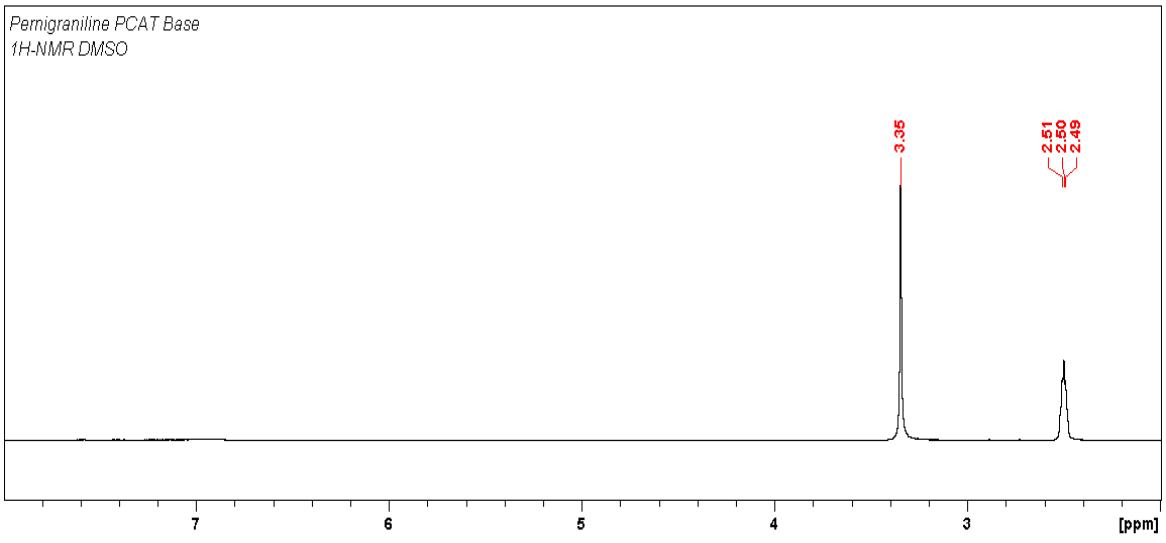

Figure 25: ^{1}H NMR spectrum of PCAT emeraldine base

3.2.2. $N^1,N^{1'}$-(ANTHRACENE-9,10-DIYL)-BIS (N^4-PHENYL BENZENE-1,4-DIAMINE) (APCAT) SYNTHESIS:

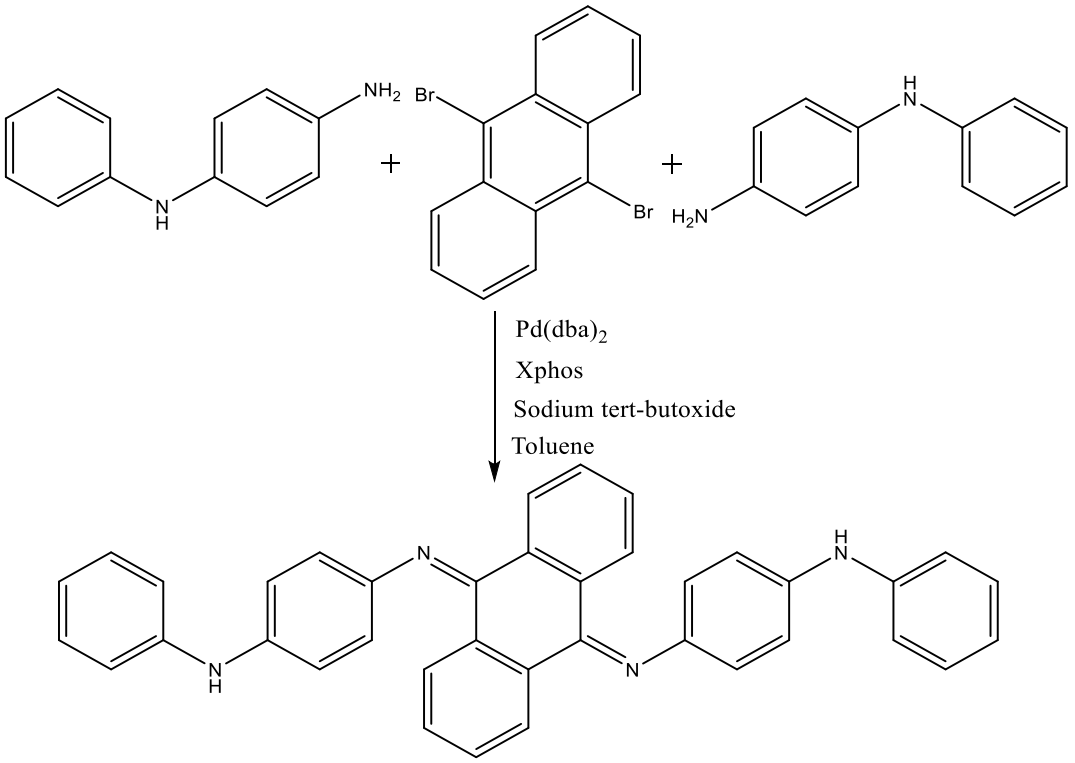

Figure 26: Synthesis of Anthracene substituted Phenyl Capped Aniline Tetramer

$N^1,N^{1'}$-(anthracene-9,10-diyl)-bis (N^4-phenyl benzene-1,4-diamine) (APCAT) was synthesized by the Buchwald-Hartwig Amination of N-Phenyl-p-phenylenediamine and 9,10-Dibromoanthracene. A 250 ml round bottom flask with a magnetic stirrer was loaded with 9,10-dibromoanthracene (0.877 g, 2.61 mmol, 1 equivalent), N-Phenyl-p-phenylenediamine (1.05 g, 5.74 mmol, 2.2 equivalent), Pd(dba)2 (0.09 g, 0.16 mmol, 6 mol%), Xphos (0.12 g, 0.23 mmol, 9 mol%) and sodium tert-butoxide (0.75 g, 7.83 mmol, 3 equivalent). The round bottom flask was fitted with a water-cooled reflux condenser and sealed with a rubber septum. The round bottom flask was then purged with argon for 15

minutes and 40 ml anhydrous toluene was added to the flask using a syringe. The flask was then placed in a 100 °C preheated oil bath. The reaction flask was protected by argon balloons. The progress of the reaction was monitored by doing TLC. The reaction was run for 36 hours until the absence of 9,10-dibromoanthracene was seen in TLC. The reaction was cooled to room temperature and 50ml ethanol and 200ml water were added to the reaction mixture and stirred for 10 hours. The product was separated out as a dark orange precipitate. After the filtration, the product was washed 3 times with a 20% ethanol in water solution. The precipitate was then dried in a desiccator under vacuum for 48 hours.

The APCAT product was characterized by mass spectroscopy and NMR spectroscopy. Chemical Formula: $C_{38}H_{30}N_4$, Exact Mass = 542.25, Molecular Weight = 542.69. The mass spectrum shows the $M+H^+$ peak for 541 which indicates that APCAT was synthesized in its half oxidized state.

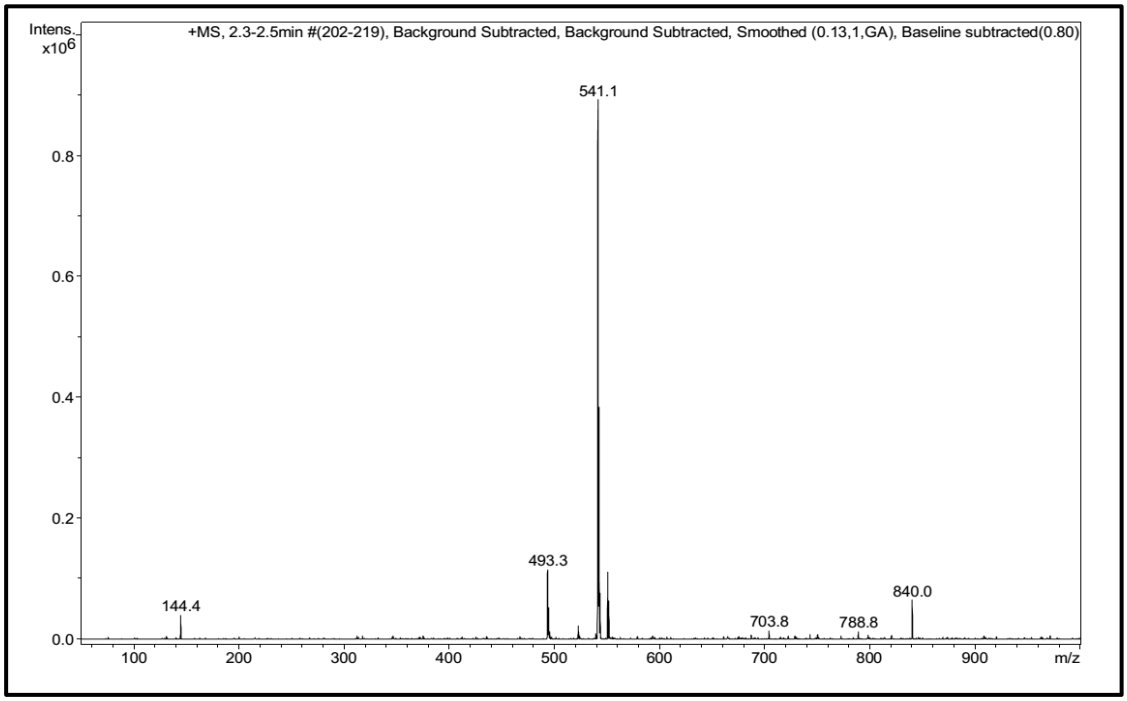

Figure 27: Mass spectrum of synthesized APCAT

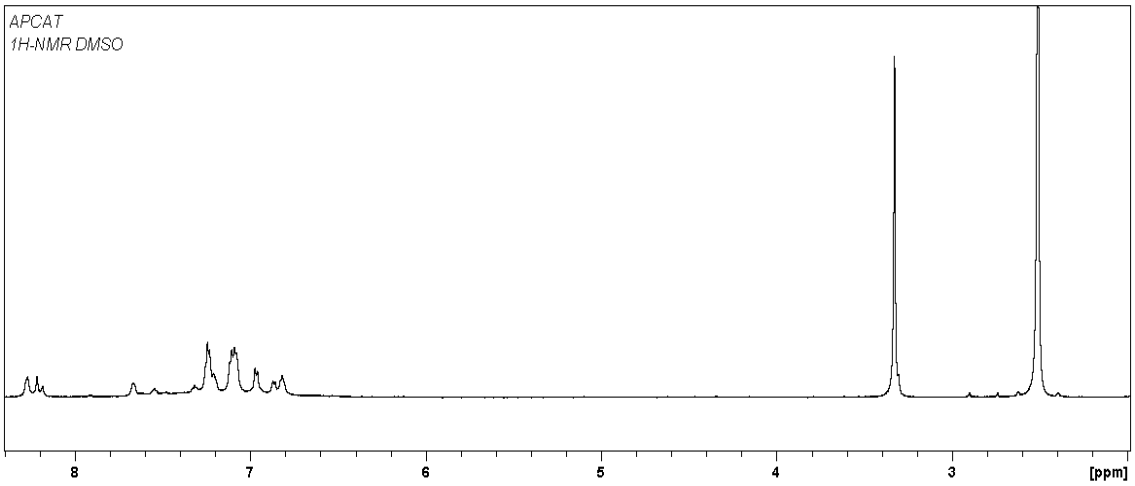

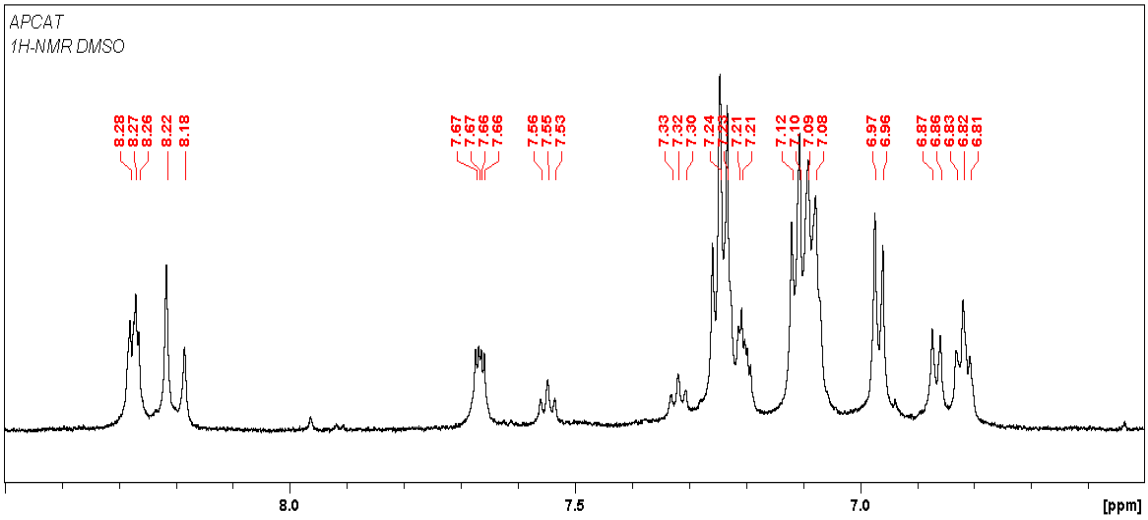

Figure 28: ^{1}H NMR spectrum of synthesized APACT

The APACT NMR spectrum looks like the synthesized product is indeed a mixture. From the PCAT emeraldine base, we have seen that it consists of two isomers. It is most likely that the APCAT is in its emeraldine base form and a mixture of isomers. The emeraldine base was tried to reduce with ascorbic acid, formic acid, and phenyl hydrazine but without success. This might be due to the easy air oxidation of APACT leucoemeraldine base to emeraldine base.

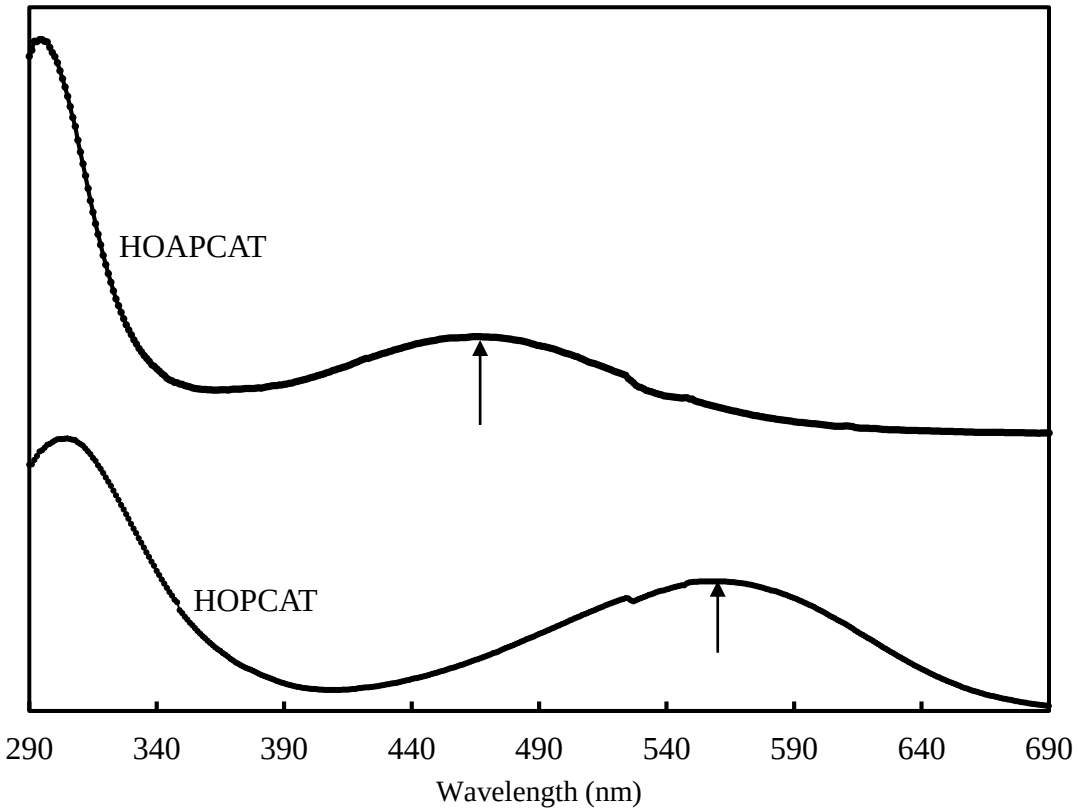

Figure 29: UV spectra of PCAT and APCAT emeraldine base

In comparison to the PCAT emeraldine base, APCAT emeraldine base also shows a similar peak for quinoid formation. The anthraquinoid peak is seen at 470nm for the APCAT molecule. Overall, mass spectrometry, NMR spectroscopy, and UV-Vis spectroscopy strongly indicate that the synthesized product is the APCAT emeraldine base.

N, N-Diphenyl-p-phenylenediamine (DPPD), N, N′-Diphenyl benzidine (SDPPD) and Crystal Violet are available commercially and purchased from Sigma-Aldrich. Their NMR characterization is shown below.

3.2.3. N, N-DIPHENYL-P-PHENYLENEDIAMINE (DPPD)

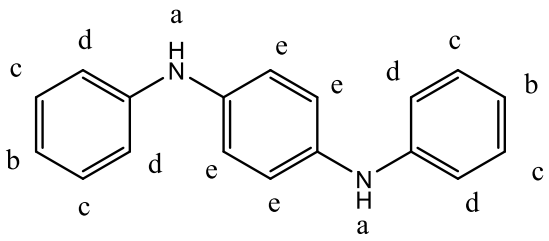

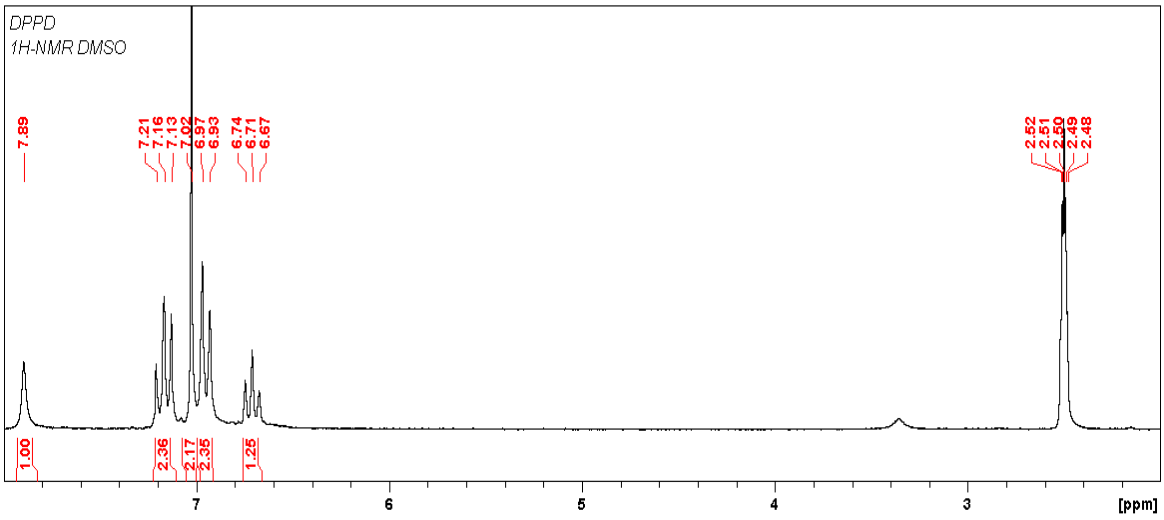

Figure 30: ^{1}H NMR spectrum of DPPD

The DPPD ^{1}H NMR spectrum is seen (600 MHz, DMSO) δ: 7.89(2H^{a},s), 7.21(4H^{c},t), 7.02(4H^{d},d), 6.97(4H^{e},d), 6.71(2H^{b},t)ppm.

3.2.4. N,N'-DIPHENYL-4,4'-BIPHENYLENEDIAMINE (SDPPD)

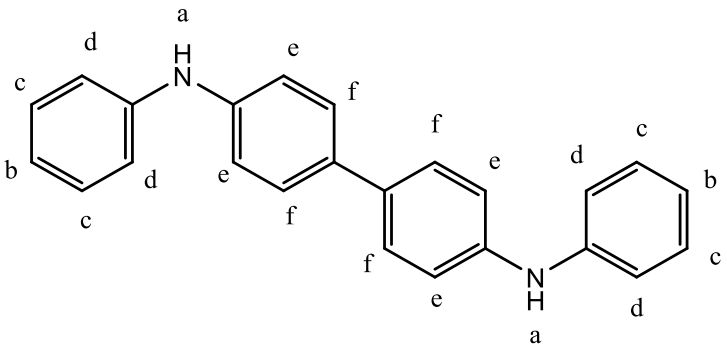

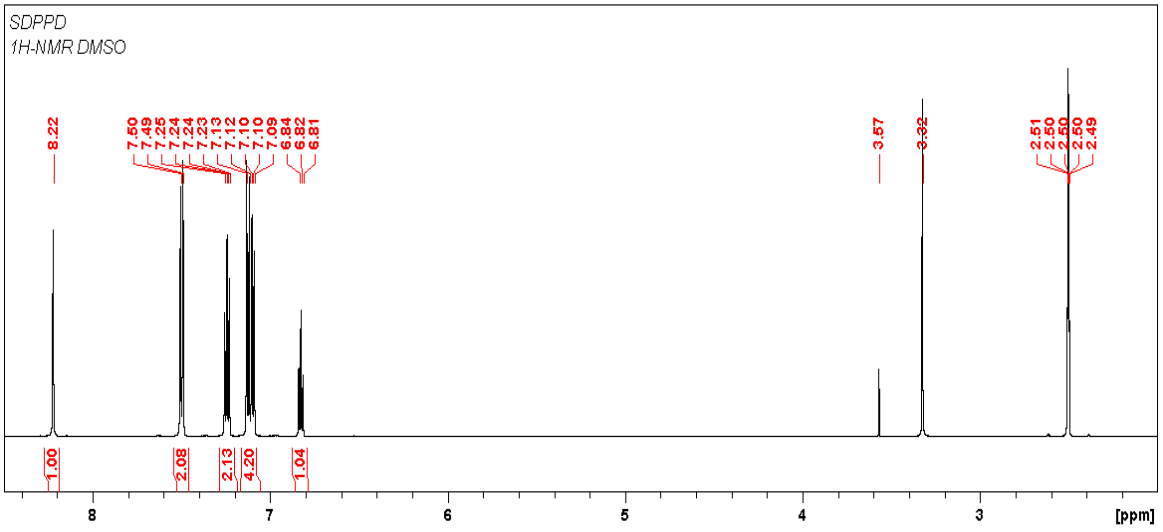

Figure 31: ^{1}H NMR spectrum of SDPPD

The SDPPD ^{1}H NMR spectrum is seen (600 MHz, DMSO) δ: 8.22(2H^{a},s), 7.50(4H^{f},d), 7.24(4H^{c},t), 7.13 (4H^{e},d), 6.10(4H^{d},d), 6.82(2H^{b},t)ppm.

3.2.5. CRYSTAL VIOLET

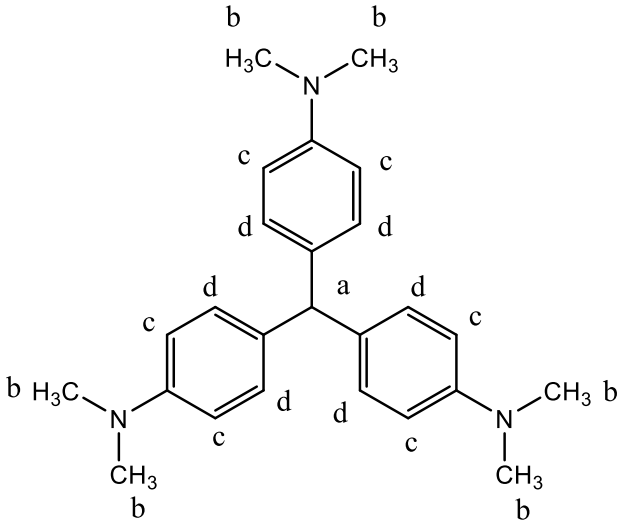

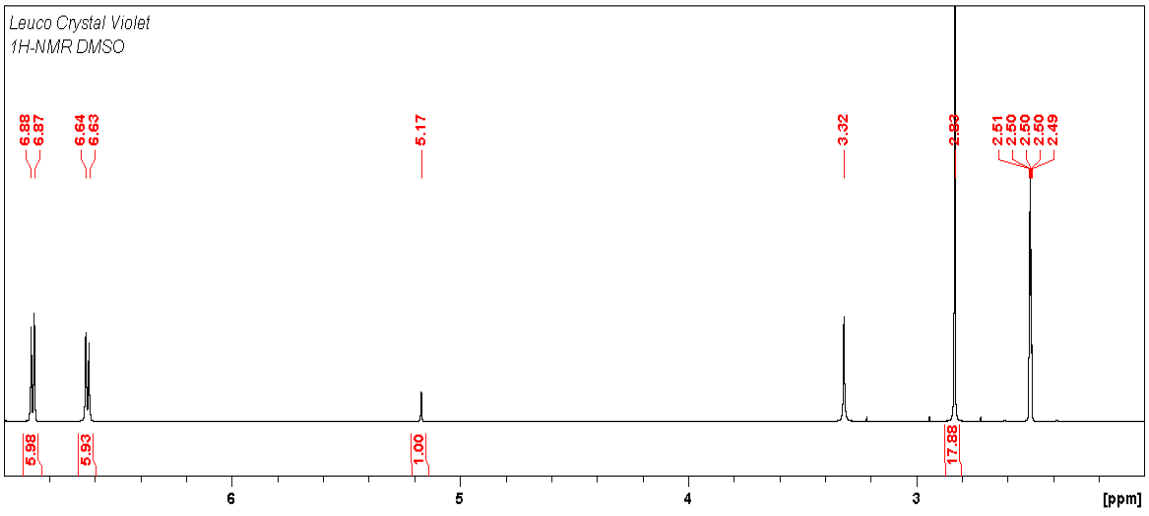

Figure 32: ^{1}H NMR spectrum of Crystal Violet

The Crystal Violet ^{1}H NMR spectrum is seen (600 MHz, DMSO) δ: 6.88($6H^{d}$,d), 6.64($6H^{c}$,d), 5.17($1H^{a}$,s), 2.83($18H^{b}$,s)ppm.

3.3. NEUTRAL RED DERIVATIVES

3.3.1. METHYL PYRENATED NEUTRAL RED

The synthesis was done by N-alkylation of neutral red and 1-bromomethyl pyrene in presence of cesium carbonate. Neutral red salt, Ce_2CO_3, 1-bromomethyl pyrene are purchased from Sigma-Aldrich. As purchased neutral red salt was first converted into the neutral red base by reacting with ammonium hydroxide. 1.32 g neutral red salt was dissolved in 20 ml DMF and the resulting solution was added to a 100 ml 0.1 M NH_4OH solution. The mixture was stirred for 30 minutes and a precipitate forms. The precipitate was collected by vacuum filtration and washed with water. Minimum 500ml water was used to wash the precipitate. The precipitate is then dried under vacuum for 48 hours. The dried powder was characterized as neutral red base and proceeded for neutral red derivative synthesis. 0.76 g (3 mmol) neutral red and 0.98 g (3 mmol) $CsCO_3$ were added to 20 ml DMF and stirred for 30 minutes at room temperature. 0.53 g (1.8 mmol) 1- bromomethyl pyrene was added to the reaction mixture and stirred for 32 hours. The reaction was monitored by TLC to see the consumption of 1-bromomethyl pyrene. The reaction mixture was filtered and the filtrate was collected. The filtrate was then added to 150 ml 20% ethanol and water solution. The mixture was stirred for 2 hours and a precipitate formed. The precipitate was collected and washed with 0.1 M NH_4OH. The precipitate was dried under vacuum for 48 hours.

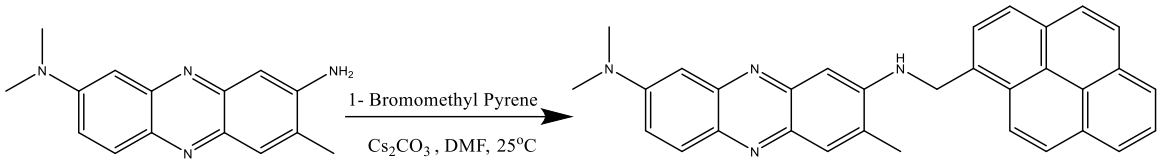

Figure 33: Synthesis of methyl pyrenated neutral red

The product is characterized by mass spectrometry and NMR spectroscopy. N^8,N^8,3-trimethyl-N^2-(pyrene-1-ylmethyl)phenazine-2,8-diamine (Methyl pyrenated neutral red), Chemical Formula: $C_{32}H_{26}N_4$, Exact Mass: 466.22, Molecular Weight: 466.59. The mass spectrum shows the significant presence of molecular weight 466.22 at 467.22 as $M+H^+$. It also shows the presence of neutral red at mass 253.15 as $M+H^+$.

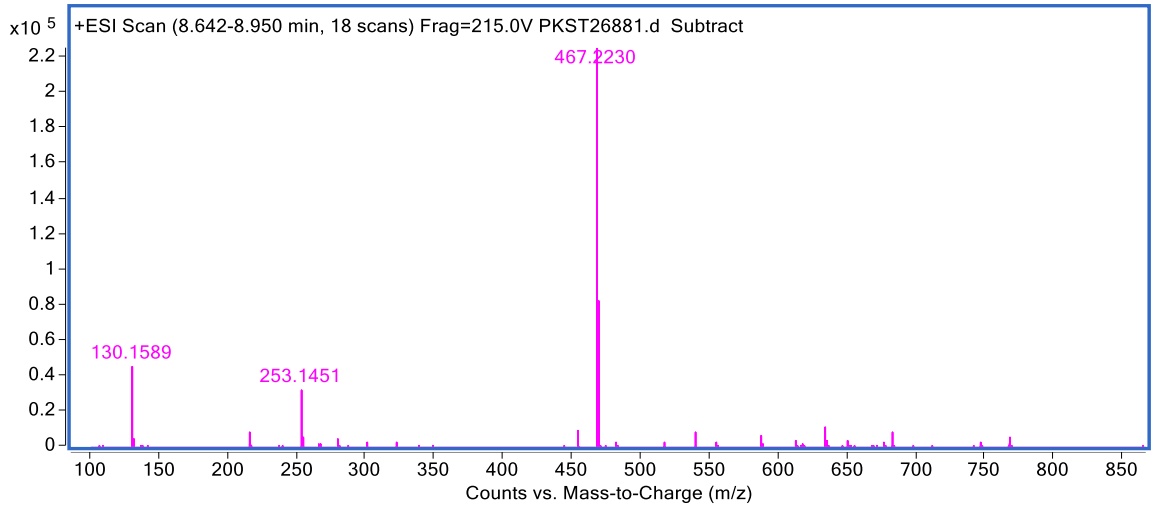

Figure 34: Mass spectrum of methyl pyrenated neutral red

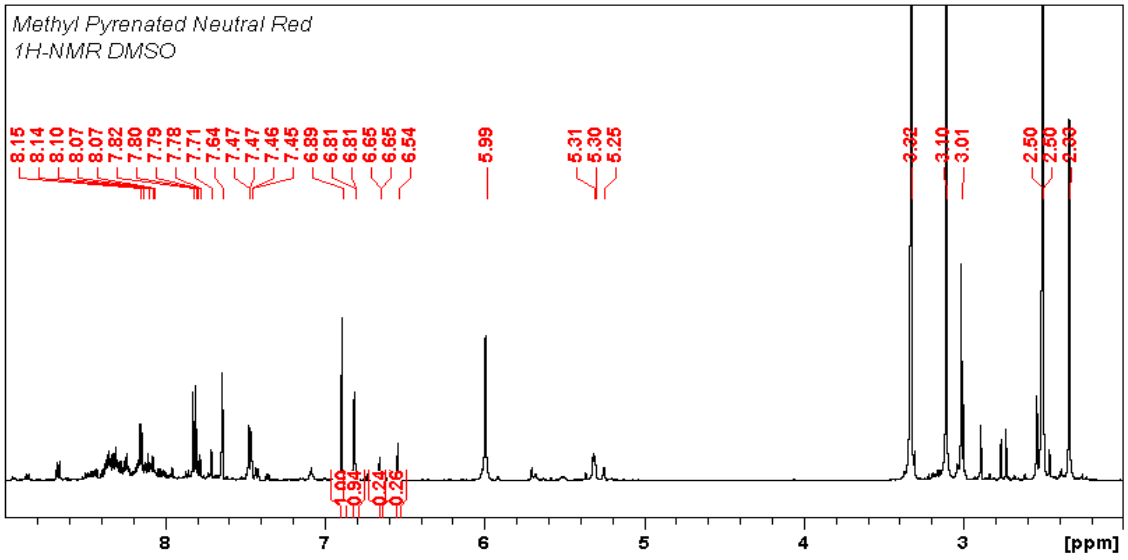

Figure 35: ^{1}H-MMR spectrum of methyl pyrenated neutral red

The NMR spectrum of Figure 35 indicates that the product is a mixture of neutral red and methyl pyrenated neutral red derivatives. From the peak integration calculation from 6.5 to 7.0 ppm, the product contains about 20% derivatives. We can also see a significant proton peak shift due to the addition of a large pyrenated ring to the neutral red. The neutral red base ^{1}H NMR spectrum is seen at peaks 7.81(1H^{h},d), 7.64(1H^{e},s), 7.46(1H^{g},d), 6.89(1H^{d},s), 6.81(1H^{f},d), 6.00(2H^{c},s), 3.18(6H^{a},s), 2.33(3H^{b},s)ppm which can be easily identified in the derivate mixture.

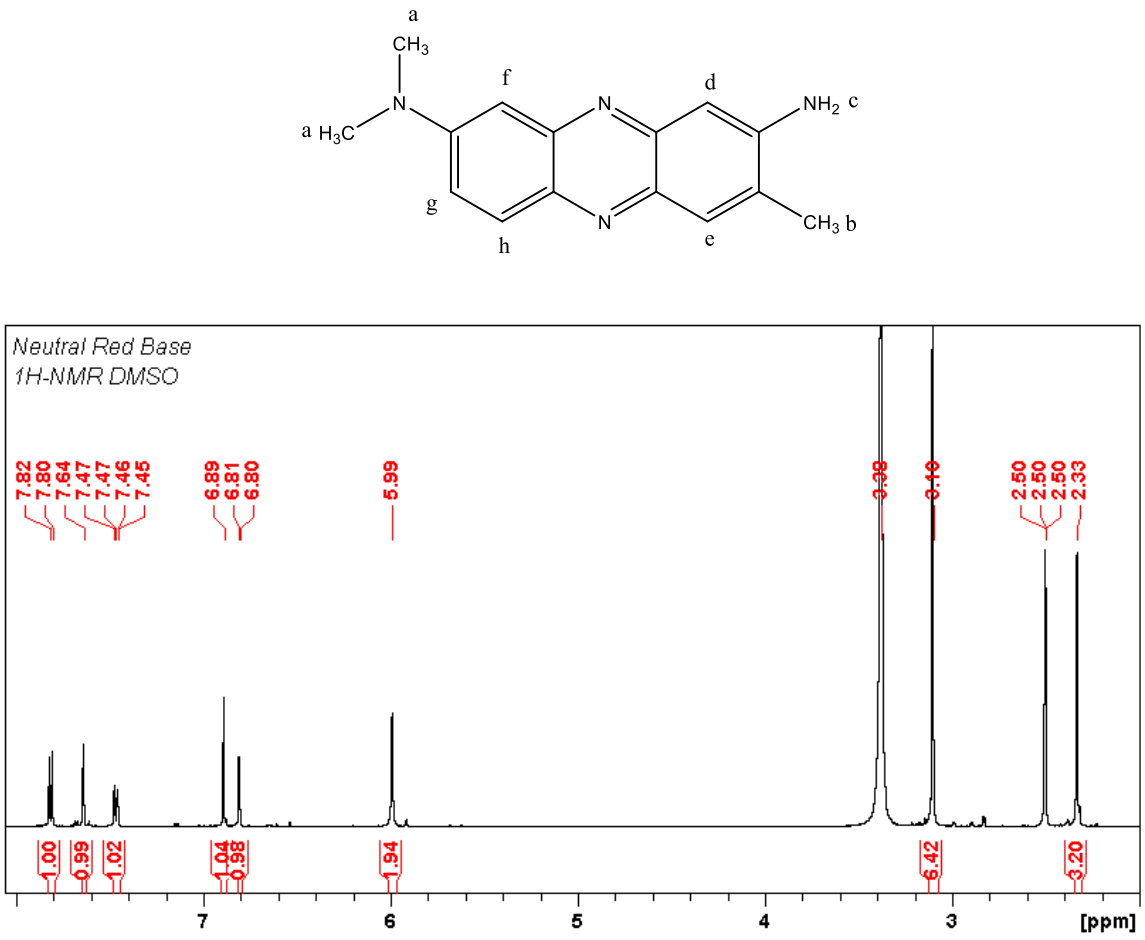

Figure 36: ^{1}H NMR spectrum of neutral red base

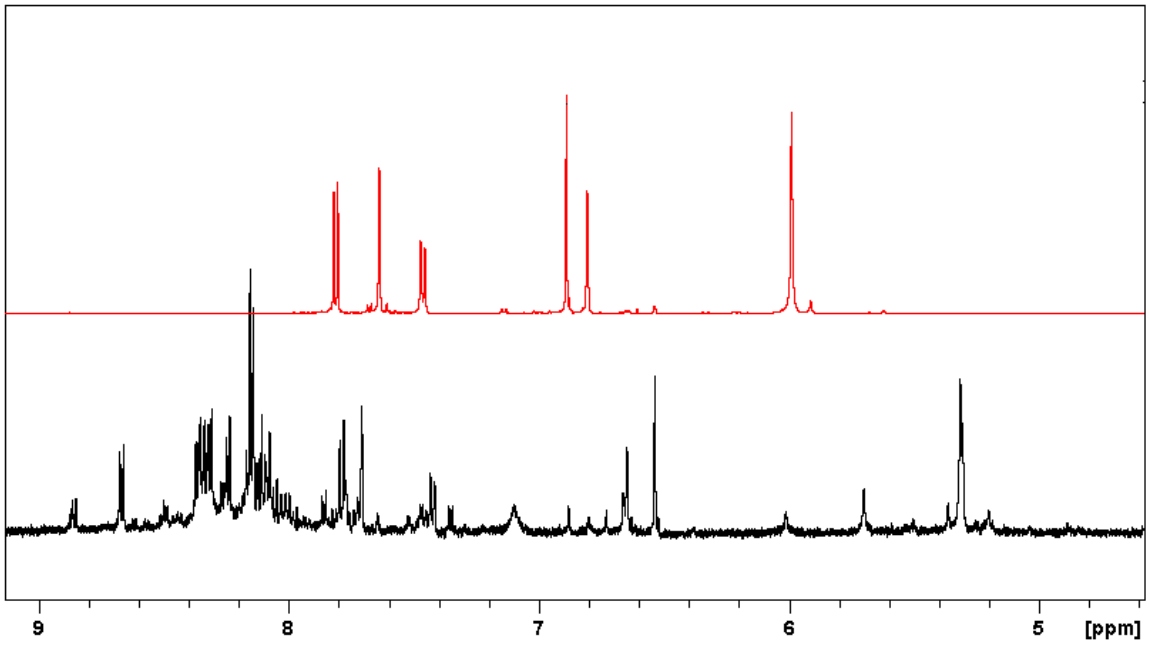

Figure 37: ^{1}H NMR spectra comparison of neutral red derivative (black) and neutral red (red)

Adding a pyrene ring will decrease the solubility of neutral red derivatives in polar solvents such as water. We have shown the separation of the product mixture based on the solubility difference of derivative and neutral red in their salt and base form in an aqueous medium. The product mixture was first added to a 0.1 M HCl solution to convert the product into the salt form. The salt formation was confirmed by observing the color change. The mixture was then stirred for 30 minutes. The solution was then titrated with 0.1 M NH_4OH to convert the product into the base. The base formation was confirmed by observing the color change. The mixture was again stirred for 30 minutes and the base forms a precipitate. The precipitate was filtered using vacuum filtration and washed with water. The precipitate was collected and the formation of salt and base was repeated 3 more times. The final

precipitate was dried for 48 hours in vacuum. The final product shows that it is almost free of neutral red that can be seen from the NMR spectrum shown in Figure 37.

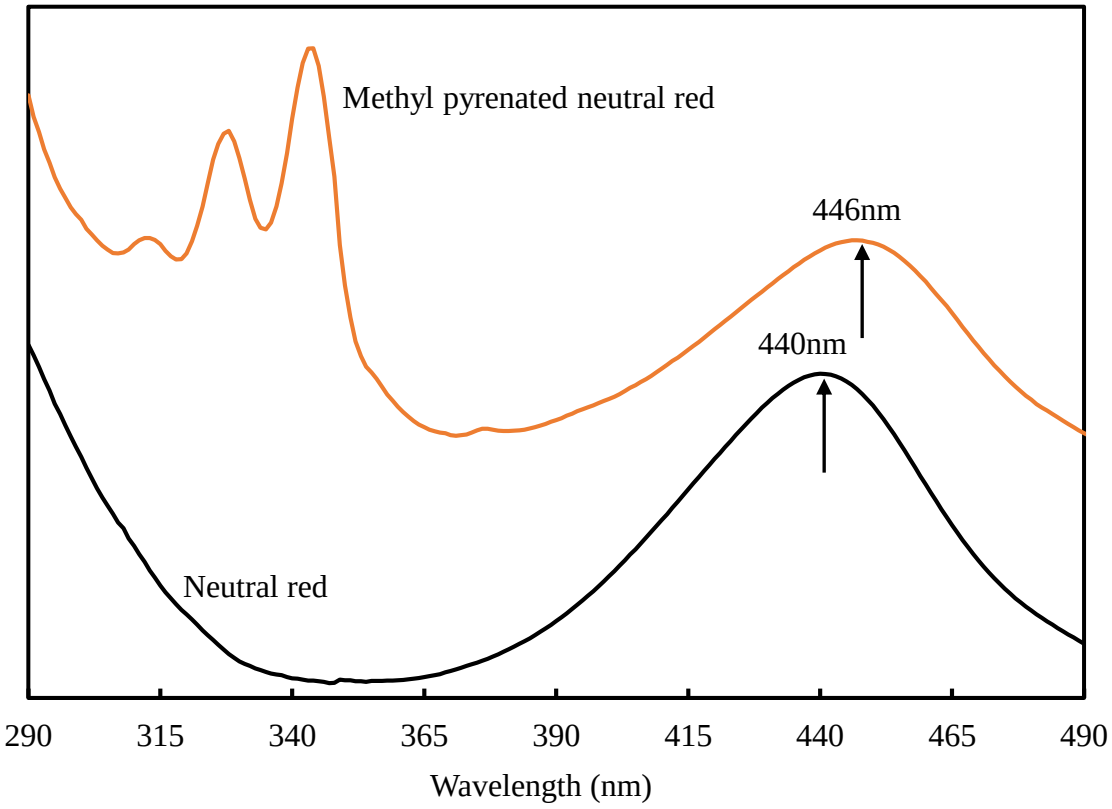

Figure 38: UV-Vis spectroscopy comparison of neutral red and neutral red derivative

The UV-Vis spectra show the attachment of pyrene ring to the neutral red and the shifting of neutral red peak maxima in derivatives. Overall, NMR, mass, and UV-Vis spectra strongly suggest that we synthesized the methyl pyrenated neutral red derivate.

3.3.2. PYRENATED NEUTRAL RED

A three-neck round bottom flask with an attached reflux condenser was charged with equivalent amounts of neutral red, Pd(dba)2, rac-BINAP, 1-bromopyrene and tert-sodium butoxide and placed under an atmosphere of argon. 15 ml anhydrous toluene was added to the reaction mixture through a septum and the reaction mixture was heated to 80 °C under stirring. The reaction mixture was put in an oil bath for 24 hours. After completion of the reaction, the mixture was cooled to room temperature. The reaction mixture was filtered through a silica plug with 80% ethyl acetate and 20% hexane. The resulting filtrate is vacuum evaporated on a rotary evaporator. The precipitate is then washed with hexane and the product was dried under vacuum for 24 hours.

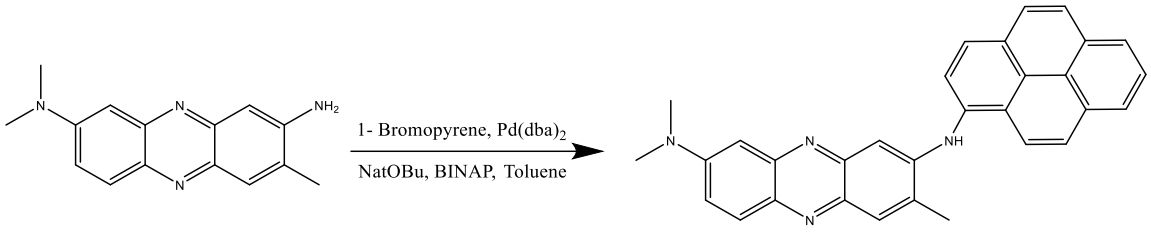

Figure 39: Synthesis of pyrenated neutral red

The product was analyzed for the verification of synthesis. The product shows the presence of pyrene substituted neutral red in mass spectrometry shown in Figure 40. But there is no significant presence of neutral red in the NMR spectroscopic analysis shown in Figure 41. This synthesis is deemed as unsuccessful.

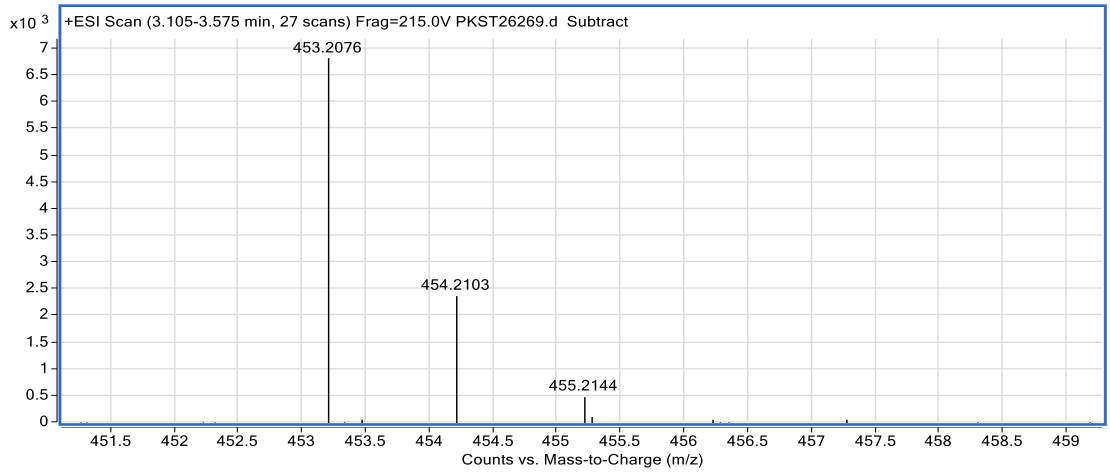

Figure 40: Mass spectrum of pyrenated neutral red derivative

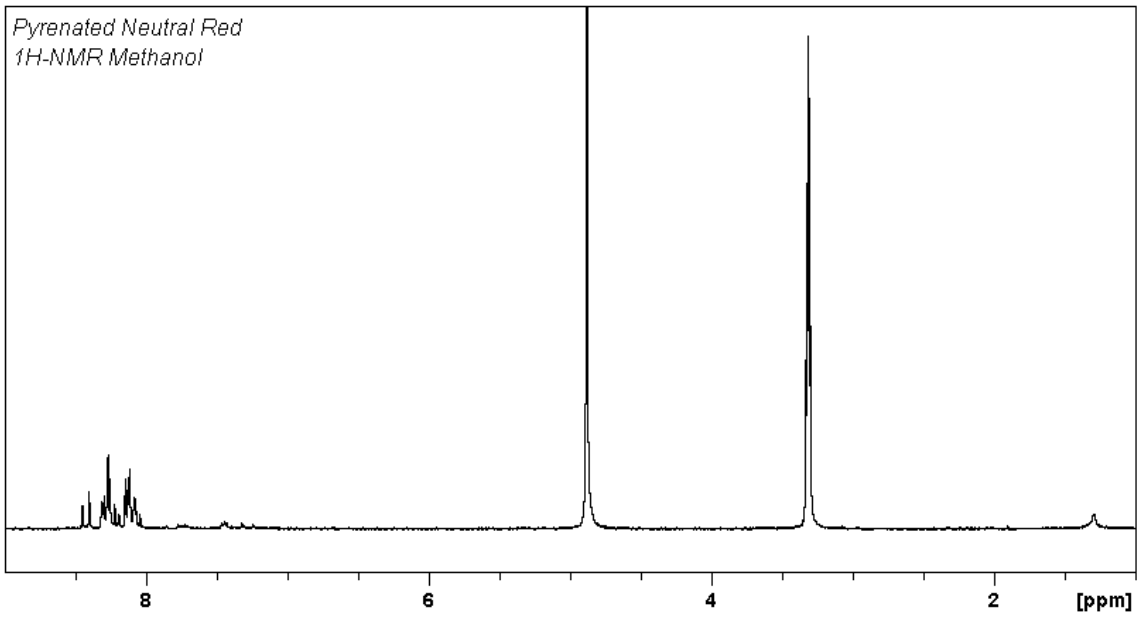

Figure 41: 1H NMR spectroscopy of pyrenated neutral red derivate

CHAPTER 4: ON THE ROLE OF IMPURITIES IN THE ELECTRIC AND SENSING PROPERTIES OF NANOCARBON FILMS

4.1. INTRODUCTION

Chemiresistive sensors are a type of chemical sensor where analyte interaction is measured by simple resistance change. Relatively easy fabrication, rapid prototyping, low-cost and availability of high precision resistance measurement circuits make chemiresistors a good choice for sensor applications. Chemiresistors have seen application in the field of gas sensing and biosensors.[75–78] Chemiresistive sensors are simply made from a substrate film or a modified substrate film and the analyte interactions happen at the surface of the substrate. Usually, the substrate surface is modified with other active species or the substrate itself takes part in sensing. Most common materials that are used as substrates are carbon nanotubes, organic semiconductors, graphene and different metal oxides films. [79–81] The substrate plays an important role in the sensing and the substrate parameters like substrate film dimension and impurities in the substrate need to be carefully controlled.

In our nanocarbon based redox chemiresistors, we will be modifying the substrate with redox active molecules and characterize the sensor performance by changing different substrate parameters. The goal of this study is to find a suitable substrate material for our sensors and explore the role of the substrate in sensing performance. The suitability of a substrate will depend on the ease of sensor fabrication, sensing response and interaction between substrate materials and the analyte. For ease of fabrication, adhesion between glass and substrate material, sensor preparation time and sensor film thickness will be taken into

consideration. The sensing response from different substrate materials will give useful information in selecting suitable substrate materials. We also want to study the interactions and sensing behavior of redox active molecules. For that, we need a substrate that has low levels of metal impurities and less substrate interaction with the targeted analyte. Studying the blank sensors will give information on substrate-analyte interactions. Sensors with different film thickness will be compared to find the role of substrate film thickness.

4.2. EXPERIMENTAL

4.2.1. SENSOR FABRICATION

Four different grades of carbon nanotubes, as well as graphene and pencil, were used to make sensors for comparison between different nanocarbon substrates. Two different batches of HiPco SWCNTs PO257 and PO343 purchased from Carbon Nanotechnologies Inc (Houston, TX), (6,5) chirality and 95% semiconducting enriched SWCNTs SG65i purchased from Sigma Aldrich and TUBALL SWCNTs obtained from OCSiAl substrate were used to fabricate nanotube sensors. Graphene nanoplatelets powder (product number:806668) purchased from Sigma Aldrich and 9B grade pencil manufactured by Bruynzeel Holland was used to fabricate graphene and pencil trace sensors.

The sensors were fabricated by following the standard procedures described in chapter 4 with different film thicknesses and thus sensors having different resistance. Nanographene was suspended in methanol by sonication and drop casted onto the glass and between two gold electrodes. 9B pencil was used to write onto frosted glass and between

two gold electrodes to make a sensor film. The sensors were aimed to be more conducting and the resistance of the dry film was targeted to be in the range of 50-250 Ω. For fabricated carbon nanotube and graphene sensors, the resistance of the dry sensing film was 50-300 Ω. The dimension of substrate films was maintained between 10-12 mm in length connecting two gold electrodes at 7.5 mm apart. The film width was maintained between 2-2.5 mm. It was not possible to make a pencil sensor with similar resistance due to its low binding/ adhesion to the glass surface. The resistance of the dry pencil film was 2573 Ω.

Different batches of carbon nanotubes were sonicated for different times depending on the bundle sizes and quality of finished materials. It is very hard to stick as produced carbon nanotubes onto a glass surface. With sonication, the adhesion properties can be improved as smaller bundles stick better to a glass surface. The TUBALL carbon nanotubes took 4 hours of sonication time to separate the bundles into smaller bundles. (6,5) semiconducting enriched single wall carbon nanotubes, HiPco SWCNT batch PO257 and PO343 took less than 1 hour of sonication time.

4.2.2. Conductivity Measurement

Conductivity measurements were carried out using a Keithley 2450 source meter and for analyte flowing through the sensor, a syringe pump was used. The syringe pump flow rate was set to 0.2 ml/min and 10 ml BD syringes were used for analyte flown to the sensors. A 5 mV bias was applied across two gold electrodes of the sensors to measure the current. For sensor programming with molecules, 20 minutes of methanol was flowed to clean the

sensor, 20 minutes of 1 mg/ml methanolic PCAT solution was flowed to deposit the PCAT onto the sensor and 10 minutes of methanol flush was used to remove any suspended PCAT particles from the sensor. For 0, 1 and 2 ppm free chlorine the analytes flowed for 30 minutes each. An I-V curve was also taken in between each analyte flown. The I-V curve was recorded from 1 mV to 100 mV potential with 10-points measurement data. Logarithmic potential step size was applied from 1mV to 100mV. For blank sensors, analyte was flown similarly except there was no PCAT deposition and methanol flush followed by PCAT deposition. Before the analyte was flown the blank sensors were cleaned with methanol for 20 minutes like the PCAT programmed sensors.

4.2.3. ANALYTE PREPARATION

The analyte was prepared from a reagent grade sodium hypochlorite solution which contains 10-15% available chlorine. Hypochlorite solution was purchased from Sigma Aldrich. Millipore water (18 MΩ) was used to prepare the analytes. 100 ppm free chlorine analyte was prepared from the stock solution and 1, 2 ppm solution was prepared using dilution from 100 ppm. There was no buffer used for the analytes and the pH of the analyte was not controlled. Since hypochlorous acid is a weak acid, the pH values for the prepared analytes were between 6.8 and 8.3.

4.3. RESULTS AND DISCUSSION:

4.3.1. SENSING COMPARISON

We tested three different grades of carbon nanotubes to compare between pristine and PCAT modified substrates.

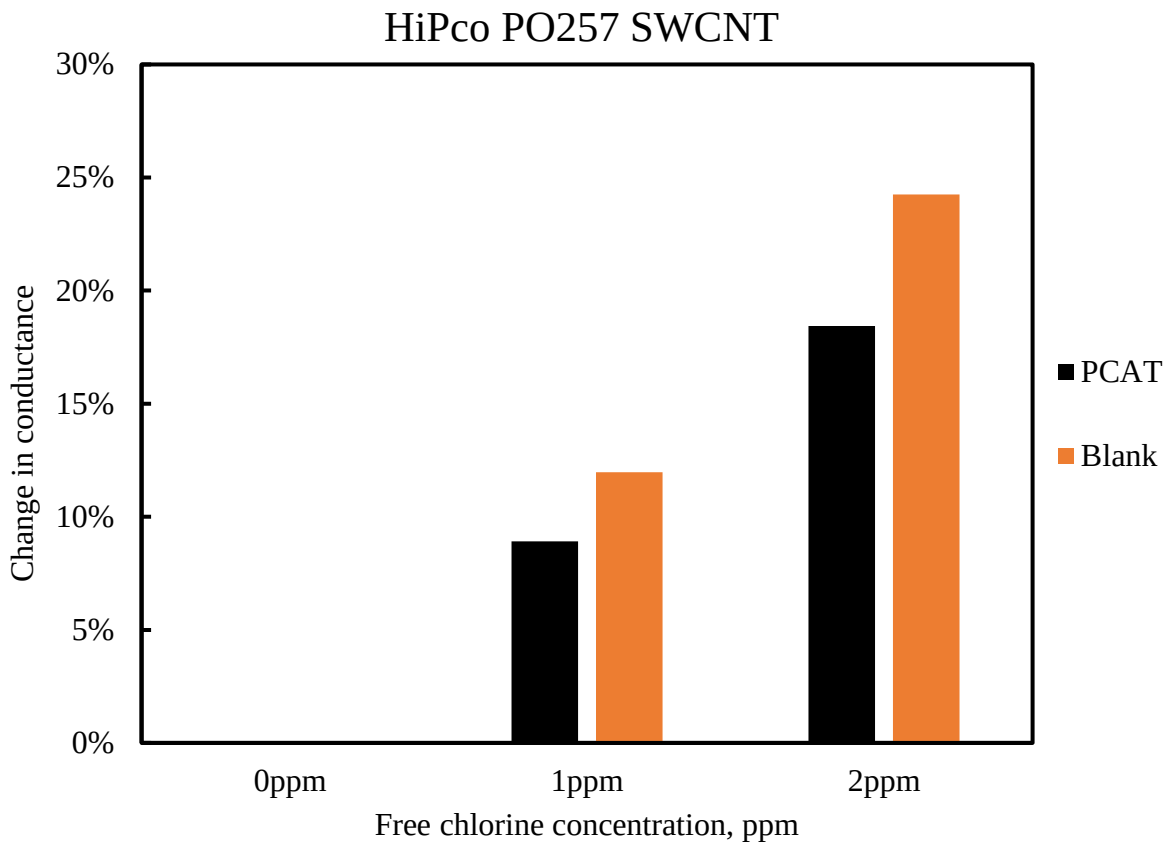

Figure 42: Comparison of blank and PCAT sensors from HiPco PO257 SWCNT

Figure 42 shows the sensing response comparison of HiPco carbon nanotubes. This nanotube sample was purchased from Carbon Nanotechnologies Inc and contains 14% total residual content. The nanotubes were synthesis by the HiPco process and contain redox active iron impurities. The resistance of the PCAT sensor film was 280 Ω and the sensor gives 9% and 19% sensing response for 1 ppm and 2 ppm free chlorine respectively. The resistance of the blank sensor film was 302 Ω and the blank sensor gives 12% and 24% sensing response for 1 ppm and 2 ppm free chlorine. The sensing response is calculated relative to the baseline response of 0 ppm standard for both sensors.

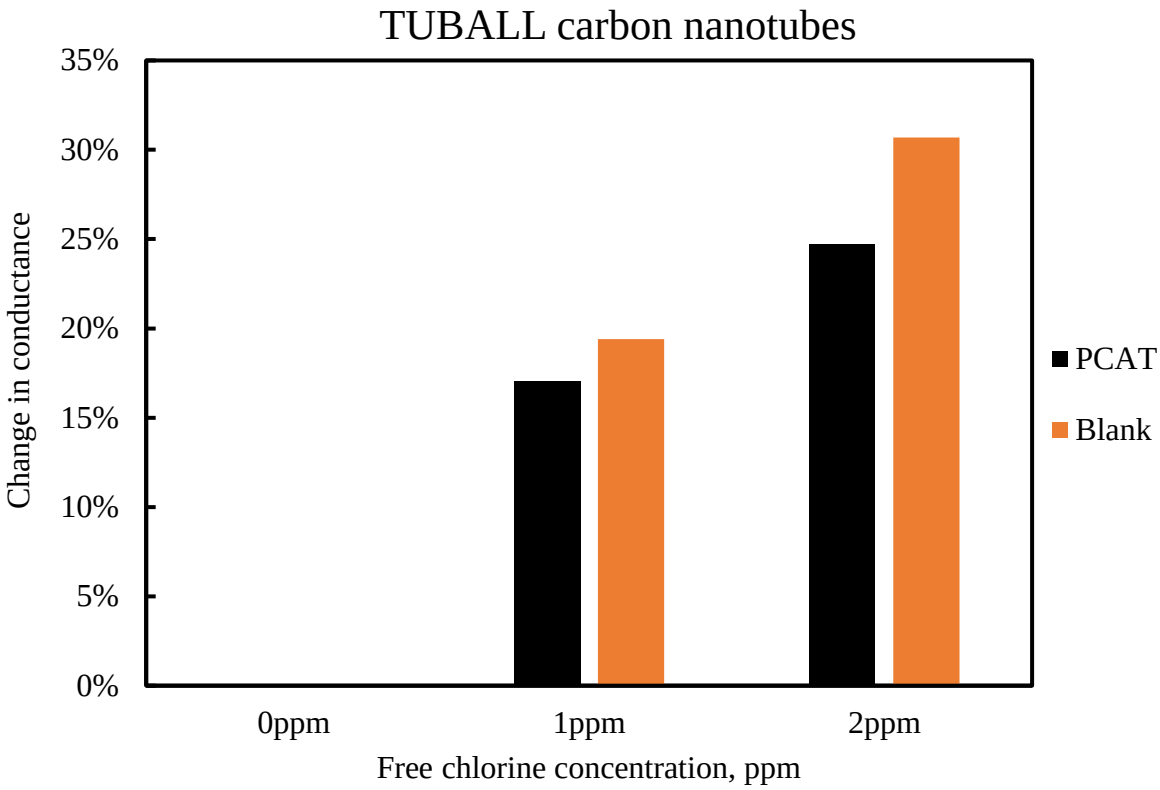

Figure 43: Sensing comparison of TUBALL carbon nanotubes blank and PCAT sensors

The sensing response comparison from TUBALL carbon nanotubes is shown in Figure 43. This is the cheapest batch of carbon nanotubes we used to make working sensors. This grade of nanotubes is mostly used as an additive in polymer composite, rubber, and other materials to improve the strength, electrical conductivity, and thermal conductivity. The price of TUBALL carbon nanotube is $8.70 per gram where by comparison 95% semiconducting SWCNT are sold for $1040.00 per gram. TUBALL carbon nanotubes are a mixture of 80% single wall carbon nanotubes and 20% multi-wall carbon nanotubes. They are synthesized via the HiPco process and are not very purified. The total carbon content is 85%, with 15% metal impurities. The resistance of the PCAT sensor film was 80 Ω. The

sensor gives 17% and 25% sensing responses for 1 ppm and 2 ppm free chlorine respectively. The resistance of the blank sensor film was 48.5 Ω. The sensor gives 20% and 30% sensing response for 1 ppm and 2 ppm free chlorine. The sensing response is calculated relative to the baseline response of 0 ppm standard. Overall TUBALL nanotubes have a higher sensing response compared to HiPco PO257 SWCNT.

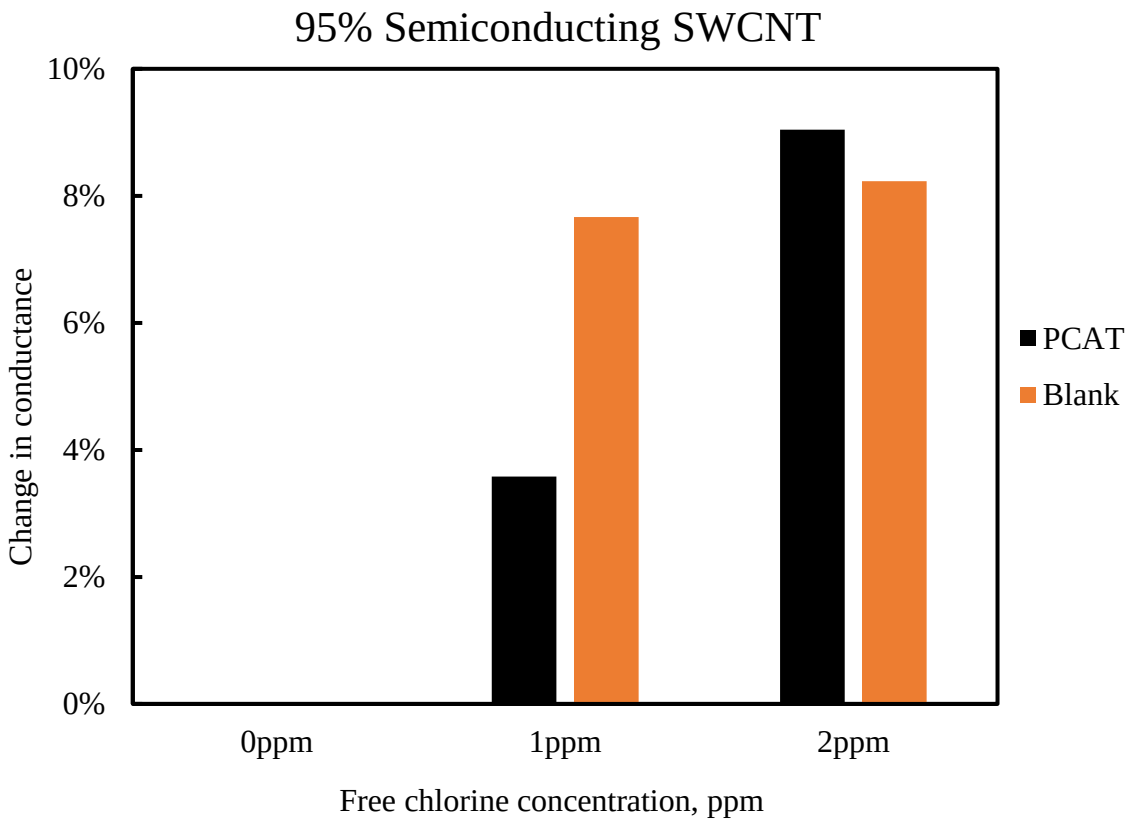

Figure 44: Sensing comparison from 95% semiconducting SWCNT blank and PCAT sensors

The sensing response of 95% semiconducting nanotubes is shown in Figure 44 for 1 ppm and 2 ppm free chlorine. The sensing response is calculated relative to the baseline response of 0 ppm standard. The carbon nanotube grade SG65i, synthesized by CHASM was used to prepare the sensors. This nanotube grade is produced by the CoMoCAT catalytic chemical vapor deposition method and semiconducting enriched with (6,5) chirality being most abundant. Even though these nanotubes are iron free they contain redox active species like cobalt and molybdenum. This grade of nanotubes has less than 5% total residual content. The resistance of the PCAT sensor film was 118 Ω. The sensor gives 4% and 9% sensing response for 1 ppm and 2 ppm free chlorine. The resistance of the blank sensor film was 184 Ω. The sensor gives 7.6% and 8.3% sensing response for 1 ppm and 2 ppm free chlorine. Semiconducting SWCNTs have the lowest sensing response in comparison to HiPco and TUBALL nanotubes.

4.3.2. Role of PCAT in Sensing Response

Comparing between the different grades of nanotubes it is seen that the PCAT sensors tend to have lower sensor responses than the blank sensors. It is known that carbon nanotubes are sensitive to their chemical environment. By functionalizing nanotubes with a redox active molecule, it is possible to make functionalized carbon nanotubes selective to redox agents. So, it was expected to see a synergy effect from both the substrate and redox active molecule. In fact, it looks like PCAT is dampening the sensing response instead of

increasing it. Higher blank sensor response could be possible due to impurities present in the nanotubes.

Metal catalytic impurities are easily incorporated into the bundles of nanotubes during the synthesis process.[82] Iron is used as catalyst in the HiPco synthesis process.[83] Nanotubes batches that are tested as sensors PO257 and TUBALL both contain around 15% total iron residual content. Elemental iron can easily react with free chlorine to produce iron chlorides ($FeCl_2$, $FeCl_3$) which are known to dope carbon nanotubes.[84,85] Moreover increasing the iron content was seen to increase the level of doping in nanotubes.[85] 95% semiconducting single walled carbon nanotubes have 5% metal impurities and they contain cobalt. There is an indication that metal impurities play a role in sensing. The higher the level of impurities the higher the sensing response. That also explains the higher sensing response of both HiPco PO257 and TUBALL nanotubes blank.

Elemental iron is in the nanotubes bundle and in the case of PCAT coating, we expect PCAT to coat nanotubes thoroughly and therefore decrease the level of accessibility of the metal impurities incorporated into carbon nanotubes. PCAT, which coats only at the nanotube surfaces, is expected to be in a much lower percentage than the metal impurities present in the bulk of nanotubes. The most of the interactions between redox molecule and oxidant will happen at the substrate film surface. Therefore, there could be a reduction of accessible redox species in the nanotube films. Also, it is possible that iron chloride has a stronger doping effect than PCAT, which explains the lower sensitivity of PCAT sensors.

From the sensing comparison between three different grades of nanotubes, it was found that only with 95% semiconducting nanotubes we can clearly observe the effect of PCAT molecule in terms of sensing response. Thus, we picked 95% semiconducting carbon nanotubes for further study. Also, a lower amount of metal impurities in 95% semiconducting nanotubes makes them the most suitable choice between the three grades of nanotubes.

We also compared between PCAT sensors from three different nanocarbon substrates: graphite, graphene and carbon nanotubes. The sensing comparison is shown in Figure 45. Graphene nanoparticles were used to make a graphene sensor substrate. The nanographene was sonicated in methanol and drop casted onto the glass. The resistance of the graphene film was 52.6 Ω and the sensor gives 2.2% and 3.23% sensing responses for 1 ppm and 2 ppm free chlorine respectively. A 9B pencil was used to write on the glass surface to make a pencil trace sensor. The resistance of the film was 2573 Ω. It was very hard to make a sensor with low resistance by writing on the glass surface. The pencil trace sensor gives 3.5% and 8% sensing response for 1 and 2 ppm free chlorine. In comparison to semiconducting nanotubes with graphene and pencil sensor, graphene has lowest sensing response whereas semiconducting nanotubes and pencil have a similar response.

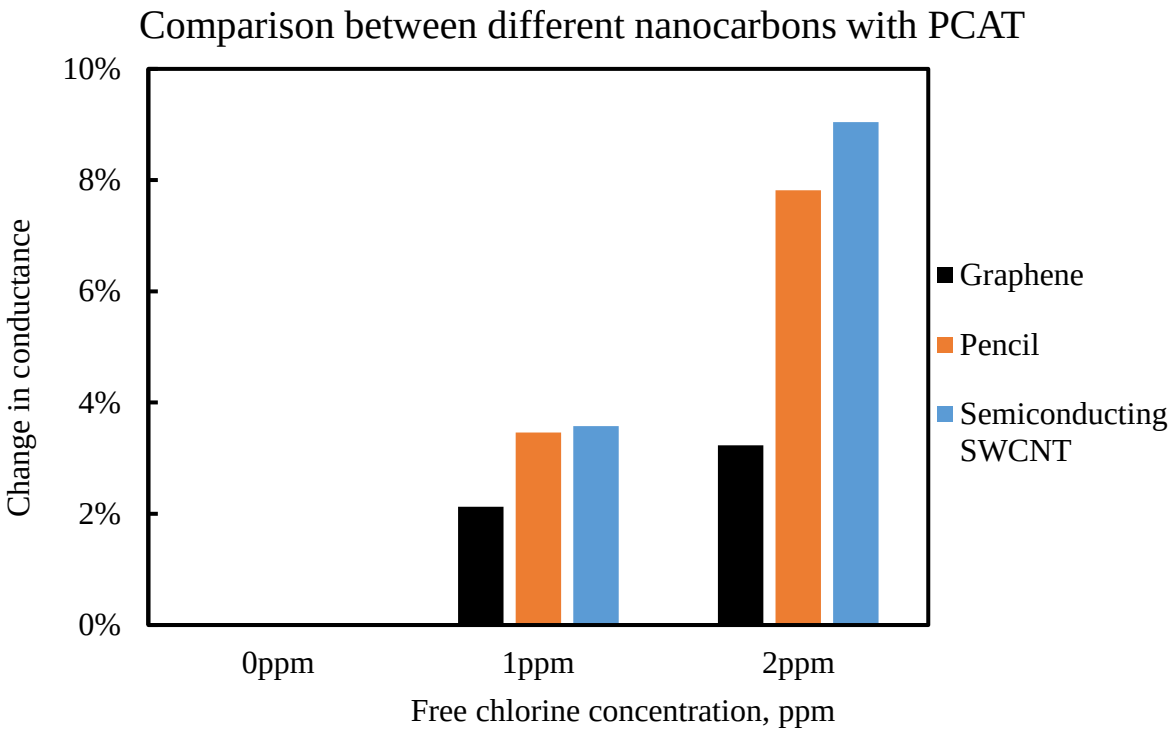

Figure 45: Sensing comparison between three different nanocarbon substrates with PCAT

It was difficult to make sensors from graphene due to their low adhesion to the glass surface. The graphene nanoparticles seem to fall apart from the nanographene substrates with time. On the other hand, the pencil is inexpensive and pencil sensors are easier to fabricate which makes pencil a good candidate for the sensor substrate. The problem is that pencil contains metal impurities and other additives which are unwanted while studying the interaction of molecule at surfaces. Though pencil may be a good choice, in the long run, we picked semiconducting carbon nanotubes here for further study.

4.3.3. ROLE OF SUBSTRATE FILM THICKNESS

Initially, thick nanotube films were used for the sensors. To study the effect of film thickness sensors with different film thicknesses were studied. No instrumentation was used to measure the film thickness. Film resistance and the film thickness are related to each other and film resistance was taken as a representation of film thickness. Substrate films with low resistance have more carbon nanotubes which form a thicker film whereas high resistance films contain fewer carbon nanotubes, therefore, a thin film.

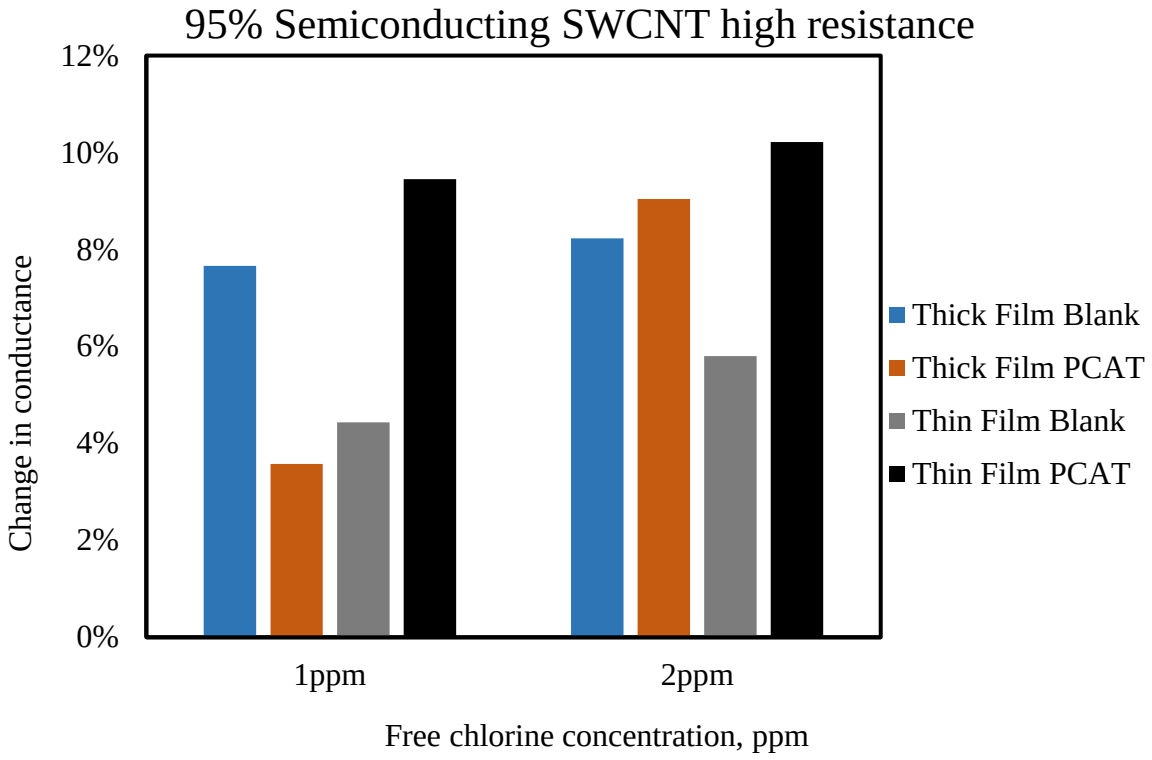

Figure 46: Sensing response comparison of a thin film carbon nanotube sensors

Sensing response comparison of a low resistance blank (184 Ω), low resistance PCAT sensor (118 Ω), high resistance blank (3937 Ω) and high resistance PCAT sensor

(2906 Ω) is shown in Figure 46. In case of the thick film we suspect that PCAT coating reduces the total accessible redox active species, therefore, we see a decrease in PCAT coated thick film substrate. With the thin-film sensor, we start seeing a higher effect of PCAT and the sensing response of thin film PCAT sensor is almost doubled in comparison to the thin film blank sensor. This is because in case of thin film we have a higher proportion of PCAT than the metal impurities present within the bulk of nanotubes and that might be the reason of sensor response increase from blank to PCAT coated film.

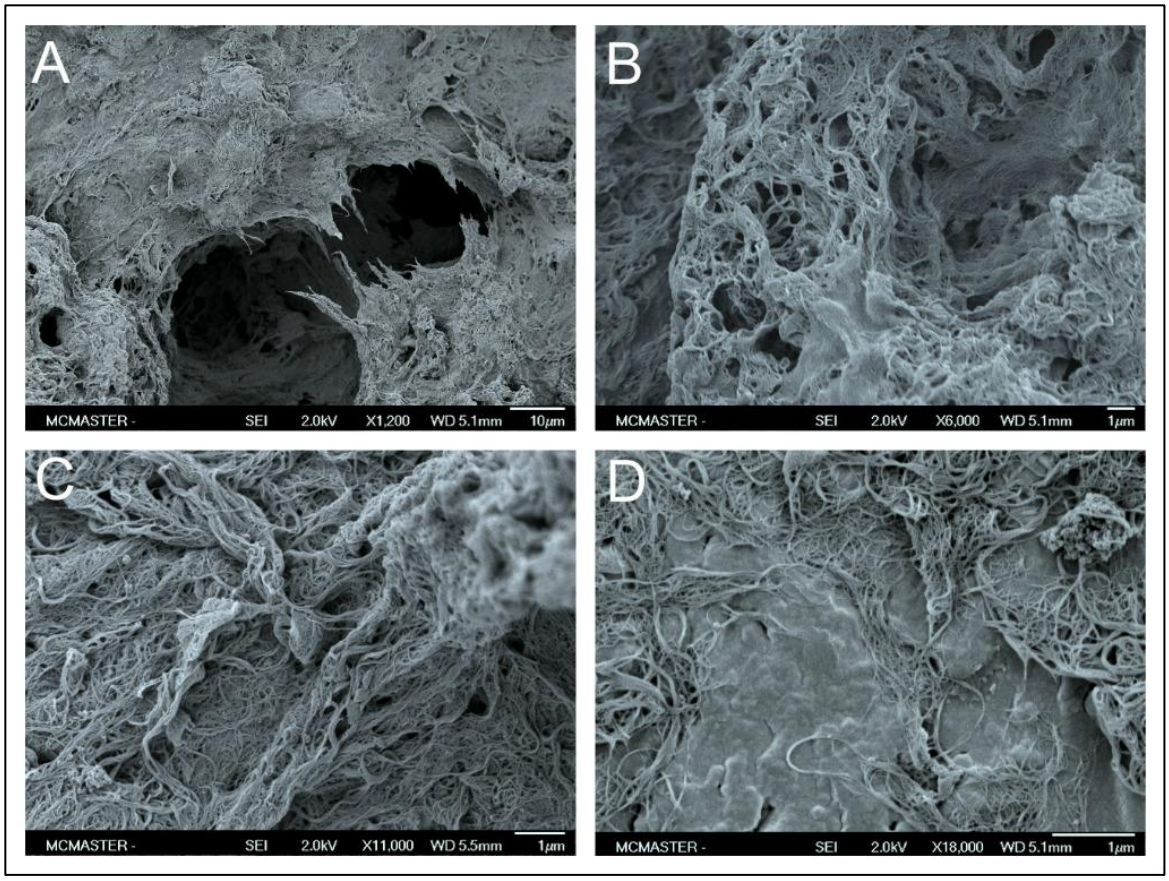

Figure 47: Morphology of a thick carbon nanotube film. A) Bulk film morphology, B) Aggregated nanotube bundles on the surface, C) Nanotube bundles, D) Nanotube film morphology at the contact.

The film morphology shows that there are excess nanotube bundles that don't contribute to the conductance of the substrate film but play a role in the sensing interaction. Also, thick films contain additional bundles of nanotubes which interfere with the analyte flow and the diffusion of species within the films. Figure 47 shows an example (D), at the edge of the contact between nanotube films and the gold electrode. We can see that a very

thin film is enough to make a network of bundles to study the change in resistance of the substrate film.

There is an effect of film thickness on the time constant of the sensing response. The sensing response against the time is shown in Figure 48. The thinner film has a faster sensing response than the thicker film. From the figure, we can see that the high resistance sensor has a faster sensing response and gives a saturation current for a specific analyte within ten minutes. On the other hand, the low resistance sensor takes a longer time to get to a saturation current value. If the sensor would have run for longer time overall sensor reponse could be similar as high resistance film. From this perspective, a high resistance i.e. low film thickness has advantages over a low resistance sensor due to the time constant.

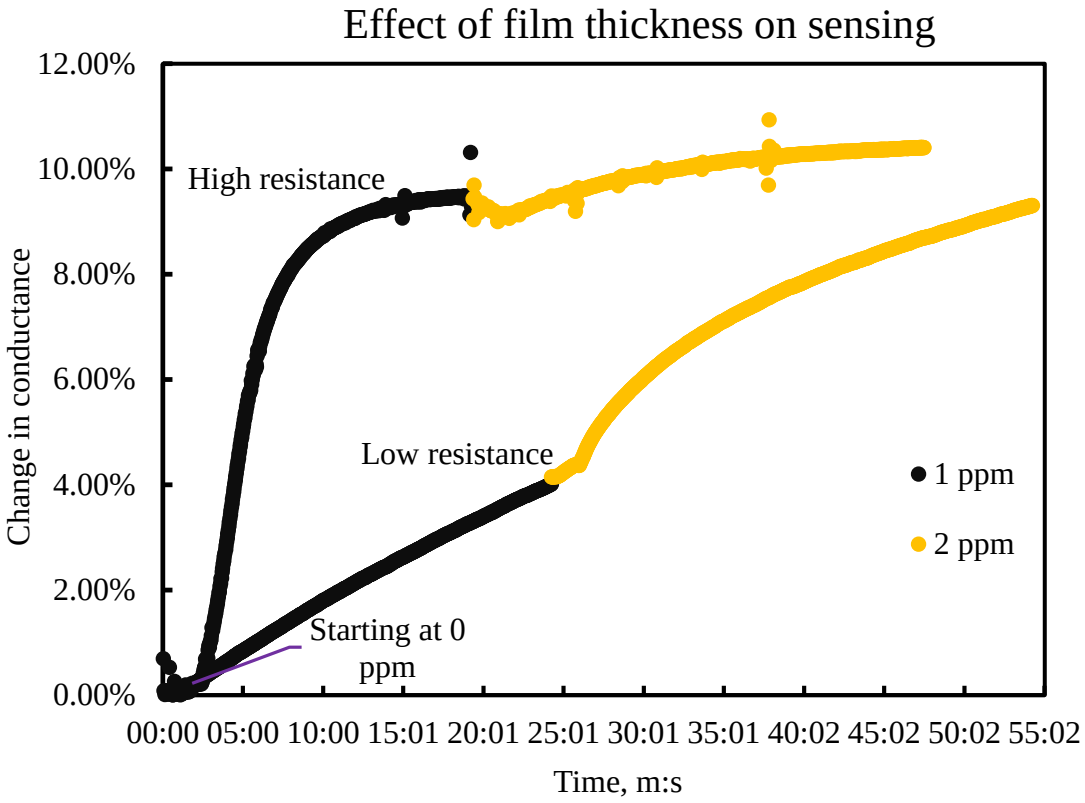

Figure 48: Effect of film thickness on the time constant of sensing response

4.3.4. Effect of Methanol

For sensor fabrication, we used Kapton double-sided tape to bind the glass substrate and PDMS microchannel. The Kapton tape is made of a polyimide film with a silicone adhesive. It is possible that the tape materials could be washed off during the methanol cleaning, molecule deposition, and methanol flush steps and deposited onto the sensor. So, the sensor could be contaminated with the tape material and it was checked to find if tape materials have any effect on the sensors. The experiment was done separately by another group member and it was found the tape material doesn't have any effect on sensing.

Inadvertently it was found that there is a significant effect of methanol contact in sensing response.

For blank sensors, we cleaned the sensor with methanol before flowing 0,1 and 2 ppm free chlorine. The sensor was also tested without any methanol contact. Figure 49 shows the sensor response comparison with and without any methanol contact.

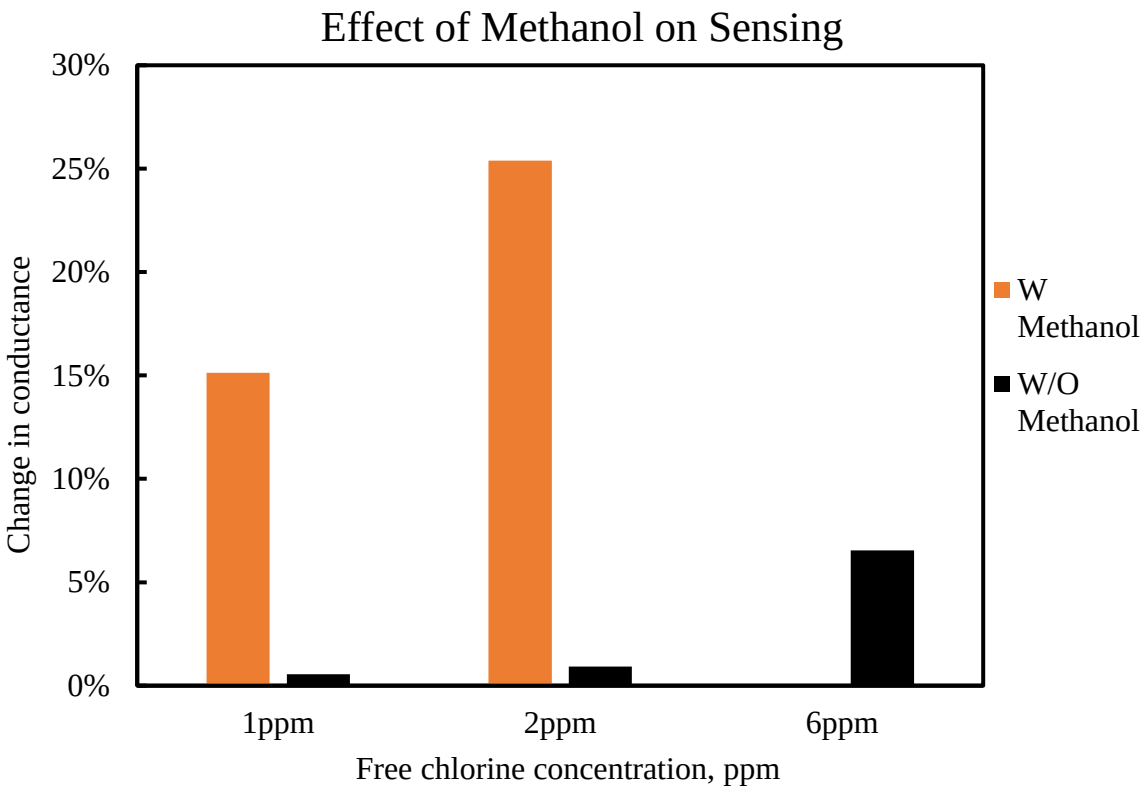

Figure 49: Sensing response comparison of HiPco PO343 SWCNT blank with and without methanol contact

A new batch of carbon nanotubes was used for this experiment. This batch of HiPco nanotubes was purchased from Carbon Nanotechnologies Inc and contains 5% total residual content. The sensor where methanol was used for sensor cleaning gives 15% and 24% sensing response for 1 ppm and 2 ppm free chlorine. Whereas, the sensor without any methanol contact barely gives any sensing response for 1 ppm and 2 ppm free chlorine. Higher chlorine concentration was tested and for 6 ppm free chlorine the sensor gives a 7% sensing response.

In comparison to the sensor with methanol contact, it is clear that methanol has a significant effect on the sensor response. The actual effect of methanol on the sensor is unknown. Carbon nanotubes are hydrophobic; therefore, a likely explanation is that methanol facilitates surface wetting by the aqueous analyte to interact with the bundles of carbon nanotubes. Also, from the film thickness discussion earlier we can see that the contact between nanotubes and analyte influences the sensing response.

4.4. SUMMARY:

In summary, we have tested three different grades of carbon nanotubes and studied the effect of metal impurities on the sensing response. Metal impurities play a significant role in the sensing response. Increased metal impurities result in an increase in sensing response. We also compared three different nanocarbon substrates. 95% semiconducting SWCNTs were found to be a suitable choice as a sensor substrate. The role of redox active molecule PCAT was explored with blank and modified sensors. Film thickness has a role in sensing

response time. Thin films have a faster sensing response and thick films have a slower sensing response. Surface wetting has a significant role in overall sensing response. It was found that a PCAT modified thin nanotube film works better as a sensor.

CHAPTER 5: IDENTIFICATION AND QUANTIFICATION OF DISINFECTANTS BASED ON REDOX CHEMIRESISTIVE SENSORS.

5.1. INTRODUCTION

Redox-active molecules are the active species in our sensing devices. Our proposed strategy is to change the redox potential of the redox molecules and correlate their sensing performance with the change in potential. Oligoanilines are a class of redox-active molecules that has seen many applications in sensing, corrosion inhibition, and organic electronics. In this research project, we will compare sensor performance of five redox active molecules. Among the redox-active molecules, two are aniline dimers and two are aniline tetramers and another is a triaryl methane derivative.

Phenyl capped aniline tetramer (PCAT) has been used previously in sensing and corrosion inhibition studies by other group members.[1,86,87] Its redox activity and surface interaction is well known to us. Therefore, PCAT serves as the model redox active molecule in this study. Replacing one of the benzene rings with a large conjugated anthracene ring will result in a shift in redox potential. Hence, we choose to study anthracene substituted PCAT (APCAT). N, N′-Diphenyl-1,4-phenylenediamine (DPPD) is another redox active aniline dimer which is readily available and was studied in our group for application in corrosion inhibition.[88] DPPD is shorter oligoaniline than PCAT, it has two aniline groups, therefore, it will have a slightly different redox potential. Adding one extra conjugated system in DPPD would give us further control over the electronic structure. Hence, we

picked readily available N,N'-Diphenyl-4,4'-bi phenylenediamine (SDPPD) to study as one of our redox active molecules.

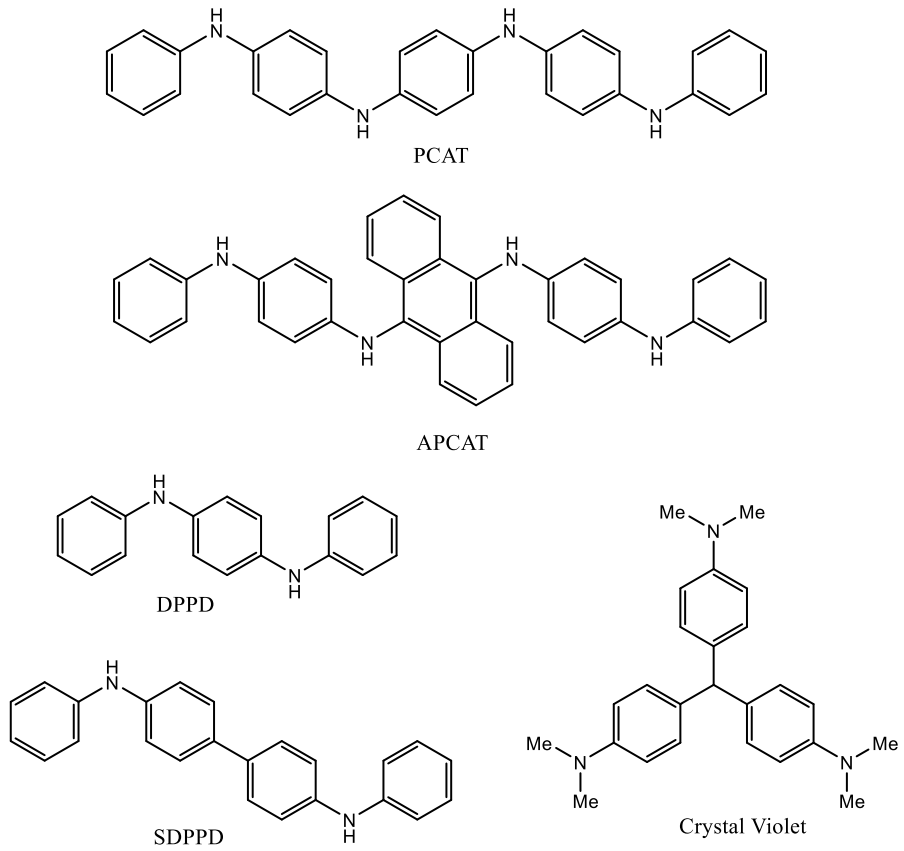

Figure 50: Redox active molecules

All four of our redox active molecules are aniline compounds and they are responsive in our targeted analyte pH range of 5 to 11. In contrast, crystal violet is a redox active molecule that is not sensitive to pH in that range. It is cheap and readily available. Its redox activity and interaction with nanocarbon are well known.[89,90]

Spectroscopic and electrochemical properties of the redox active molecules will be explored in this chapter and compared to the sensing response to disinfectant chemistry. Differentiating between different disinfectants will also be discussed based on sensor characterization.

5.2. EXPERIMENTAL

5.2.1. MATERIALS

The sensors were fabricated following the sensor fabrication SOP on chapter 4. (6,5) chirality and 95% semiconducting enriched SWCNTs SG65i purchased from Sigma-Aldrich were used to make sensor substrates. The resistance of sensor substrate films was in the range of 0.9-3 kΩ. PCAT and APCAT were synthesized in our lab and used after characterization (see chapter 3). DPPD, SDPPD and crystal violet were purchased from Sigma-Aldrich.

5.2.2. UV-VIS SPECTROSCOPY

About 10 mg of the molecule was dissolved to give 20 ml of solution in acetonitrile and sonicated for around 5 minutes to dissolve any suspended particles. Necessary dilution was done in some cases. A Cary 100 UV-Visible spectrometer was used for the spectroscopic analysis. The single beam was used and the scanning window was set to 800-200 nm. A quartz cuvette was used and the spectrometer was set to blank calibrated with pure acetonitrile solvent.

5.2.3. ELECTROCHEMISTRY

Cyclic voltammetry and differential pulse voltammetry were done in a nonaqueous medium using 0.1 M tertbutyl ammonium perchlorate (TBAP) supporting electrolyte and 0.02 mM diphenyl phosphate proton source in acetonitrile solvent. The working electrode was a platinum disk (0.785 mm^2 area) and a platinum wire was used as a counter electrode. A non-aqueous $Ag/AgNO_3$ electrode was used as reference electrode. The reference electrode was made from an Ag wire dipped into 10 mM $AgNO_3$ and 0.1 M TBAP base electrolyte in acetonitrile solution. Ag wire was placed into a glass tube sealed with porous Teflon tip and the glass compartment was filled with $AgNO_3$ electrolyte solution. EmStat was used for the cyclic voltammetry and for data acquisition PSTrace software was used. For cyclic voltammetry scan rate of 0.1 V/s and step size of 0.005 V was used. For DPV, E step of 0.005 V, E pulse of 0.1 V, t pulse of 0.05 s and scan rate of 0.01 V/s was applied. The experimental window was set between -1.5 V to +1.5 V. Argon was purged to remove any interference from air oxidation. The experiment was performed inside a Faraday cage equipped with argon purging and stirrer.

Experimental procedure: 15-20 ml 0.1 M TBAP solution was placed into the sample holder. The platinum working electrode was polished, cleaned and dried carefully. The reference electrode and the working electrodes are also cleaned and dried before submerging into the electrolyte. Platinum disk, platinum wire, and $Ag/AgNO_3$ electrode were submerged into the electrolyte solution and hanged from the electrode holder cap. The electrolyte solution was then purged with argon for at least 5 minutes. A scan was run in absence of molecule and afterward, 0.1 mM solute was added to the solution. The solution

was stirred for 5 minutes and purged with argon for another 5 minutes. The argon blanket was always turned on during the experiment to maintain inert conditions in the electrochemical cell. The scan rate was adjusted in between 0.1 V/s to 0.2 V/s and all other parameters were kept the same.

5.2.4. CONDUCTIVITY MEASUREMENT

A Keithley 2450 sourcemeter was used to measure the conductivity. A very small bias of 5 mV was applied across two gold electrodes of the sensor for current measurement. The analyte was flown through the sensor using a syringe pump. The flow rate of the syringe pump was set to 0.2ml/min. The analytes were flown until a stable saturation current was reached.

5.2.5. ANALYTE PREPARATION

Two different types of analytes were used for this project. Different disinfectant concentrations at constant pH and different pH analytes at constant concentration. Two different disinfectants were used in this chapter. Free chlorine solutions were prepared from reagent grade sodium hypochlorite solution (Sigma-Aldrich) which contains 10-15% available chlorine. $KMnO_4$ solutions were prepared from 99% potassium permanganate crystal (ACP Chemicals), reagent grade. Different concentrated disinfectants (0.5, 1, 2, 4 and 8 ppm) were prepared in 0.005 M phosphate buffer at pH 7.5. 1 ppm free chlorine and 1 ppm $KMnO_4$ solutions at different pH were also prepared from 0.005 M phosphate buffer. The pH of the buffer was adjusted by adding 0.1 M HCl and 0.1 M NaOH solutions.

5.2.6. SENSOR PROGRAMMING WITH REDOX-ACTIVE MOLECULE

For characterizing the sensor performance of a molecule, we first program the sensor by depositing the molecule. The molecule non-covalently functionalizes the carbon nanotubes and interacts with the environment present.

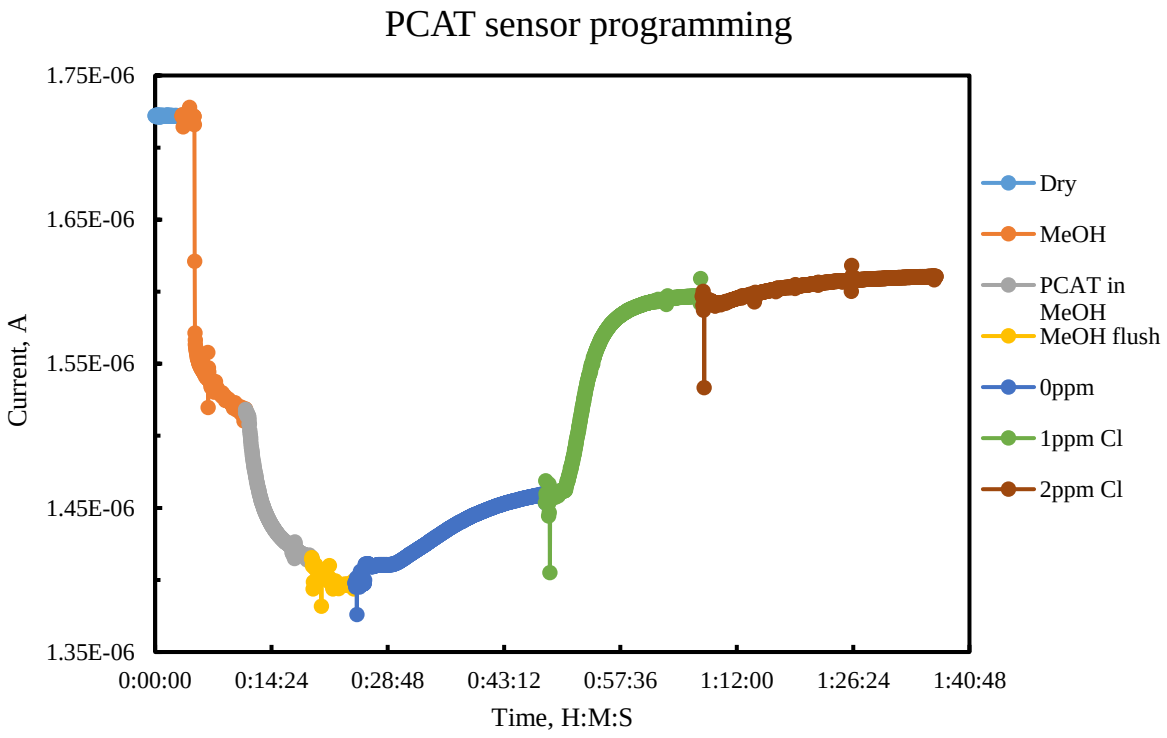

Figure 51: Sensor programming with redox active molecule

The plot in Figure 51 shows a sensor being programmed with PCAT molecules. The plot shows the measured current across the carbon nanotube films for different analytes and the horizontal axis shows the time of an analyte flown through the sensor. To prepare a sensor methanol is flown first to wet the sensor and make sure that it is clean. Then a methanolic solution of PCAT is run through the sensor to deposit the molecules. There is a

drop in current from just methanol to the methanolic PCAT solution which is shown in gray. When the sensor saturates with molecules the current stabilizes. After the PCAT deposition, the sensor is flushed with methanol to make sure the sensor is free of any suspended particles from the methanolic solution. A 0.005 M, pH 7.5 phosphate buffer solution in absence of any oxidant was run to get a 0 ppm baseline current. We see an increase in sensor current from methanol to 0 ppm which might be due to the change in surface wetting by different solutions. After that 1 ppm and 2 ppm, free chlorine solution shows an increase in current which is shown in green and maroon color.

5.3. MOLECULE CHARACTERIZATION

5.3.1. HOMO-LUMO GAP FROM UV-VIS

UV-Visible spectra of molecules are given below. The HOMO-LUMO gap was calculated from λ_{max}.

The observed spectrum of DPPD is shown in Figure 52. The λ_{max} is found at 304 nm for DPPD. The calculated HOMO-LUMO gap is 4.07 eV from the electron transition at 304 nm.

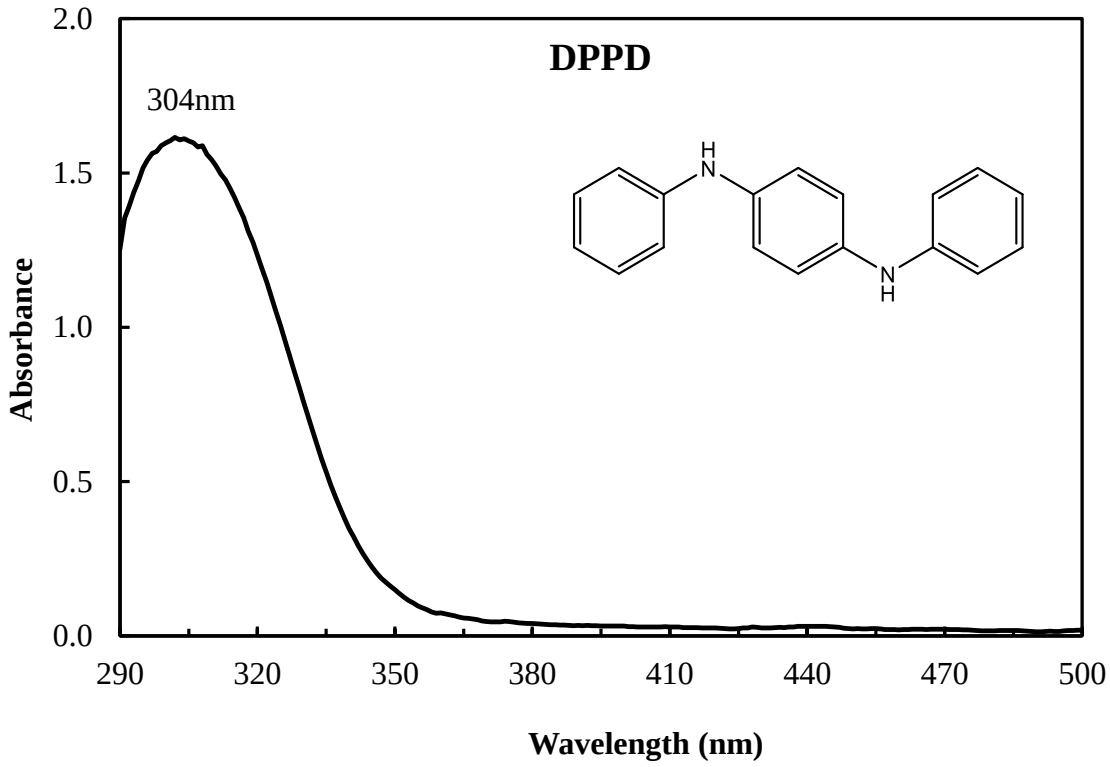

Figure 52: UV-Vis spectrum of DPPD in acetonitrile.

The observed UV-Vis spectrum of SDPPD in acetonitrile is shown in Figure 53. One extra conjugation at the middle ring of DPPD results in a red shift and the λ_{max} is found at 330 nm. The calculated HOMO-LUMO gap from the electron transition is 3.75 eV.

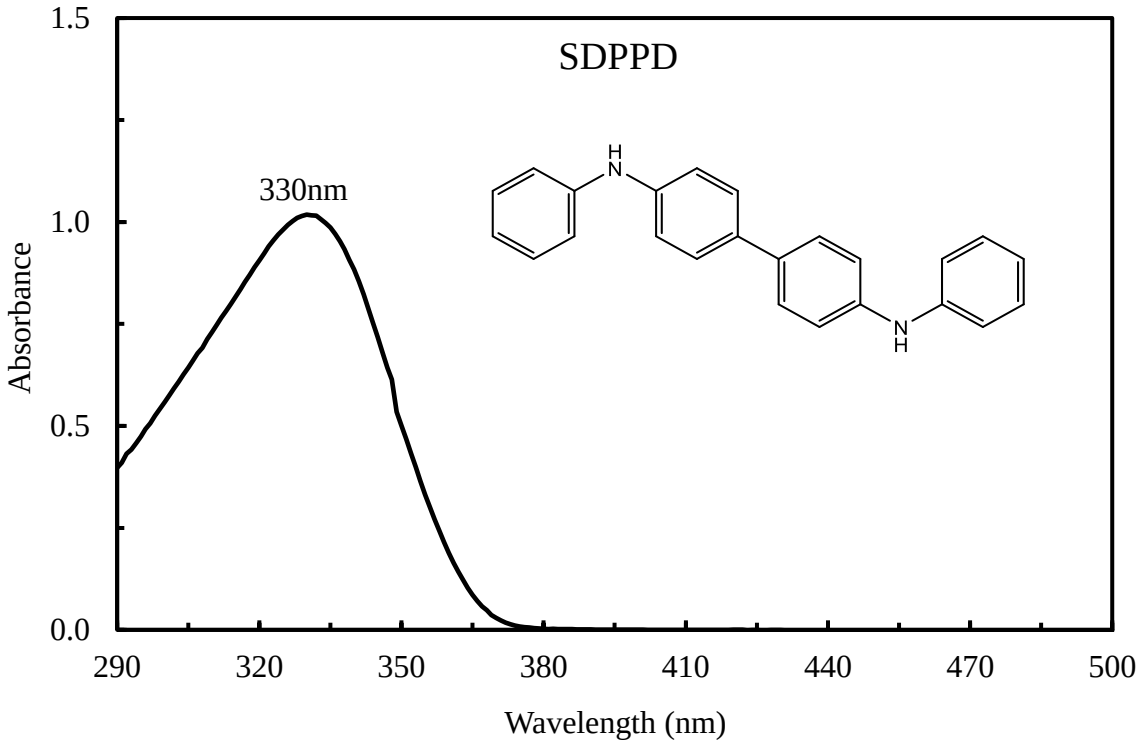

Figure 53: UV-Vis spectrum of SDPPD in acetonitrile.

The observed spectrum of reduced PCAT is shown in Figure 54. PCAT is a molecule having two more aniline groups than DPPD. Thus, PCAT is a molecule with longer conjugation and a red shift is seen in λ_{max}. The λ_{max} for PCAT is found at 320 nm and the calculated HOMO-LUMO gap for electron transition is 3.87 eV.

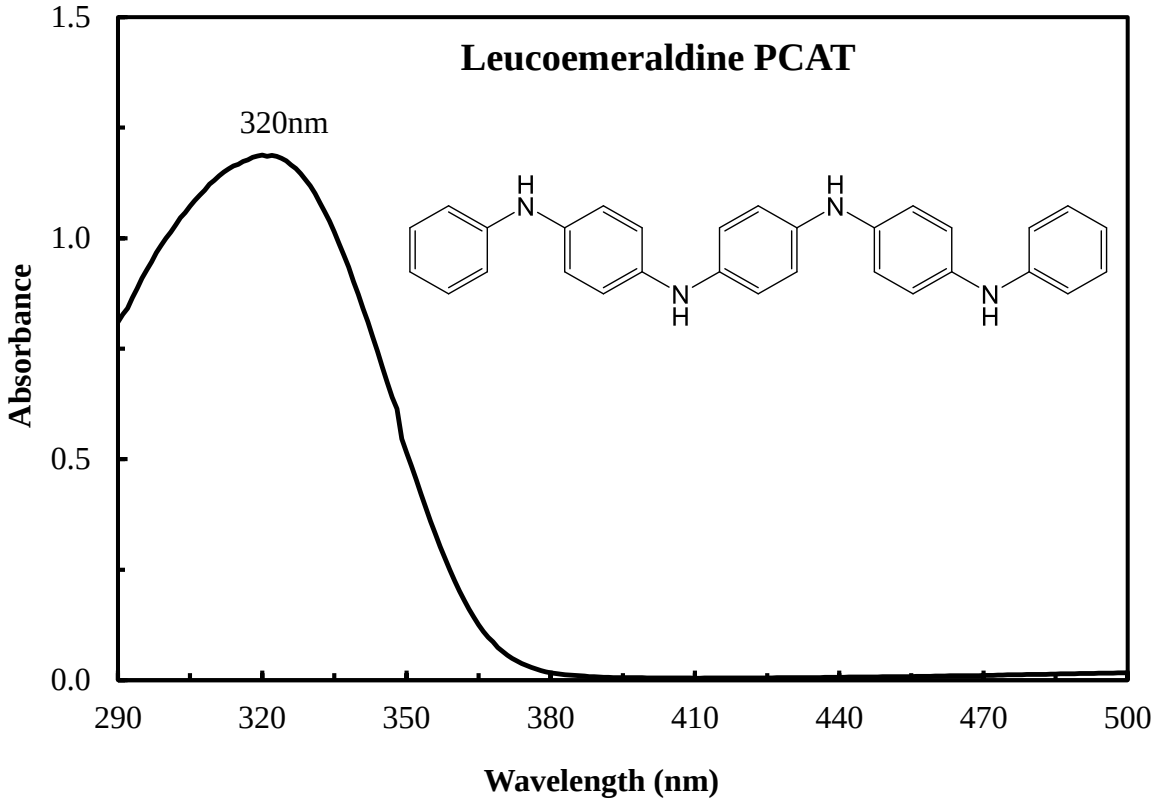

Figure 54: UV-Vis spectrum of Leucoemeraldine PCAT base in acetonitrile.

The observed UV-Vis spectrum of emeraldine PCAT is shown in Figure 55. There are two electron transitions seen in the spectrum at 305 nm and 565 nm. The first electron transition at 305 nm is assigned to $\pi \rightarrow \pi^*$ and the second electron transition at 565 nm is believed to be due to the formation of molecular exciton.[58] The exciton forms due to the charge transfer to the quinoid rings from the adjacent benzenoid rings. The molecular exciton is the characteristic electron transition for the emeraldine oxidation state. The λ_{max} at 305 nm has a calculated HOMO-LUMO gap of 4.06 eV.

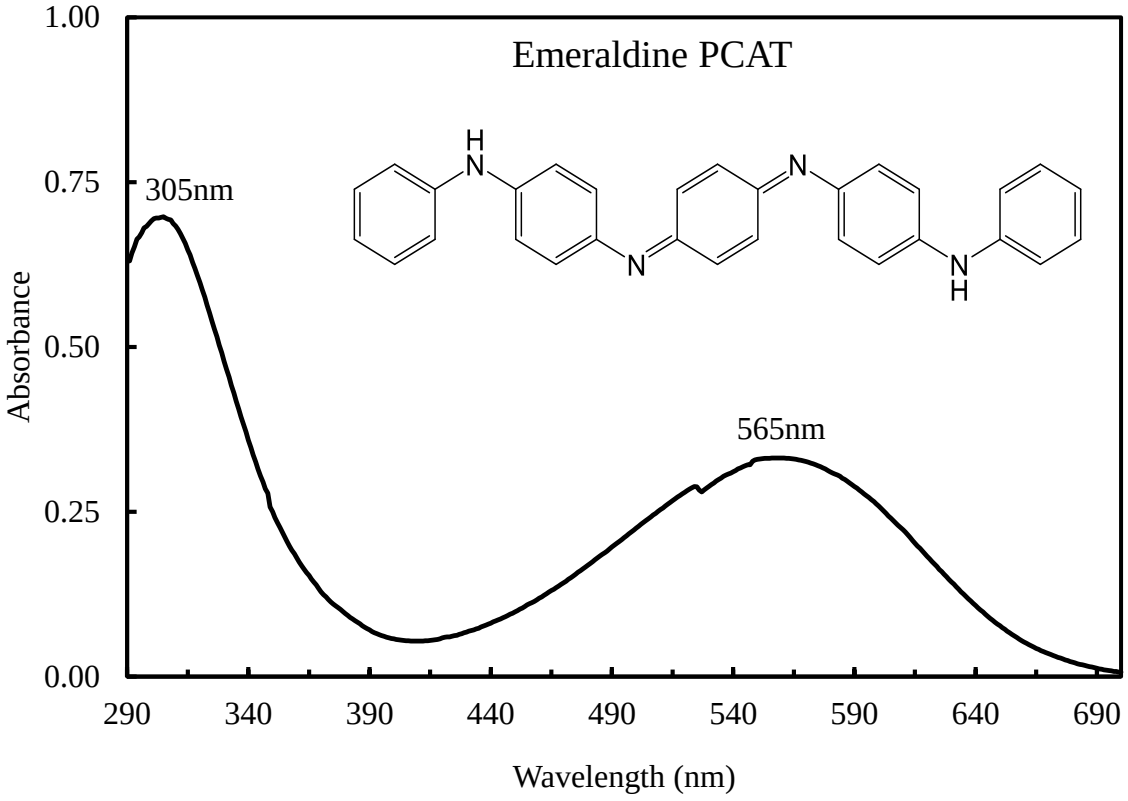

Figure 55: UV-Vis spectrum of emeraldine PCAT base in acetonitrile.

The UV-Vis spectrum of half oxidized APCAT is shown in Figure 56. Like half oxidized PCAT, a characteristic molecular exciton for emeraldine oxidation state and one $\pi \rightarrow \pi^*$ transition is seen. The first electron transition is seen at 295 nm and the molecular exciton is seen at 465 nm. The molecular exciton is formed by charge transfer to the anthraquinone ring from the adjacent benzenoid rings. The λ_{max} at 295 nm has a calculated HOMO-LUMO gap of 4.20 eV.

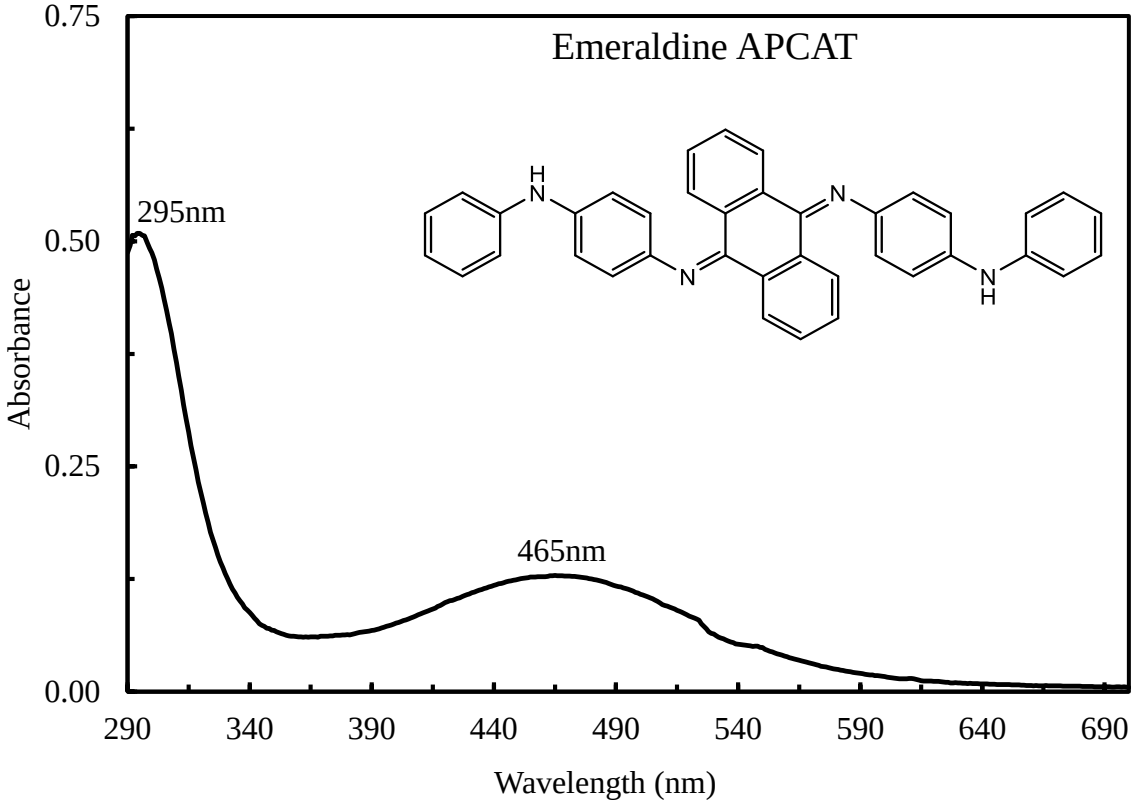

Figure 56: UV-Vis spectrum of emeraldine APCAT base in acetonitrile.

The observed crystal violet spectrum is shown in Figure 57. The characteristic absorption of visible light at 586 nm for crystal violet is seen with one shoulder at 550 nm. The absorption peak at 303 nm is also shown in the spectrum. The discontinuites at 352 nm and 528 nm are due to instrumental malfunction. The λ_{max} at 584 nm has a calculated HOMO-LUMO gap of 2.12 eV.

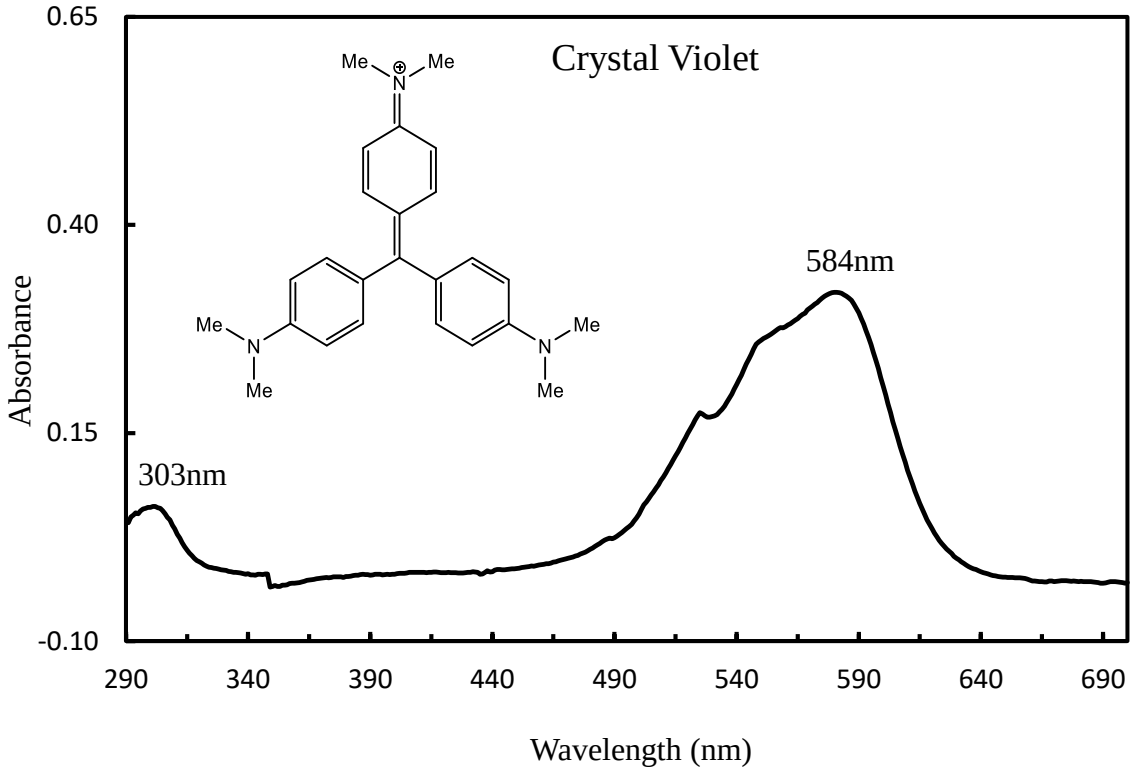

Figure 57: UV-Vis spectrum of crystal violet in acetonitrile.

5.3.2. ELECTROCHEMICAL CHARACTERIZATION

The electrochemical properties of redox-active molecules are discussed here based on the cyclic voltammogram and differential pulse voltammogram. All the voltammograms are reported relative to internal ferrocene standard. The CV and DPV show a ferrocene redox peak at 0.0975 V relative to the $Ag/AgNO_3$ reference electrode. All the CV and DPV measurements were done in 0.1 M tertbutyl ammonium perchlorate (TBAP) supporting electrolyte and 0.02 mM diphenyl phosphate as a proton source in acetonitrile solvent. For cyclic voltammetry, a scan rate of 0.1 V/s was used. For DPV an E_{pulse} of 0.1 V and a scan rate of 0.01 V/s was applied.

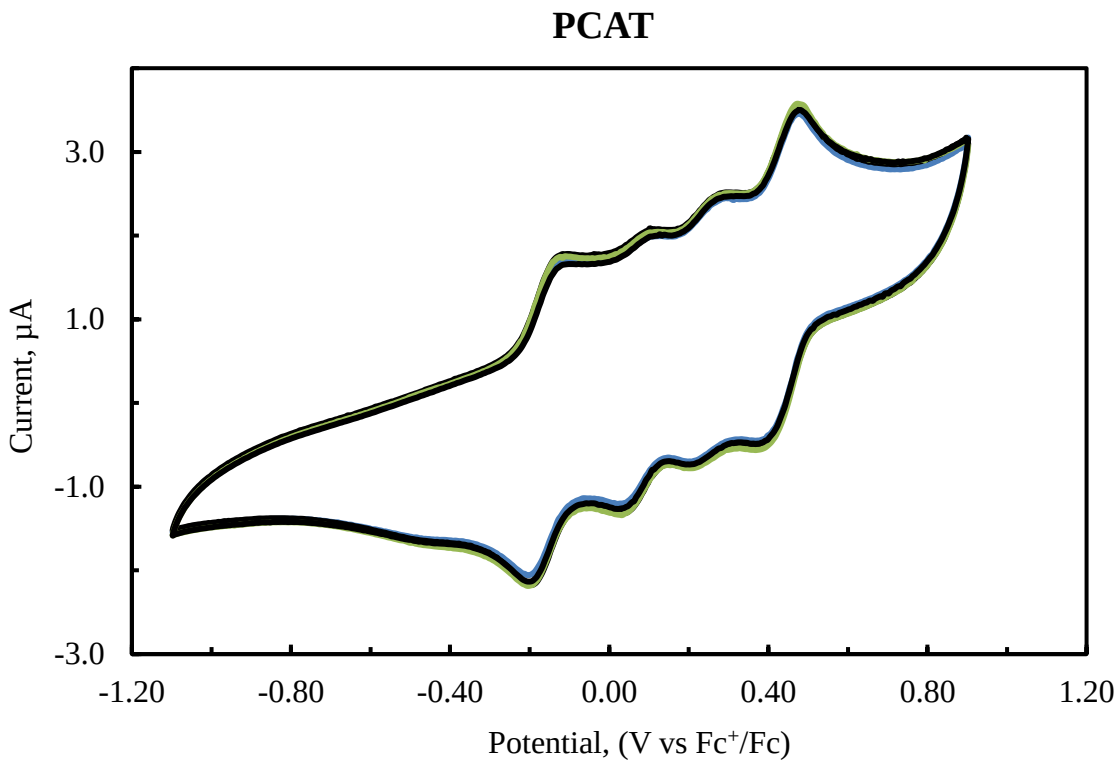

Figure 58: Cyclic voltammogram of PCAT in acetonitrile

From the cyclic voltammetry data for PCAT, four induvial peaks are seen and the oxidation-reduction process is reversible. The oxidation of PCAT is a four-electron process and each peak can be associated with an individual one electron process from leucoemeraldine base oxidizing to the pernigraniline base. The voltammogram found is consistent with the literature and can be explained by four individual one electron processes.[91] The following redox mechanism in Figure 59 shows the oligoaniline oxidation from the amine to imine.

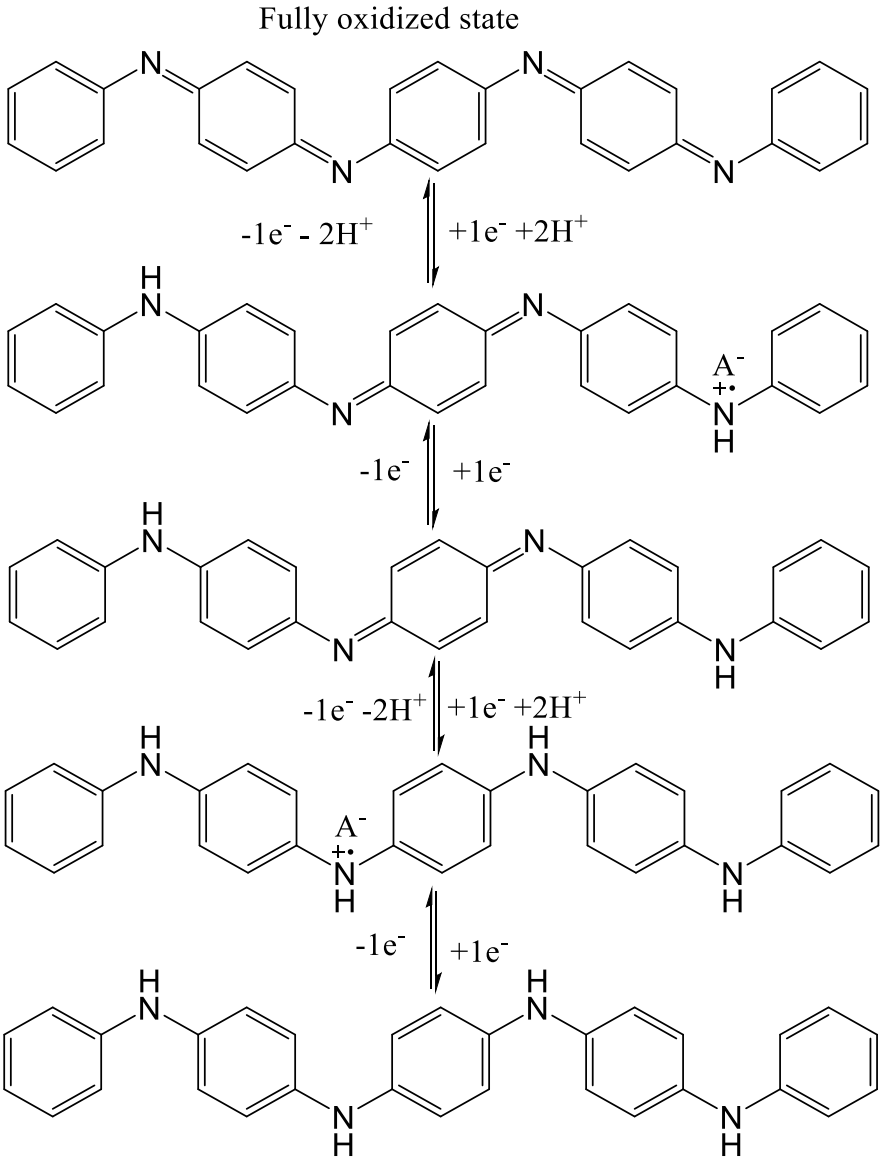

Figure 59: PCAT redox process mechanism

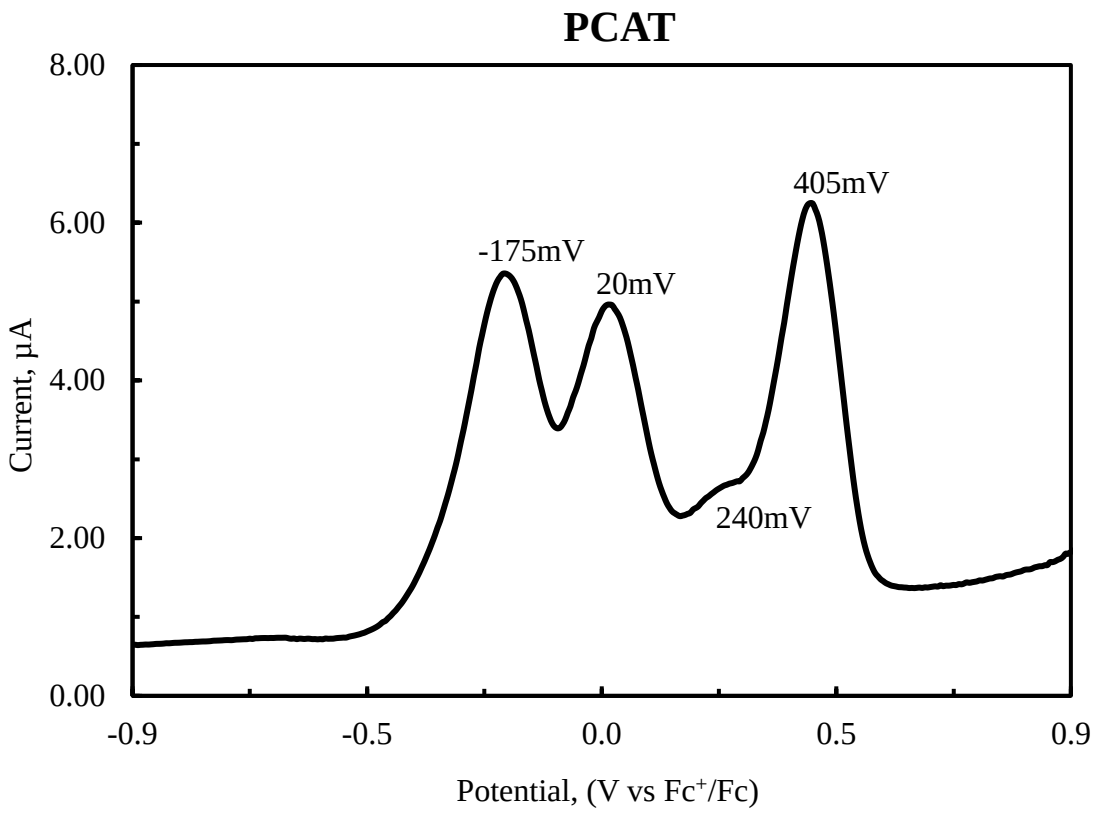

Figure 60: Differential pulse voltammogram oxidation scan of PCAT in acetonitrile

The differential pulse voltammogram of PCAT shows four peaks in the oxidation scan. Four oxidation peaks are found to be at -175 mV, 20 mV, 240 mV, and 405 mV. Each individual peak can be assigned to a one electron process from PCAT being gradually oxidized from leucoemeraldine base to pernigraniline base.

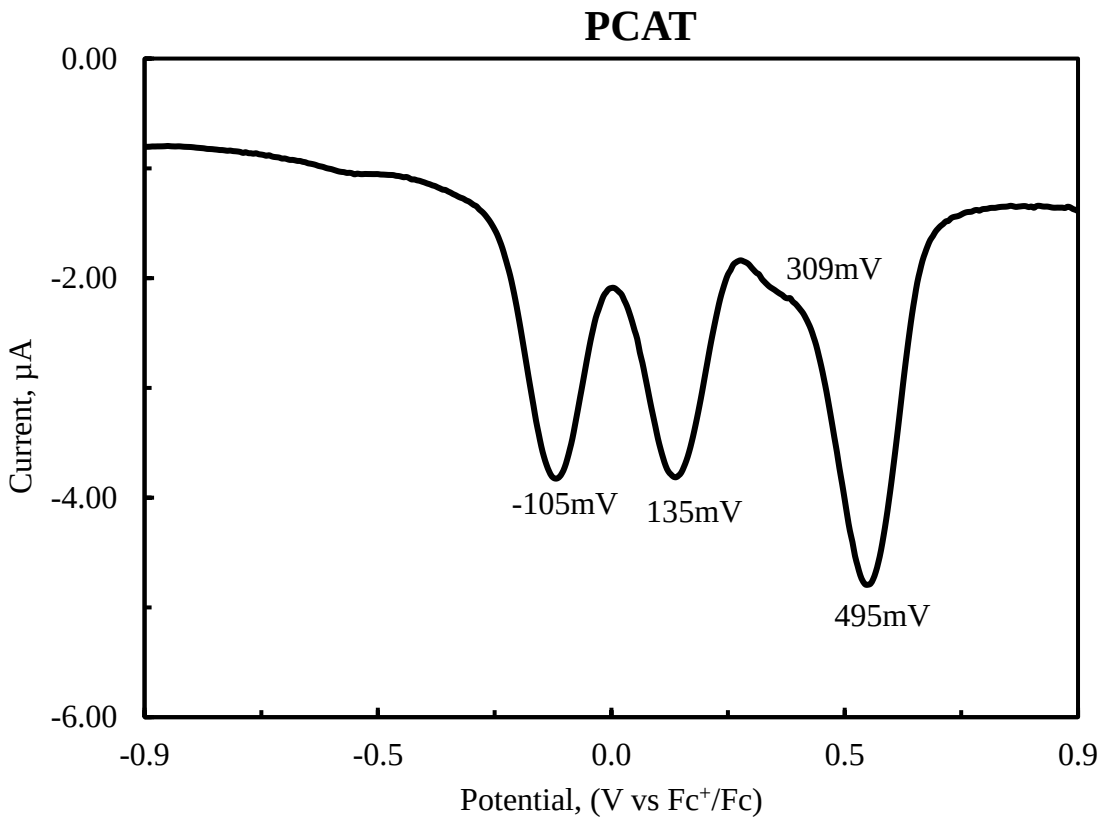

Figure 61: Differential pulse voltammogram reduction scan of PCAT in acetonitrile

The reduction scan of PCAT shows four reduction peaks at 495 mV, 420 mV, 220 mV and -9 mV. The oxidation reduction peaks show a 100 mV peak difference which is due to the E_{pulse} of 100 mV. The voltammogram shows that as the reducing voltage is applied the PCAT in its pernigraniline base, it gets reduced to the leucoemeraldine base. The four peaks can be associated with four one electron processes during PCAT reduction.

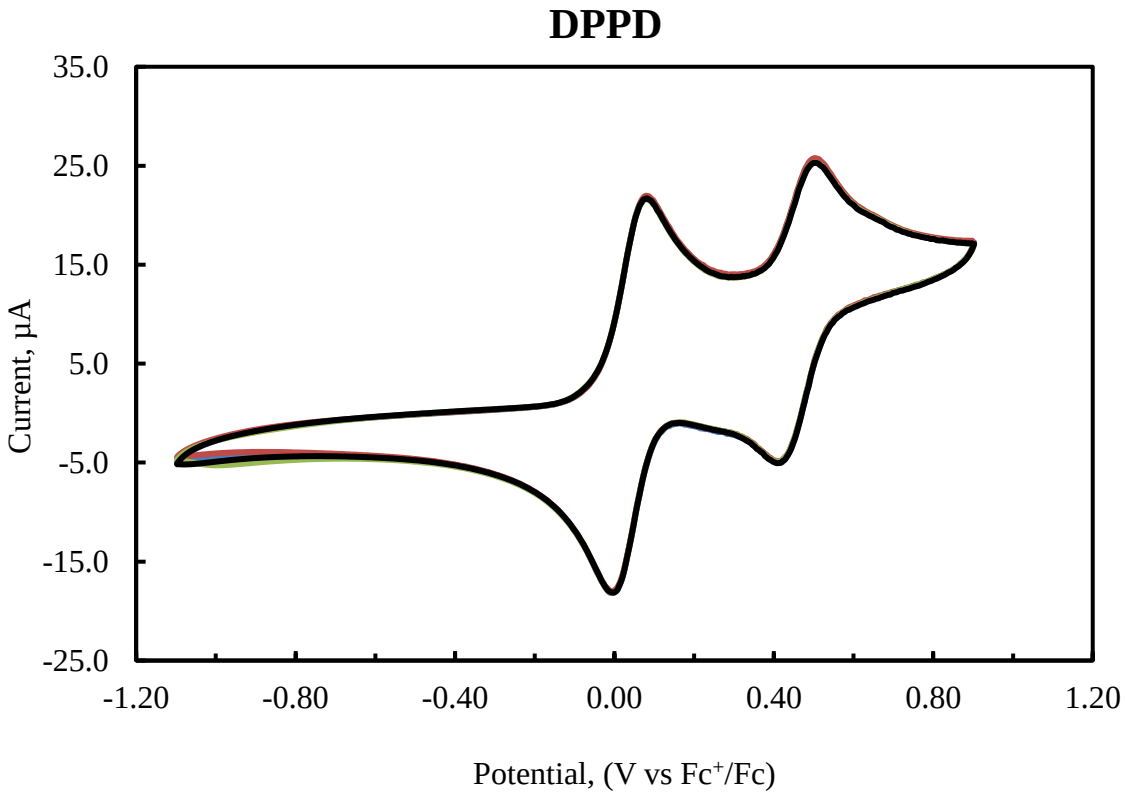

Figure 62: Cyclic voltammogram of DPPD in acetonitrile

The reversible oxidation and reduction of DPPD is a two-electron process and the cyclic voltammogram shows two reversible peaks. The peaks can be associated with the DPPD being reversibly oxidized from reduced state amine to oxidized state imine. The proposed mechanism of the DPPD redox process is given in Figure 63. It shows that reduced DPPD first converts into the intermediate semiquinoid form which is then converted into the imine base. Each process is a single electron process thus we can see two individual peaks for DPPD.

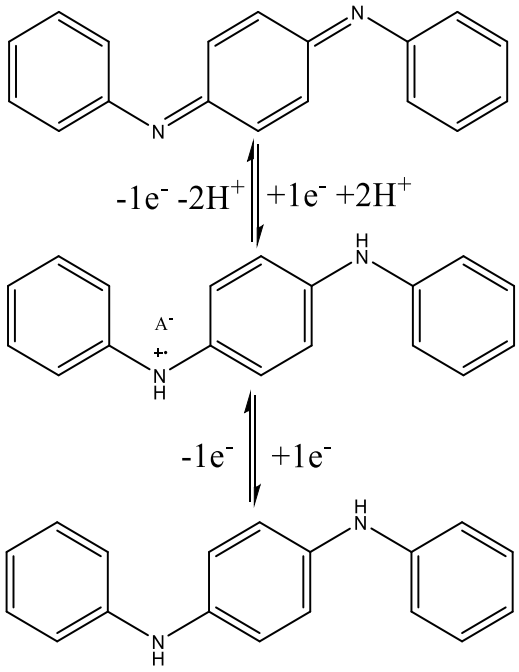

Figure 63: DPPD redox process mechanism

The oxidation scan of DPPD shows two oxidation peaks at 0 mV and 415 mV. The peak difference in Figure 64 suggests a highly stable semiquinoid intermediate and the full oxidation occurs at a higher potential similar to PCAT oxidation.

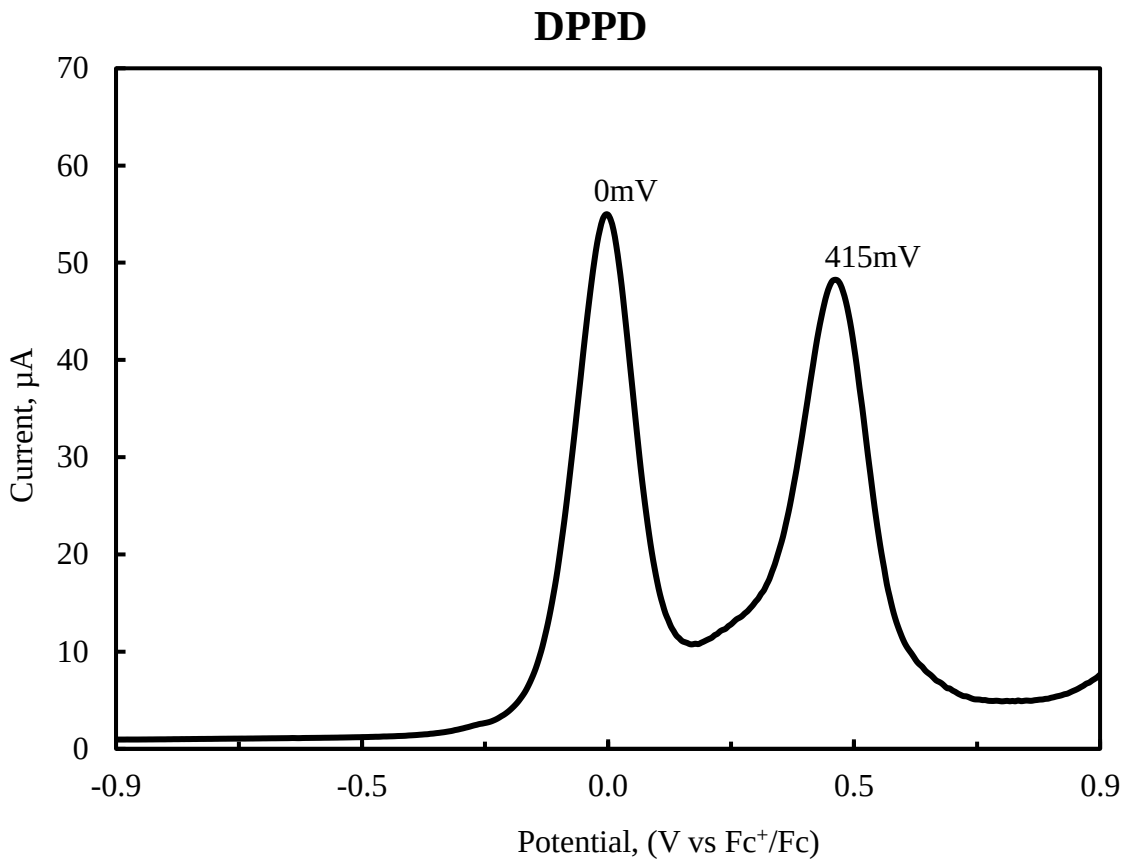

Figure 64: Differential pulse voltammogram oxidation scan of DPPD in acetonitrile

The DPPD reduction scan shows two reduction peaks at 85 mV and 510 mV. The DPV reduction scan is shown in Figure 65.

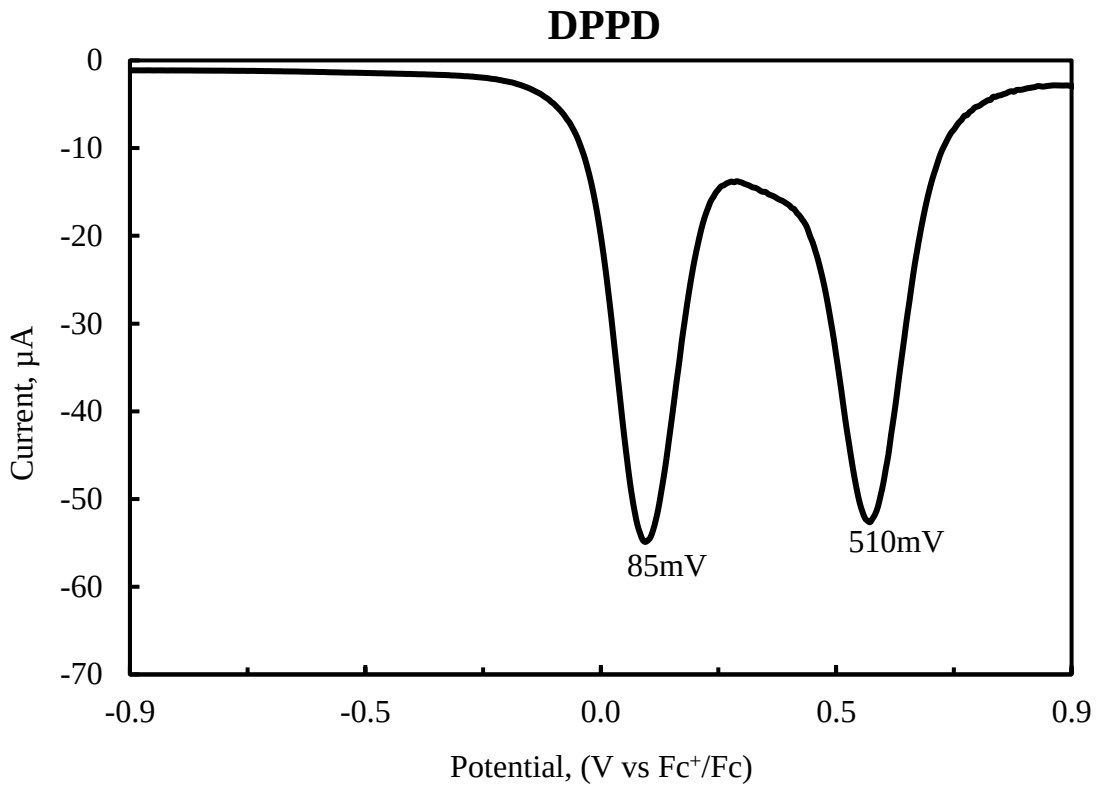

Figure 65: Differential pulse voltammogram reduction scan of DPPD in acetonitrile

The SDPPD molecule is similar to DPPD, but with two benzene rings in the middle. Adding one extra benzene ring should decrease the HOMO-LUMO gap of the molecule and it was expected to be easier to oxidize. Even though the full oxidation potential of SDPPD is lower than that of DPPD, the first redox couple of SDPPD is higher than DPPD. This might be due to the more stable structure of a conjugated molecule which increases the potential of the first redox couple. For SDPPD two reversible oxidation-reduction peaks are seen around 0.3V and a broad peak is seen at -0.6V which diminishes in the differential pulse voltammogram. The reduction peak at -0.6V might come from the dissolved oxygen. The proposed redox mechanism of SDPPD is given in Figure 67.

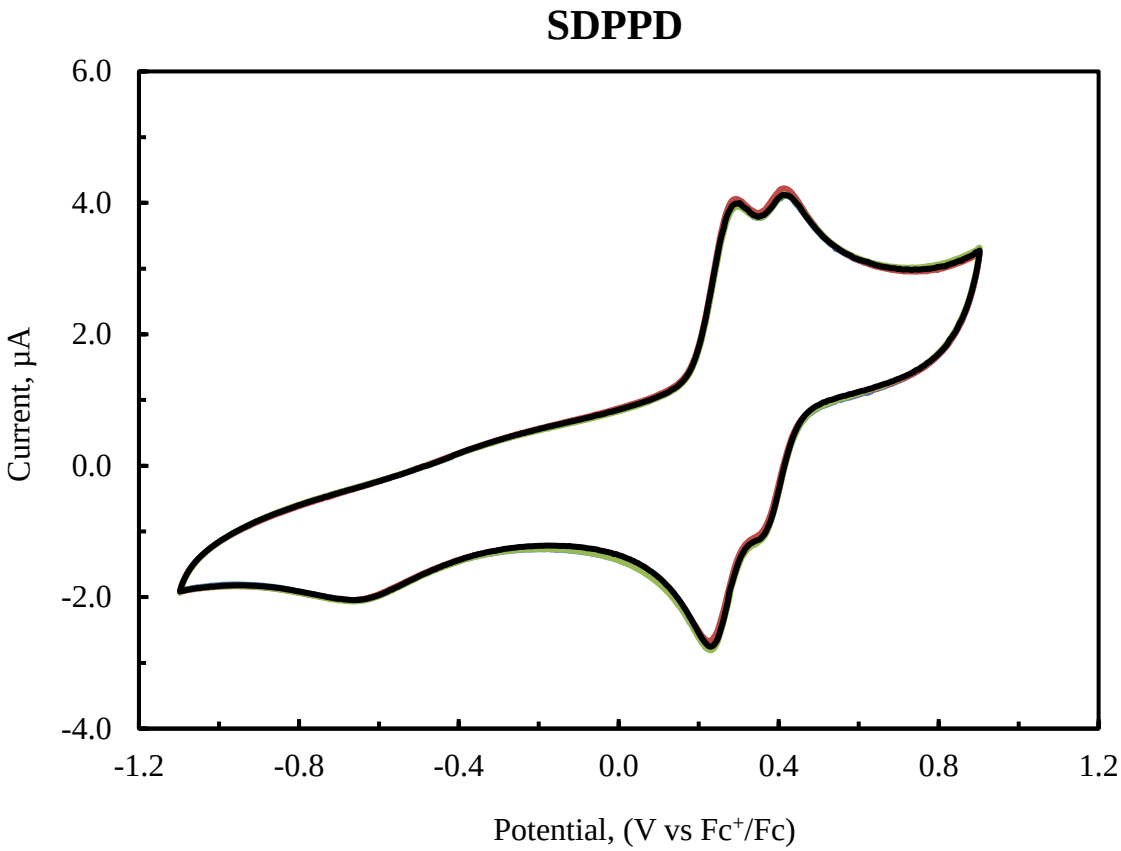

Figure 66: Cyclic voltammogram of SDPPD in acetonitrile

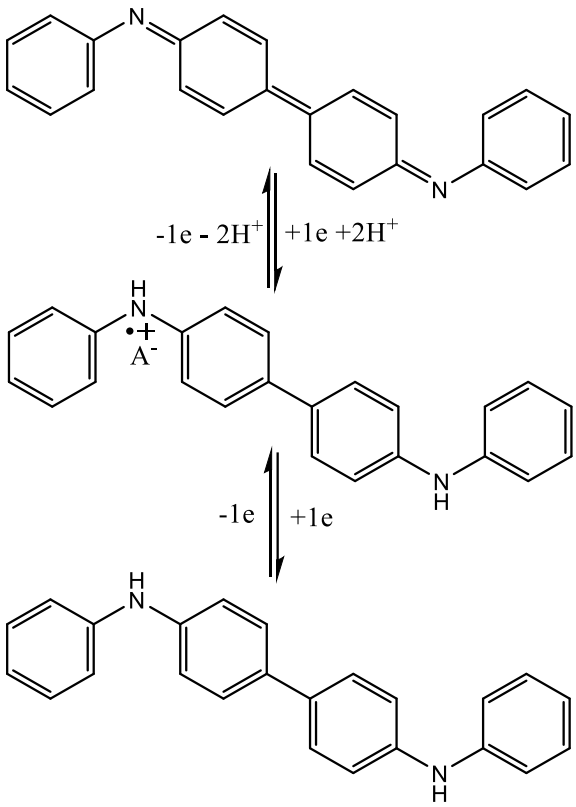

Figure 67: SDPPD redox process mechanism

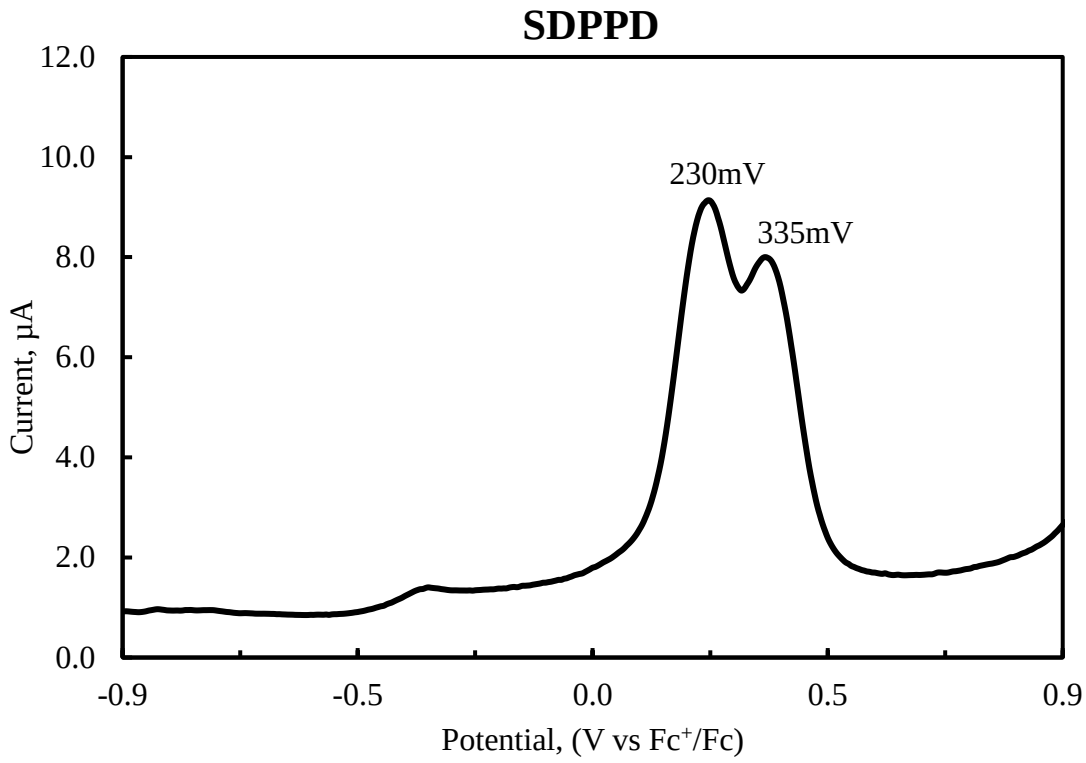

Figure 68: Differential pulse voltammogram oxidation scan of SDPPD in acetonitrile

From the differential pulse voltammogram of SDPPD, two oxidation peaks are seen at 230mV and 335mV. The two peaks are associated with the two-electron process oxidation of SDPPD.

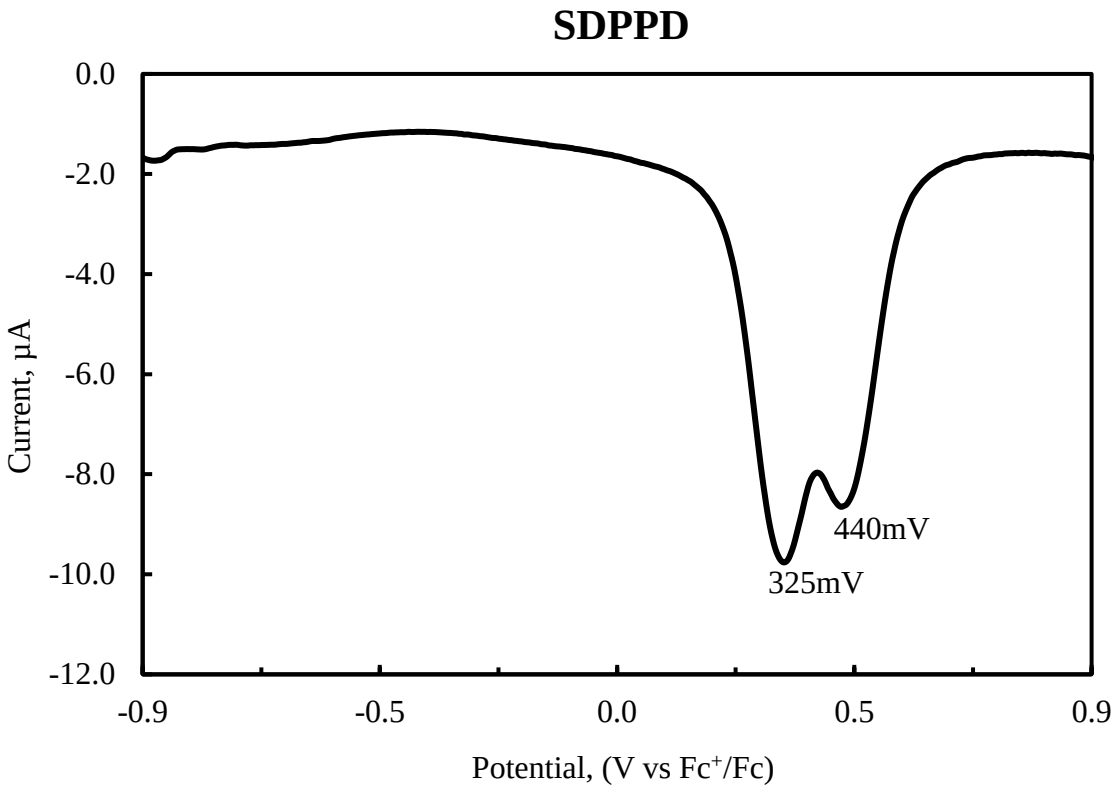

Figure 69: Differential pulse voltammogram reduction scan of SDPPD in acetonitrile

The SDPPD reduction scan voltammogram shows two peaks at 440mV and 325mV. The two peaks represent the two electron process reduction of SDPPD from its oxidized state to its reduced state.

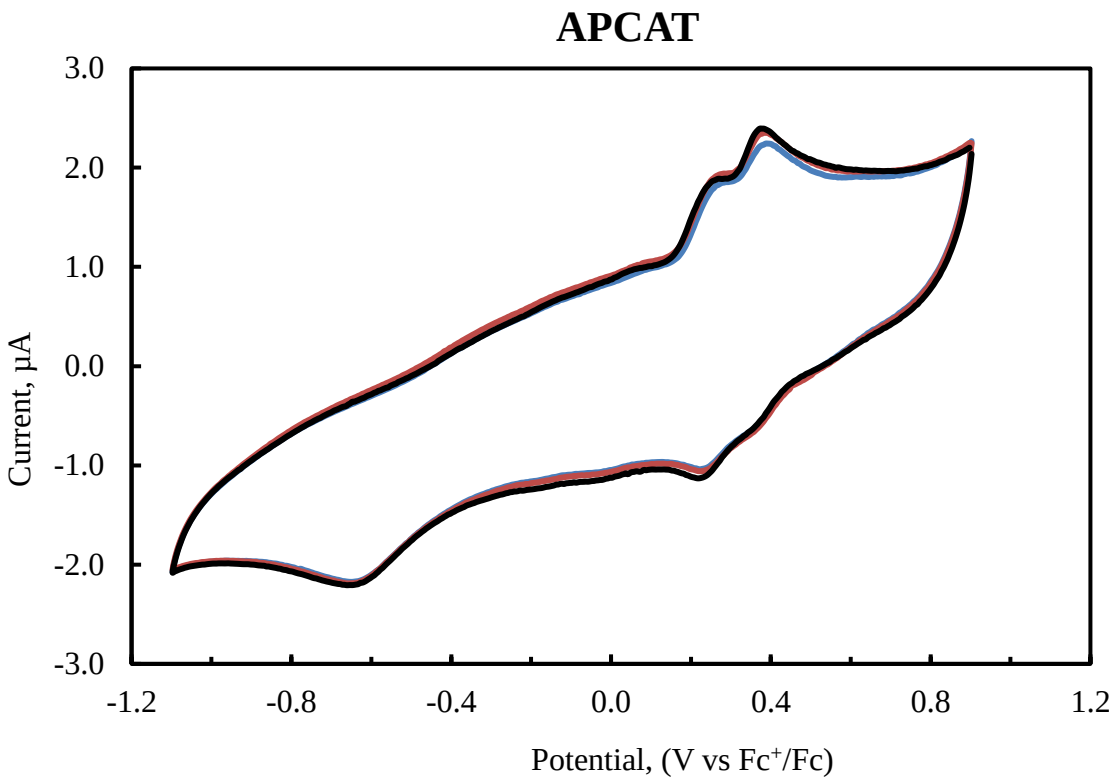

Figure 70: Cyclic voltammetry of APCAT in acetonitrile

The APCAT cyclic voltammogram is shown in Figure 70. The APCAT CV data alone doesn't give the complete information about the redox properties of the molecule. Taking into consideration DPV data, we can get a more complete picture of the redox properties of APCAT. The APCAT molecule shows similar redox properties to PCAT. Its electron transfer process is expected to be similar to PCAT because of their same structural configuration. From the CV data, we can clearly see that APCAT shows two redox couple at 0.3 V and one more broad peak at around -0.6 V. The voltammetry resolution is not very good due to the starting compound being already half oxidized and there might be some

other impurities present. Overall the DPV gives us better information to understand the redox properties of APCAT.

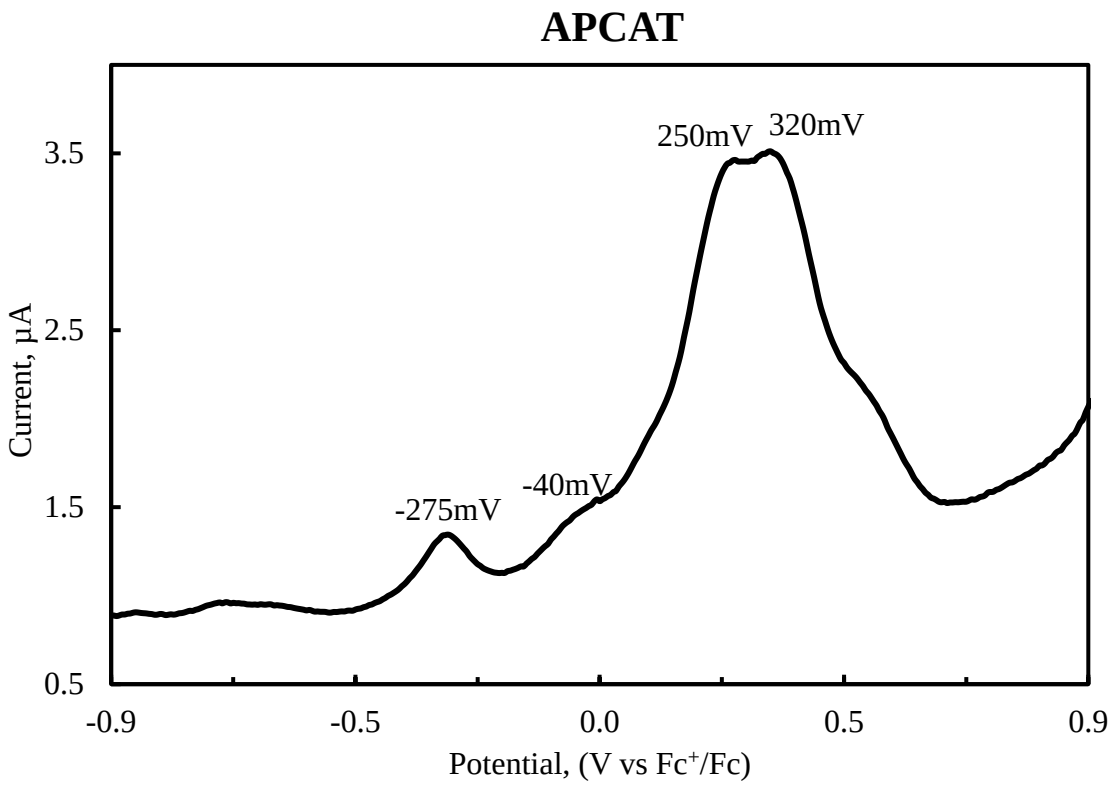

Figure 71: Differential pulse voltammogram oxidation scan of APCAT in acetonitrile

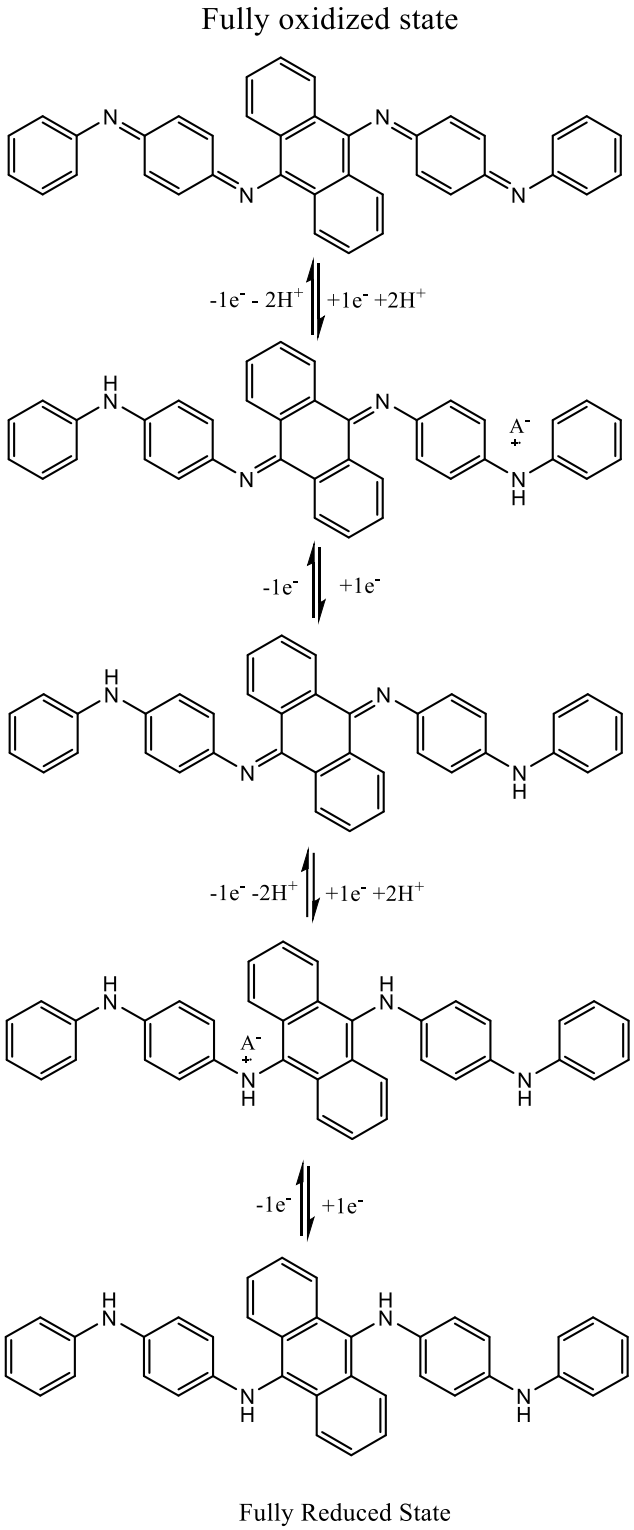

Figure 72: APCAT redox process mechanism

The DPV oxidation scan of APCAT shows four oxidation peaks at -575 mV, -215 mV, 335 mV, and 435 mV. Four peaks can be associated with the four-electron process oxidation from leucoemeraldine to the pernigraniline base. The first two oxidation peaks are much smaller compared to the second pair of oxidation peaks. We started from the half oxidized molecule which is emeraldine base, so the abundance and peak height are expected to be higher for a molecule being oxidized from the emeraldine to the pernigraniline state.

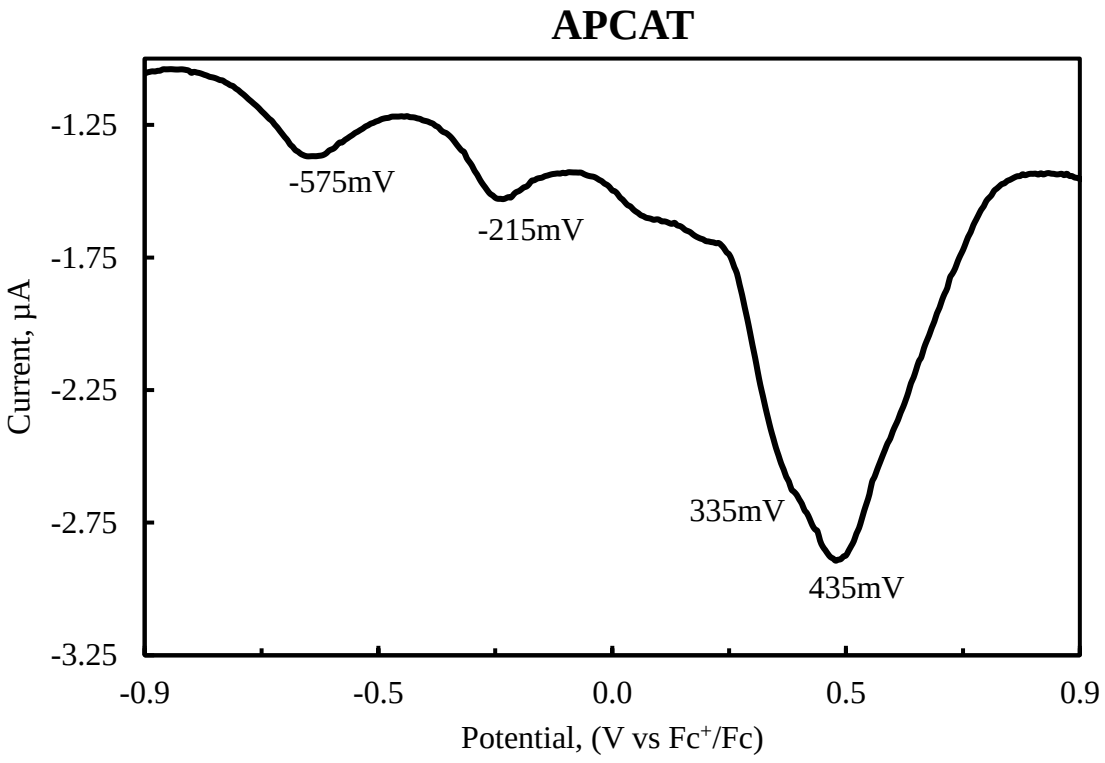

Figure 73: Differential pulse voltammogram reduction scan of APCAT in acetonitrile

The APCAT DPV reduction scan voltammogram shows four reduction peaks at 530 mV, 440 mV, -150 mV and -480 mV. The voltammogram represents the molecule being

reduced from the pernigraniline base to the emeraldine base and then subsequently getting reduced to the leucoemeraldine base.

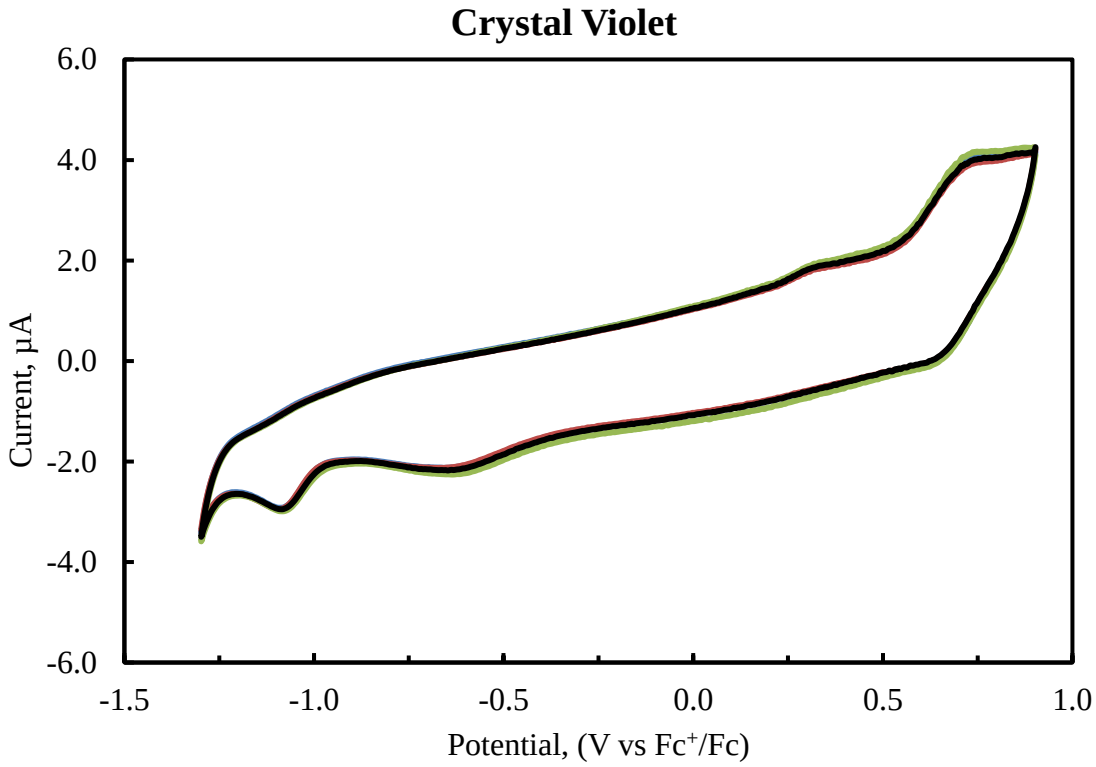

Figure 74: Cyclic voltammogram of Crystal Violet in acetonitrile

The redox properties of crystal violet are somewhat different from the aniline oligomers due to the structural differences. Structurally, aniline oligomers are long conjugated molecule while crystal violet is a short triaryl methane molecule. The CV data shows that crystal violet has one reversible oxidation-reduction and one irreversible reduction. The reversible redox process is at around 0.7V which makes crystal violet harder to oxidize in comparison to the selected aniline oligomers.

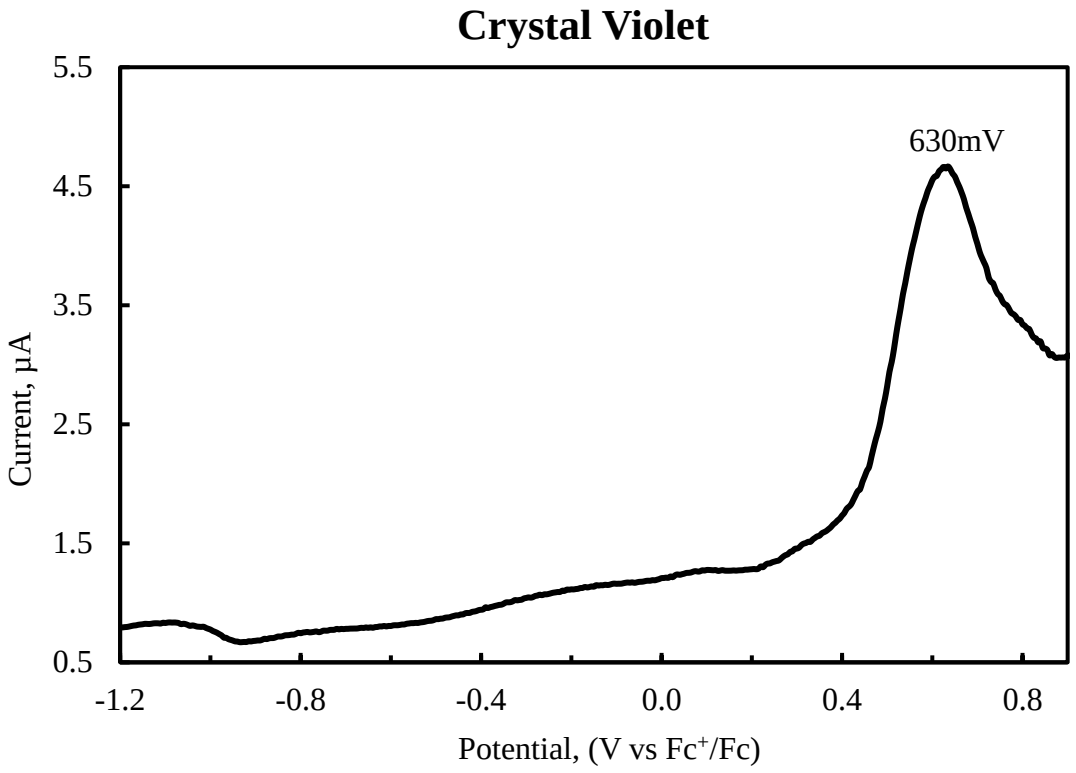

Figure 75: Differential pulse voltammogram oxidation scan of Crystal Violet in acetonitrile

Crystal Violet has one oxidation peak at 630 mV. The DPV scanning window was selected from -1.2V to +1V and all the parameters were kept same as described experimental procedure.

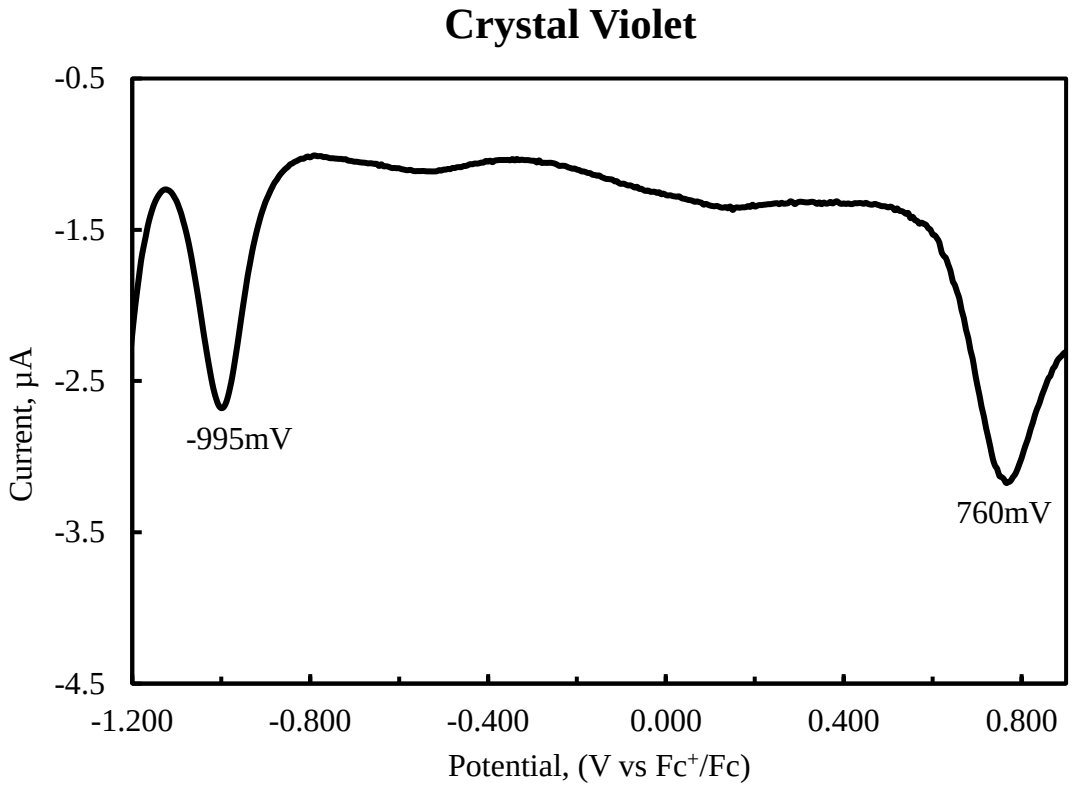

Figure 76: Differential pulse voltammogram oxidation scan of PCAT in acetonitrile

Two reduction peaks are seen in the reduction scan of crystal violet in DPV, one of which is a reversible reduction at 865mV and another is an irreversible reduction at -900 mV. This is maybe due to the leucoemeraldine form being further reduced to a very reactive anion at higher reduction potential and thus we see an irreversible reduction peak. The mechanism for the reversible peak is shown below in Figure 77 which shows a one electron process.

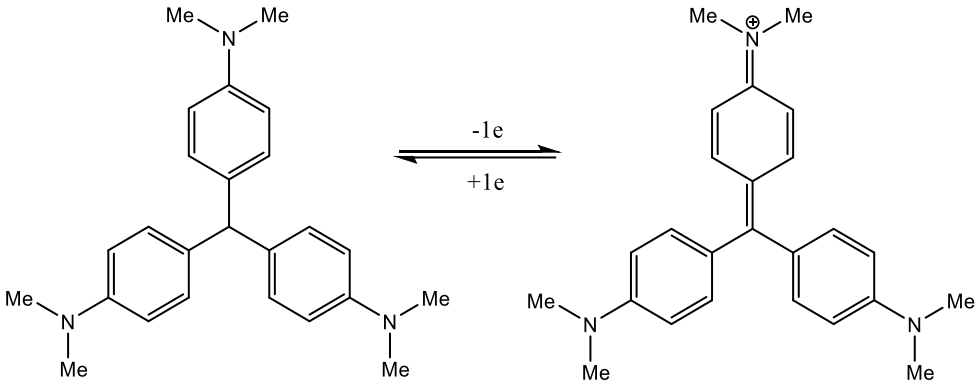

Figure 77: Crystal Violet redox process mechanism

5.3.3. Ranking of Molecule by Ease of Oxidation and Reduction

Table 2: Differential pulse voltammetry peaks for different redox active molecule.

	Oxidation Potential ($E_{1/2}$)				Reduction Potential ($E_{1/2}$)			
PCAT	-125	70	290	455	445	260	85	-155
APCAT	-225	10	300	370	385	285	-245	-625
DPPD	50	465			460	35		
SDPPD	280	385			390	275		
C. Violet	680				710			

Considering the DPV peaks for oxidation and reduction we can now rank molecules by the ease of oxidation and reduction. The oxidation reduction potential is calculated from the peak potential. For the five targeted molecules, the ease of oxidation and reduction ranking will be

Ease of oxidation ranking

1. Reduced APCAT
2. Reduced PCAT
3. DPPD
4. SDPPD
5. Half oxidized PCAT
6. Half oxidized APCAT
7. Crystal Violet

Ease of reduction ranking

1. Crystal Violet
2. DPPD
3. Oxidized PCAT
4. Oxidized APCAT
5. SDPPD
6. Half oxidized PCAT
7. Half oxidized APCAT

5.4. SENSOR PERFORMANCE

5.4.1. SENSOR CALIBRATION AGAINST FREE CHLORINE AND POTASSIUM PERMANGANATE

Sensing response for two different disinfectants is shown in Figure 78. The change in sensor film conductivity was plotted against different disinfectant concentrations. The sensing response was plotted relative to the 0 ppm current baseline.

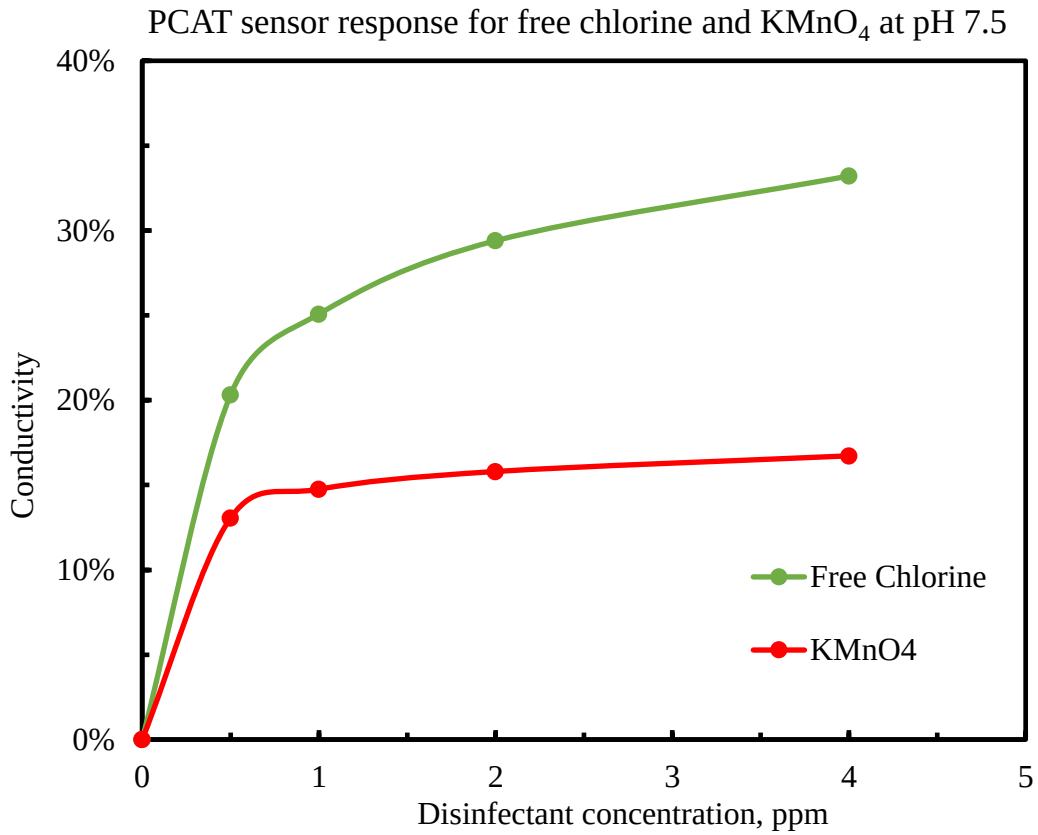

Figure 78: PCAT sensing response for two different disinfectants

From the figure, we can find that free chlorine, in general, gives a higher sensor response than $KMnO_4$ for different concentrations. After a certain concentration, the sensor

gets saturated and the conductivity doesn't increase much with the increase of concentration.

The sensor response characteristics can be explained if we consider that we are measuring the oxidation reduction potential of an analyte. The oxidation reduction potential of an oxidant at an electrode can be calculated from the Nernst equation.

$$E_{mv} = E_o + 2.3026\frac{RT}{nF}\log\frac{[\text{Oxidizer}]}{[\text{Reducer}]}$$

For the hypochlorous acid oxidation, the Nernst equation can be written as following

$$HOCl + H^+ + 2e \longrightarrow Cl^- + H_2O$$

$$E_{mv} = E_o + 29.58\log\frac{[HOCl][H^+]}{[Cl^-]}$$

$$E_{mv} = E_o + 29.58\log[HOCl] - 29.58pH - 29.58\log[Cl^-]$$

For any oxidizing reaction, the equation can be written as following

$$E_{mv} = \text{Standard reduction potential} + X\log(\text{Oxidant Concentration}) - YpH - Z \qquad (1)$$

$$X,Y,Z = \text{constants}$$

For any specific oxidizing agent at constant pH, the oxidation reduction potential is in relation with log concentration of the oxidizing agent. Our sensor is previously reported to have a sensor response characteristic which is in log relation with disinfectant concentration.[1]

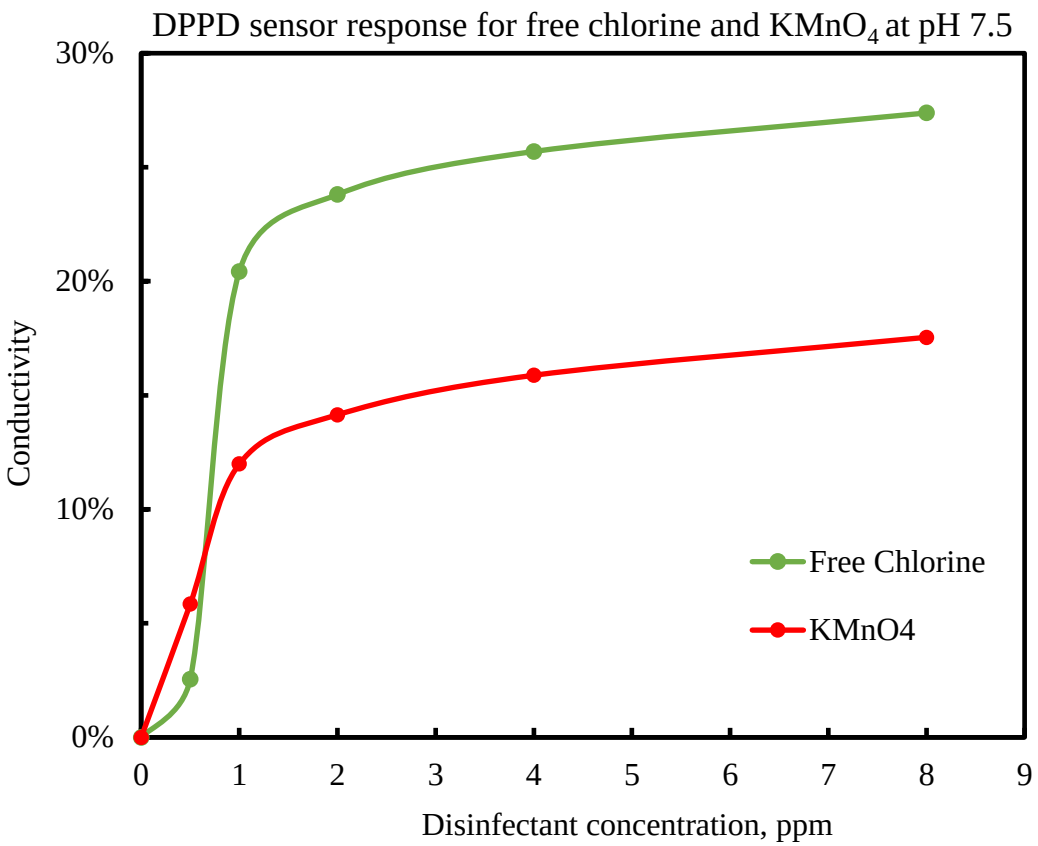

Figure 79: DPPD sensing response for two different disinfectants

The DPPD sensor gives a similar sensing response plot as PCAT for two different disinfectants. There is an overall decrease in sensing response in comparison to the PCAT sensor. 0.5 ppm free chlorine gives lower sensor response than 0.5ppm $KMnO_4$. This might be due to the lower stability of free chlorine at lower concentrations. Free chlorine stability is discussed at the end of this chapter which shows that free chlorine is very unstable at lower concentrations. The instability of free chlorine is due to the reaction of free chlorine with the syringe. We used one-time syringes for different analytes and sometimes we didn't see any free chlorine degradation.

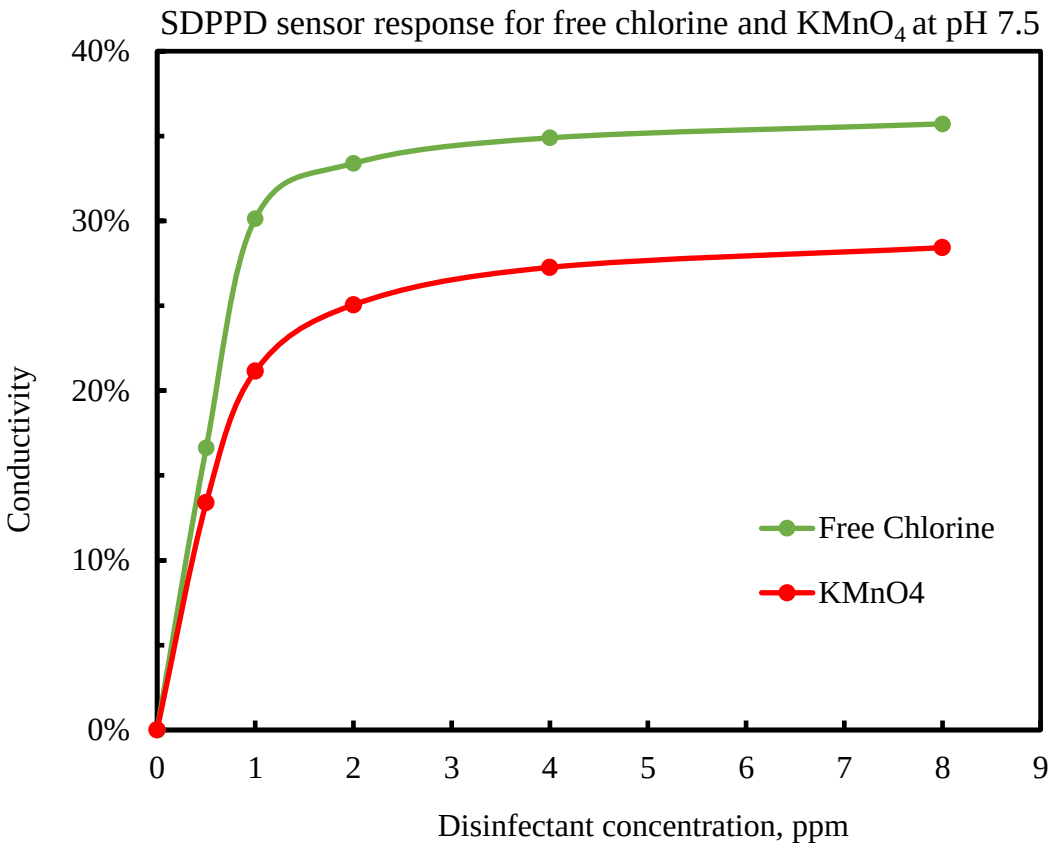

Figure 80: SDPPD sensing response for two different disinfectants

SDPPD gives a similar sensing response as PCAT for two different disinfectants. There is an overall increase in sensor response compared to both PCAT and DPPD. This might be due to a solvent effect. In chapter 5 we discussed the surface wetting effect of methanol as a solvent. SDPPD is insoluble in methanol and acetonitrile was used as the substitute for methanol. Acetonitrile could facilitate better surface wetting than methanol which could lead to higher sensing response. Also, there could be an effect of solvent distribution coefficient on molecule deposition during sensor programming which could lead to higher sensing response. Another possible reason for higher sensing response might

be the ease of complete oxidation of SDPPD compared to complete oxidation of PCAT and DPPD.

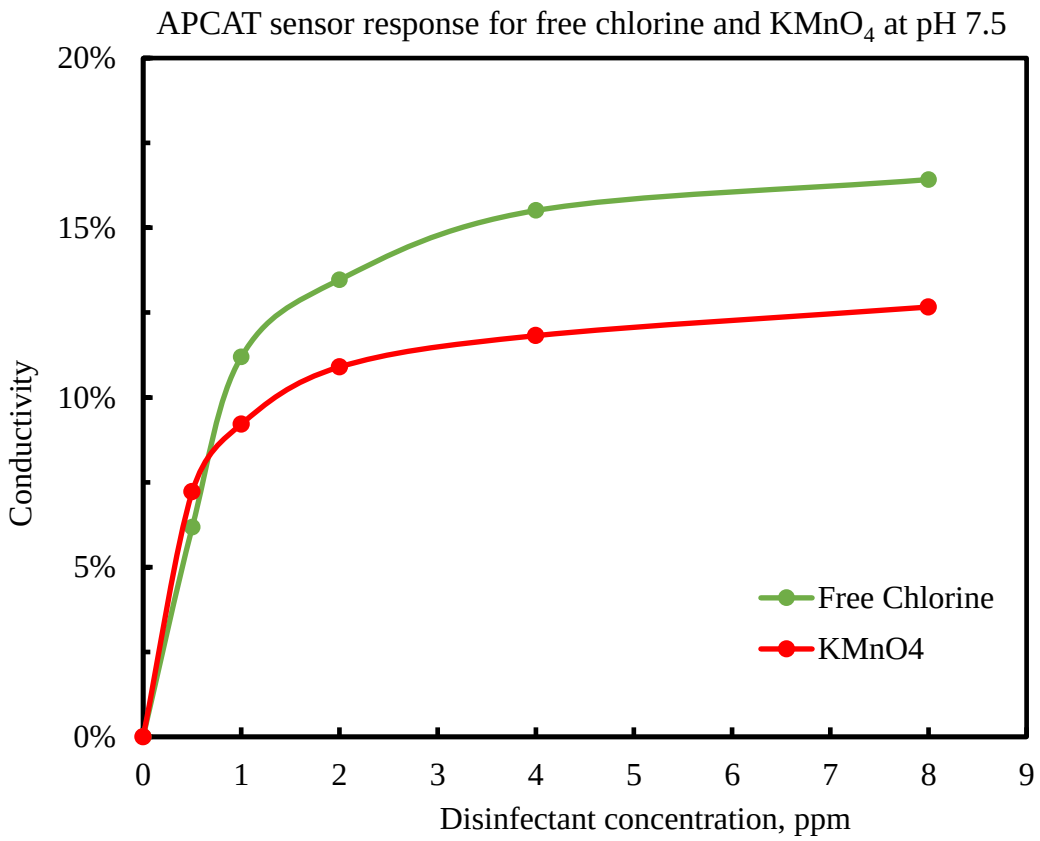

Figure 81: APCAT sensing response for two different disinfectants

The APCAT sensing characteristic for two different disinfectants is shown in Figure 81. APCAT has an overall lower sensing response in comparison to the other redox active molecules. Higher sensing response for 0.5 ppm $KMnO_4$ compared to 0.5 ppm free chlorine might be due to the faster degradation of free chlorine analyte at low concentration.

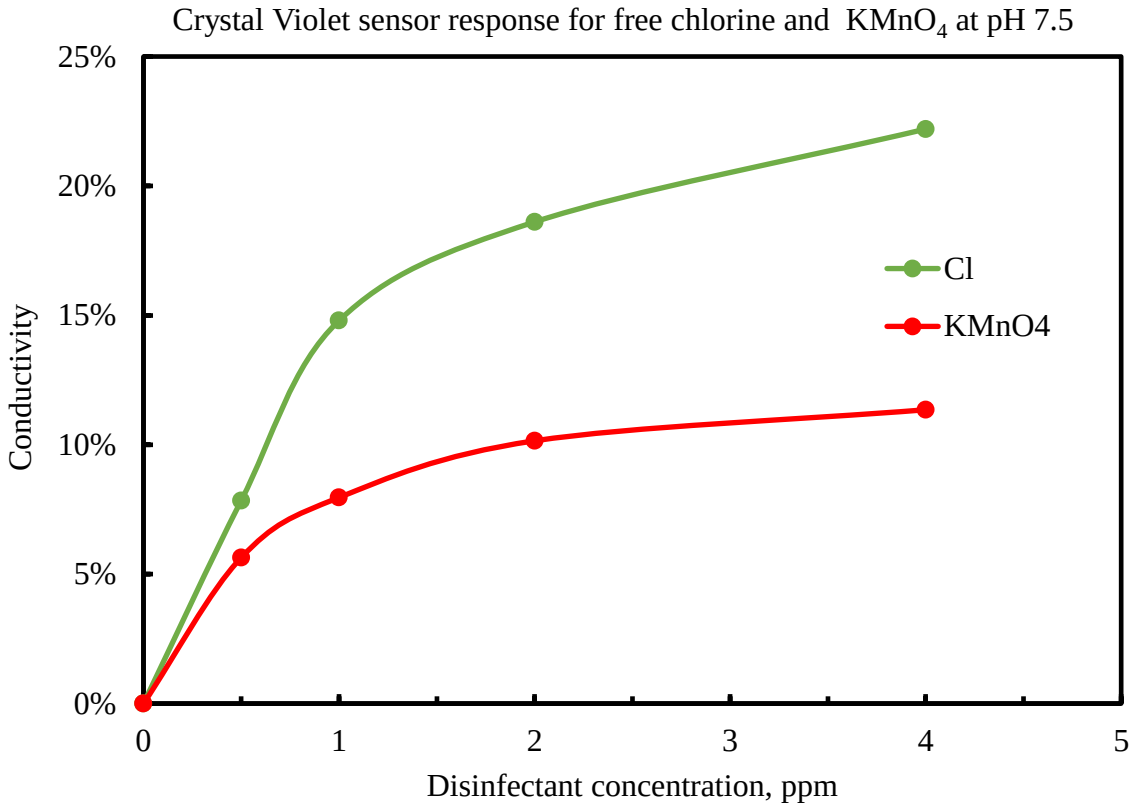

Figure 82: Crystal violet sensing response for two different disinfectants

A similar sensor response trend is seen for crystal violet for the two different disinfectants. Crystal violet gives a lower sensor response in comparison to the PCAT, DPPD and SDPPD sensors.

Comparing all the redox active molecules we can see a higher sensor response trend with ease of oxidation ranking. APCAT is an exception which shows a lower sensing response than crystal violet. APCAT is a large molecule with an anthracene ring in the middle and likely has more effective pi-pi interactions with the nanotubes, possibly making it a more effective dopant. In comparison to our redox active aniline compounds, we can

clearly see the relation between sensing response and redox potential. This gives a hope that molecules with higher oxidation potential could be used to differentiate between stronger and weaker oxidizing agents

5.4.2. IMPACT OF pH AND ORP ON SENSING RESPONSE

Quantifying the sensor response with relation to pH change was one of the goals of this study. PCAT sensor response at different pH for 1ppm free chlorine and 1ppm $KMnO_4$ is shown in Figure 83. The sensor response is plotted as a change in conductance of sensor film versus pH. The response is calculated relative to the baseline current at a pH 10.43 without any oxidant, which therefore represents 0 percent change in the sensing plot. The sensor was tested for a pH range of 5 to 10.75. The drinking water pH range is usually in between 6 to 8.5.

From the sensor response plot for disinfectants it is clear that the pH has a significant effect on the sensing response. 1 ppm free chlorine gives different sensing responses at different pH values. For example, at pH 10.5 the sensor gives around 10% response for 1 ppm free chlorine whereas at pH 5 the sensor gives 42% sensing response. There is an almost 4 times sensing response increase for 5-unit pH change. The $KMnO_4$ also shows a similar sensing response trend but with a different slope for changes in pH. At pH 10.5 the sensor gives around 15% response for 1 ppm $KMnO_4$ whereas at pH 5 the sensor gives 30% sensing response. The sensing response doubles for around 5-unit pH change for $KMnO_4$.

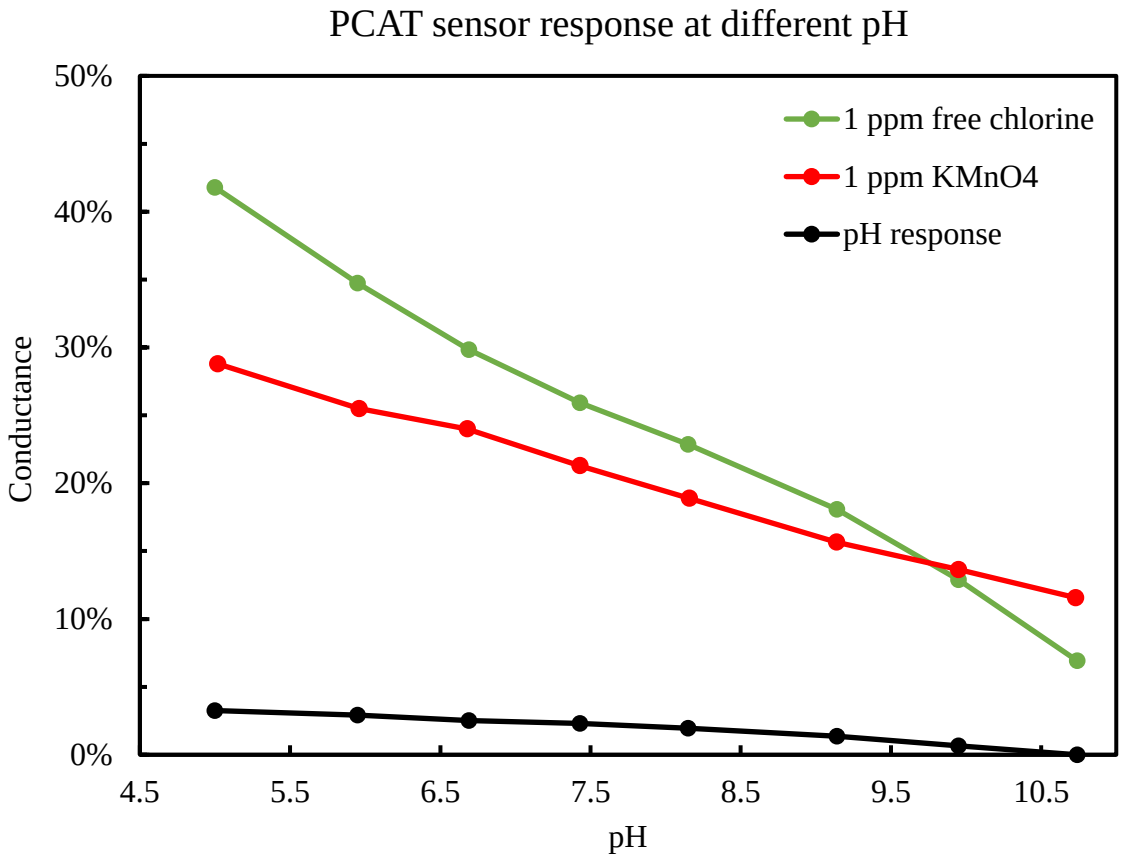

Figure 83: PCAT sensor response for 1 ppm free chlorine and 1 ppm KMnO4 at different pH

The change in sensor response with different pH can be explained by the Nernst equation for an oxidizing agent. At constant oxidant concentration, a change in pH will change the ORP of the solution. At low pH, the oxidation potential will be higher, and at high pH, oxidation potential will be lower.

$$E_{mv} = \text{Standard reduciton potential} + X \log(\text{Oxidant Concentration}) - YpH - Z$$

$$X,Y,Z = \text{constants}$$

Our sensor shows a similar trend to the Nernst equation. We see lower sensing response at higher pH and higher sensing response at lower pH. This sensing response is consistent with the hypothesis that we are measuring oxidation reduction potential rather than just oxidant concentration.

Both the disinfectants have different sensing response slopes which is consistent with different oxidation reaction coefficients (see Table 1). This could be an advantage for differentiating between two different disinfectants. If a certain range of pH change for a constant disinfectant concentration is measured the conductivity slope could potentially give an identification of that disinfectant. The characteristic sensor response curve for two different disinfectants crosses at pH 9.8. The crossing point is also seen for DPPD, SDPPD and crystal violet at different pH value. The crossing point seems to vary for different molecules which is related to the degree of oxidation of each molecule.

PCAT is an aniline compound which can be pH-responsive and the pH sensing response was also shown in Figure 83. The pH sensing response is much smaller compared to the free chlorine and permanganate response. In comparison, the free chlorine response is ten times higher than the pH response.

DPPD also behaves in a similar trend as PCAT with a change in pH which is shown in Figure 84. The sensor gives a 10 percent change in conductivity for 1 ppm free chlorine at pH 9.5 and a 50 percent change in conductivity for 1 ppm free chlorine at pH 5, which is a 4-times increase in conductance for 4.5 units of pH. The sensor gives a comparable change in conductivity for permanganate at different pH values. From the trend line for 1

ppm free chlorine and 1 ppm $KMnO_4$, it is clear that the sensing response is consistent with disinfectant chemistry. Both the disinfectants cross at pH 9.0 for the DPPD molecule.

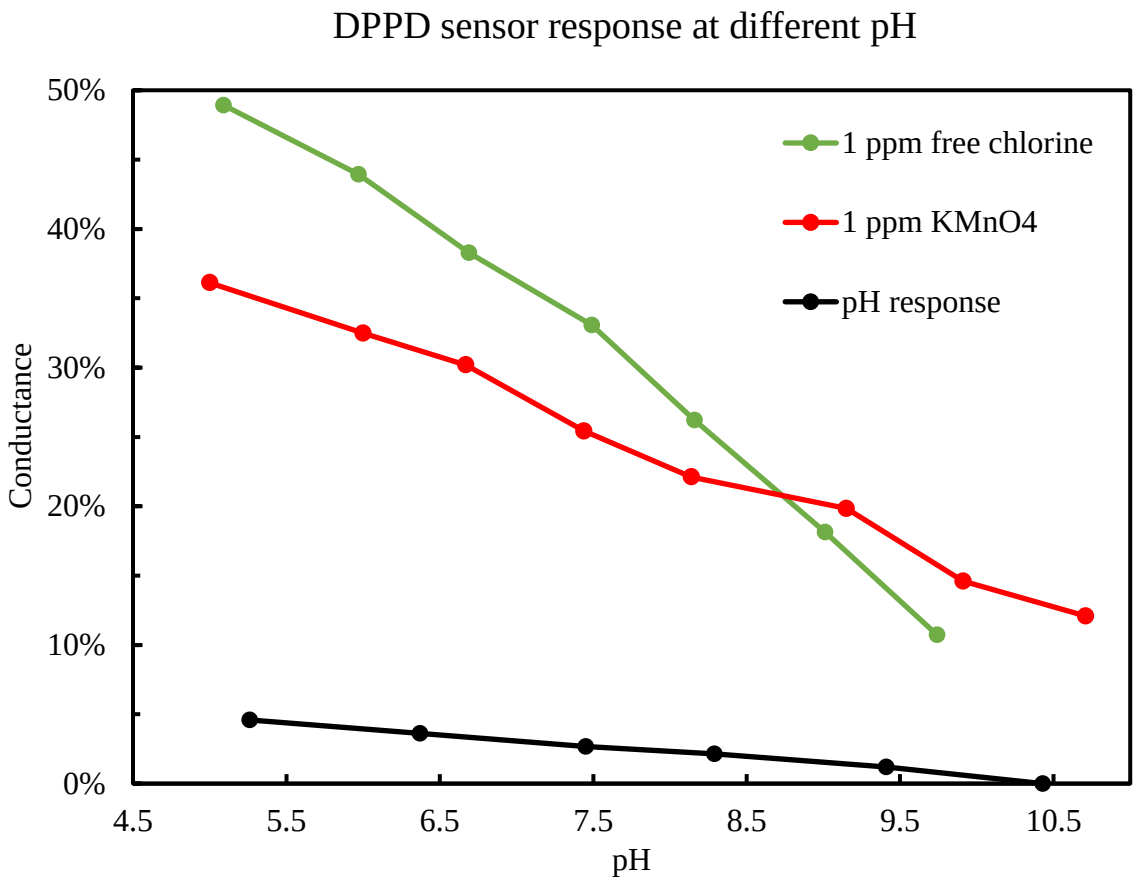

Figure 84: DPPD sensor response for 1 ppm free chlorine and 1 ppm KMnO4 at different pH.

The SDPPD sensor response for 1 ppm free chlorine and 1 ppm $KMnO_4$ is shown in Figure 85. pH sensing at 0 ppm was not done for the SDPPD molecule but we expect it to sense pH like other aniline oligomers. The sensor response trend shows that SDPPD sensing is consistent with disinfectant chemistry. The response for the two disinfectants crosses at pH 10.2.

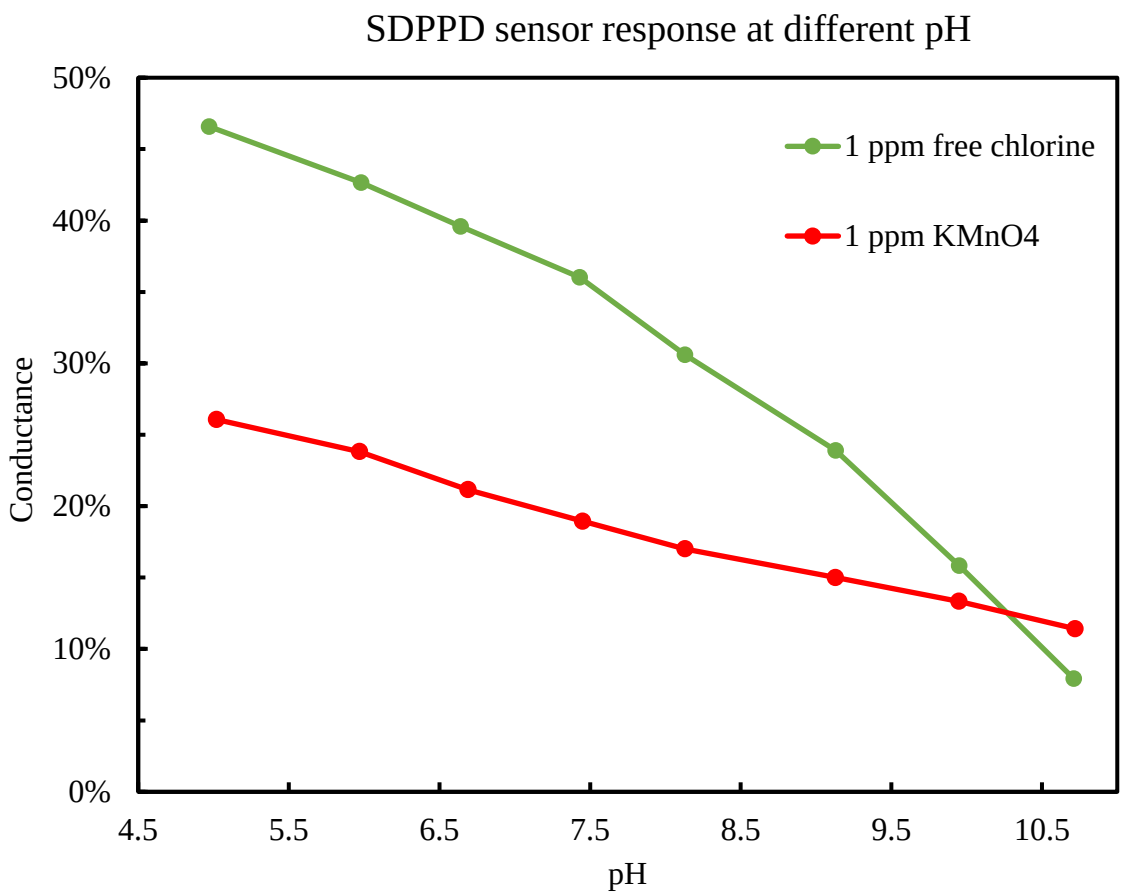

Figure 85: SDPPD sensor response for 1 ppm free chlorine and 1 ppm KMnO4 at different pH.

The APCAT sensor response with pH changes for two disinfectants is shown in Figure 86. The APCAT sensor has the overall lowest sensing response in comparison to other redox active molecules. The sensor response trend is consistent with the disinfectant chemistry. For APCAT we don't see any crossover in sensing response curves in our tested pH range but given the different slopes, we will see a crossover at higher pH.

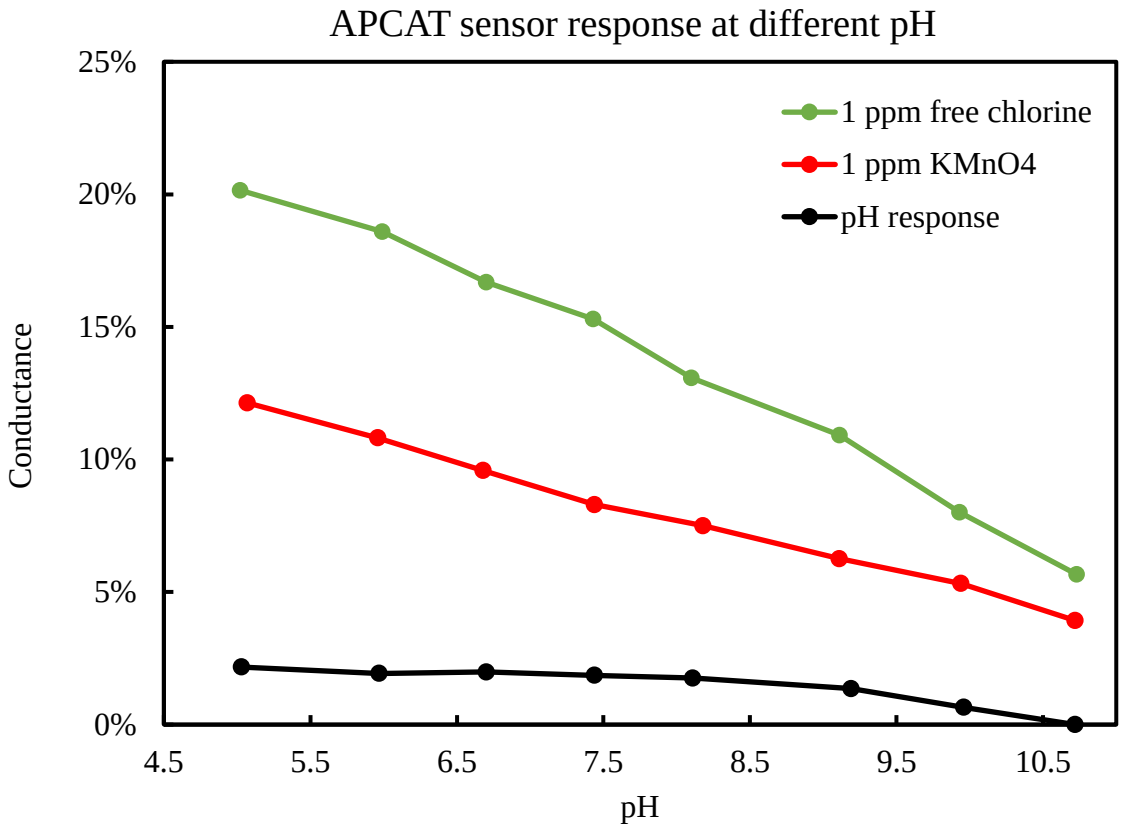

Figure 86: APCAT sensor response for 1 ppm free chlorine and 1 ppm KMnO4 at different pH

The crystal violet sensor response for two disinfectants at different pH is shown in Figure 87. Both the disinfectants show similar sensing response slopes and it will be very hard to differentiate between $KMnO_4$ and free chlorine with a crystal violet sensor. But it is clear that the sensing response behavior is consistent with the change in oxidizing power of disinfectants.

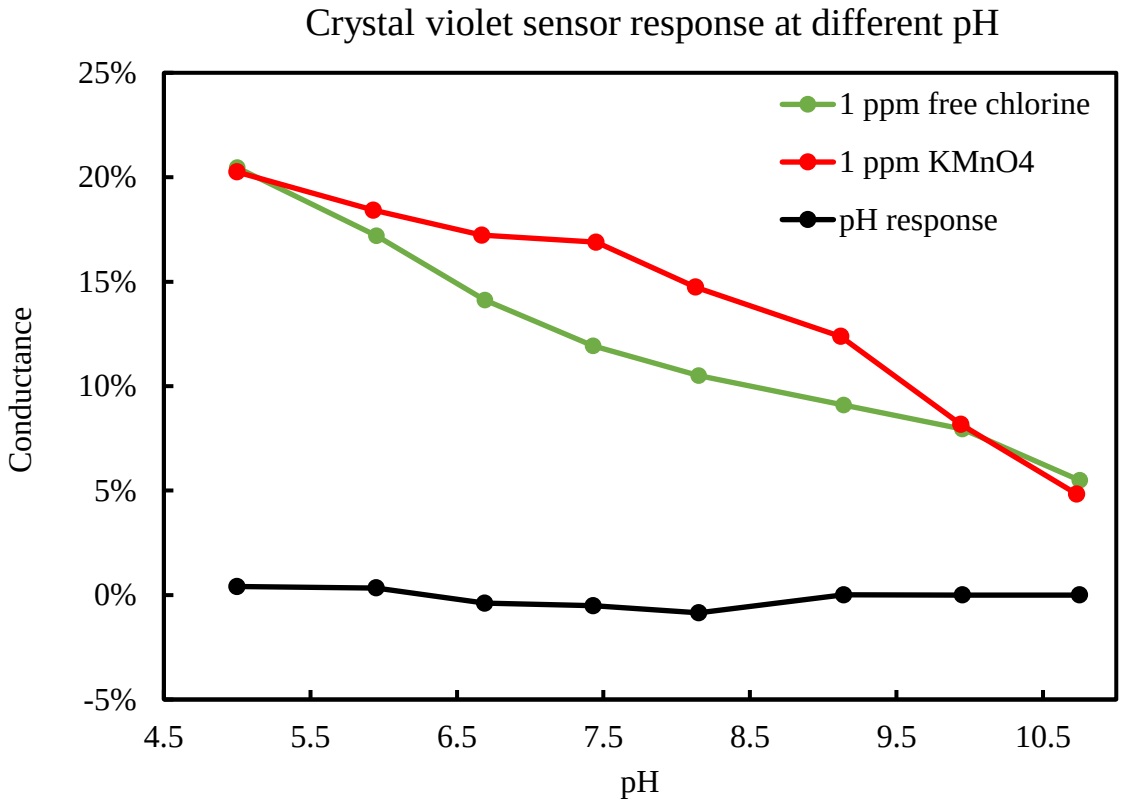

Figure 87: Crystal Violet sensor response for 1 ppm free chlorine and 1 ppm KMnO4 at different pH

Crystal violet doesn't show any response to pH in absence of an oxidant. This is because crystal violet has a pH indicating the range of -1 to 2. The experimental pH range is from 5 to 10.75 in which range crystal violet stays in its form. Therefore, there is no salt and base formation within our experimental pH range and we don't see any pH response.

5.4.3. ELECTROCHEMICAL MEASUREMENT WITHOUT REFERENCE ELECTRODE?

Both the disinfectant concentration and pH change strongly indicate that our sensor response is directly related to the oxidation reduction potential of the analyte. During the discussion about distinguishing different disinfectants, we showed that it is also possible to calculate the ORP of the analytes from our sensor response. ORP measurement is an electrochemical measurement. Electrochemical measurements are done in presence of a reference electrode and we don't have a reference electrode in our sensor setup. The important question is how it possible to perform electrochemical measurements without a reference electrode?

A chemical change can be measured in different ways. For example, a titration reaction can be done by using both the colorimetric method or the potentiometric method. In our sensing approach, we are measuring colorimetric changes instead of potentiometric change. We explained our approach of measuring colorimetric changes at carbon nanotube surfaces in chapter 1. A reference electrode free chemiresistive pH sensor has been reported based on a sensing approach similar to ours.[92]

5.4.4. EFFECT OF BUFFER

We used 0.005 M phosphate buffer for analyte preparation and the effect of the buffer was tested on the sensor. Four different buffer concentrations from 0.0025 M to 0.02 M were tested. The change in conductivity of a DPPD sensor for different buffer concentrations is

shown in Figure 88. The conductivity change is almost negligible for different concentrations.

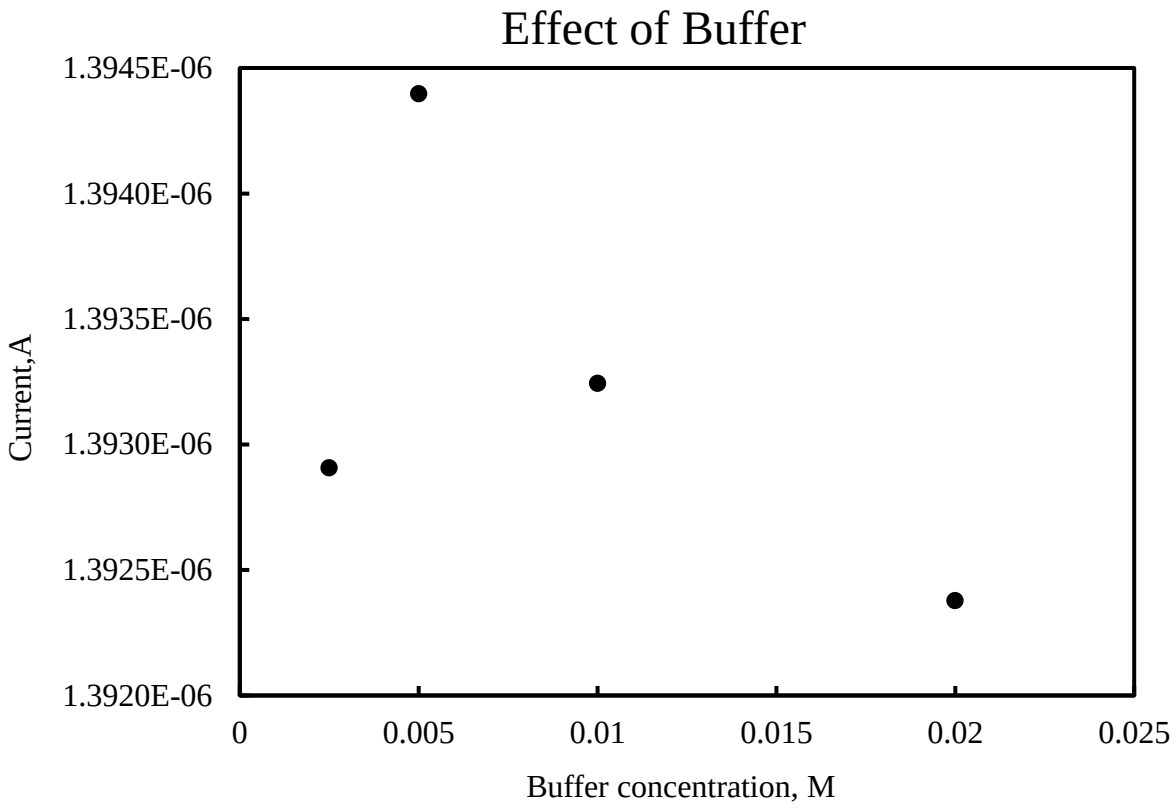

Figure 88: Current measurement for different buffer concentration.

The comparison of the sensor response for a simple pH change and a buffer concentration change is shown in Figure 89. A change in pH of 0.1 units results in about 0.1% sensor response for a pH changing from 7.42 to 7.12. On the other hand, a change in concentration of the buffer from 0.0025 M to 0.2 M gives just 0.04%. In conclusion, an 8-fold change in concentration has almost negligible consequence for the sensor response.

Therefore, the sensor is selective to pH and oxidizing agents only, not to the buffer concentration.

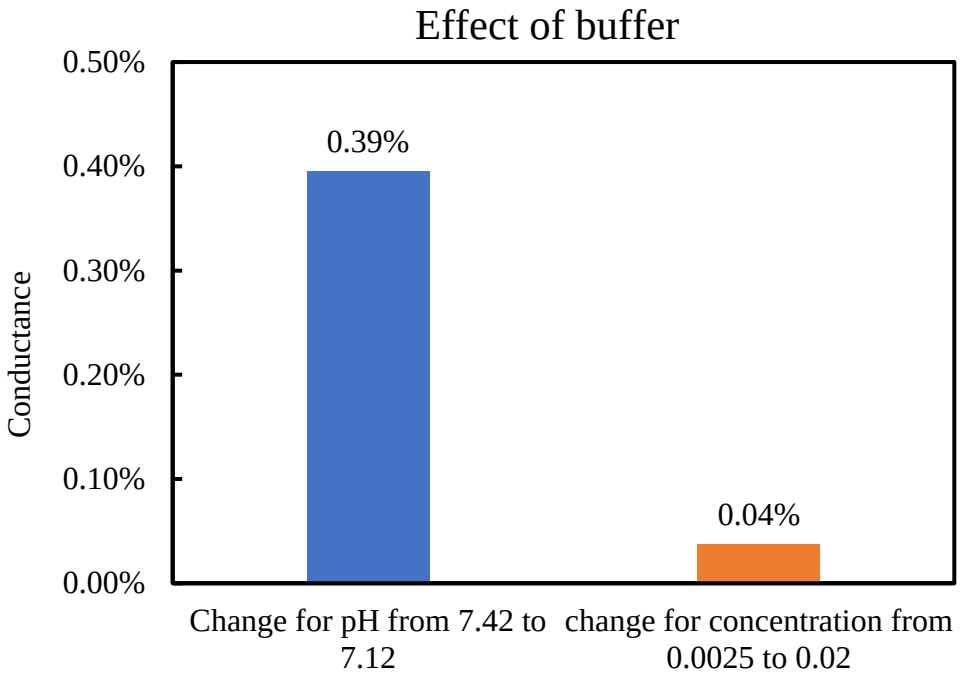

Figure 89: Comparison of sensing response for pH and buffer concentration

5.4.5. Stability of Free Chlorine:

Disinfectants are oxidizing agents and they can easily react and get depleted. So, it was necessary to verify the stability of the prepared analyte solution. The concentration of free chlorine and ORP value of the analyte were recorded before and after exposure to the sensor. The free chlorine concentrations were measured using a Hach free chlorine kit and ORP values were measured using an ExStik RE300 ORP meter.

Table 3: Stability of free chlorine and oxidation reduction potential of the analyte.

Stability test					
	Cl			ORP	
Standard	Actual	After(out from sensor and after orp measurement)	Actual	After	Rest in the syringe
0 ppm			178		
0.5 ppm	0.6	0.1	370	300	320
1 ppm	1.1	0.4	464	450	458
2 ppm	2.1	0.8	580	540	
4ppm	4.2	3.4	726	708	715

Actual values represent the measurement data of the prepared solution. After value represents the analytes that are collected after exposure to the sensor. At low concentration, the free chlorine depletion is very high even though the ORP values don't show that much of a decrease. It could due to the sequence of the experiment and a relatively small volume of analyte solution. At higher concentration, the depletion is relatively small compared to lower concentrations.

5.5. DISTINGUISHING DISINFECTANTS

5.5.1. DISTINGUISHING BETWEEN FREE CHLORINE AND POTASSIUM PERMANGANATE

From the concentration and pH change experiments, we have seen that our sensor response is related to the ORP of the analytes. We further extended our analysis to determine the relationship of our sensor response with the ORP of the analytes. Measured and literature ORP values for different analyte concentration tested are given in Table 4. Even though our ORP measurement values are smaller compared to literature values, overall, they give a relative comparison.

Table 4: Measured and literature ORP values for different analytes.[93]

Disinfectant Concertation (ppm)	Measured Free Chlorine ORP (mV)	Literature Free Chlorine ORP (mV)	Measured $KMnO_4$ ORP(mV)	Literature $KMnO_4$ ORP (mV)
0	155	420	165	500
0.5	234	780	240	700
1	318	890	335	740
2	460	920	427	760
4	568	960	466	780
8	663		495	

ORP values and sensor response for different analytes are compared in Figure 90 and Figure 91. We can clearly see that; our sensors behave differently from each other which is the result of the different redox potentials of the molecules. Also, as they are not

directly in a linear relationship with ORP there could be some deviation from the actual ORP. It will be beneficial to calculate the deviation for further analysis.

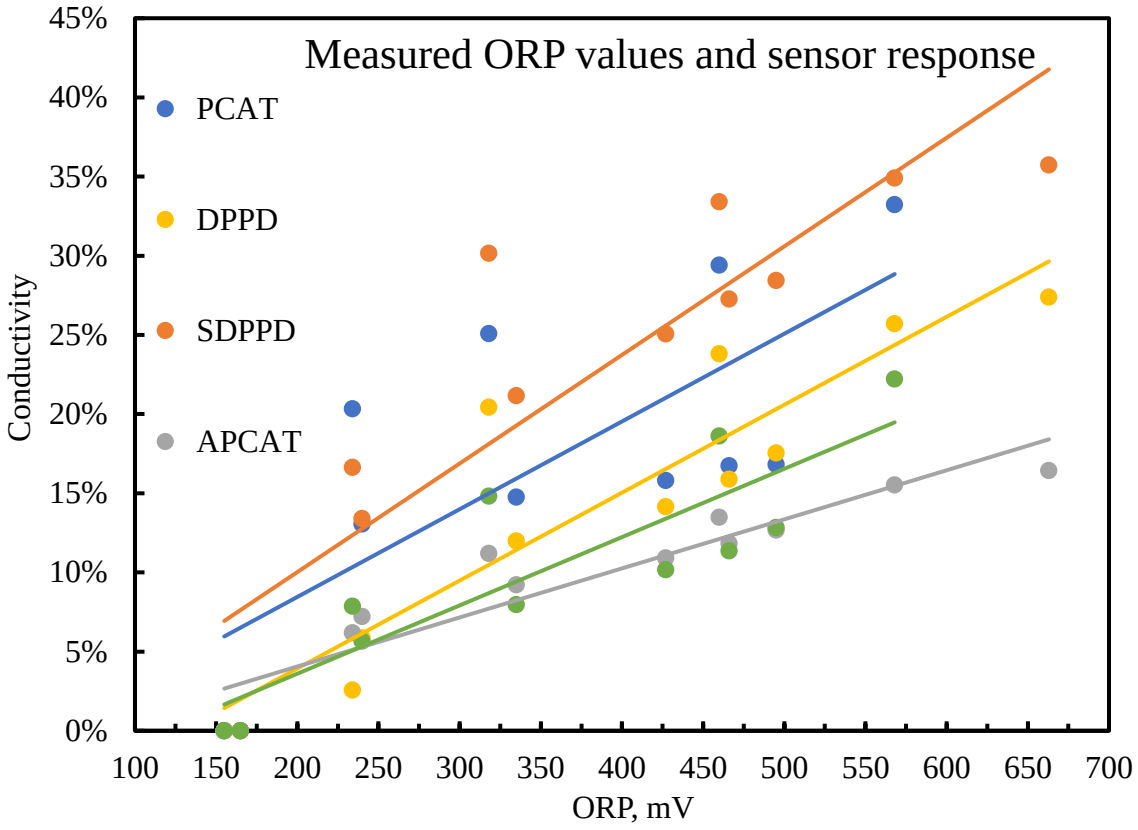

Figure 90: Relationship between sensor response and measured ORP values for free chlorine and $KMnO_4$ analytes

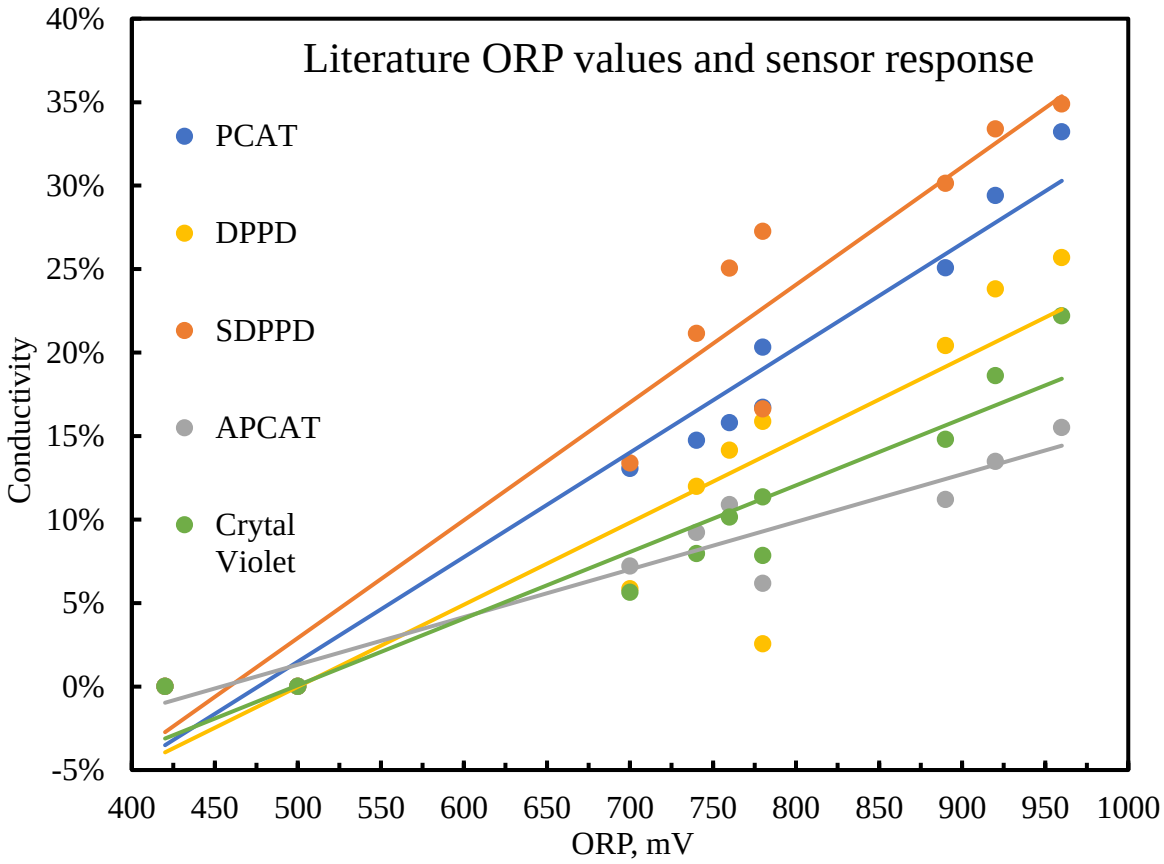

Figure 91: Relationship between sensor response and literature ORP values for free chlorine and $KMnO_4$ analytes

We calculated the deviation of sensor response associated ORP values from analytes actual ORP values which are shown in Figure 92 and Figure 93. There is a clear relationship between deviation from analytes actual ORP value and sensor response associated ORP values. The deviation seems to have a relationship with the complete oxidation potentials (potential where molecules get fully oxidized) of our redox molecules. The sensor response deviates from actual ORP with increasing value of complete oxidation potentials.

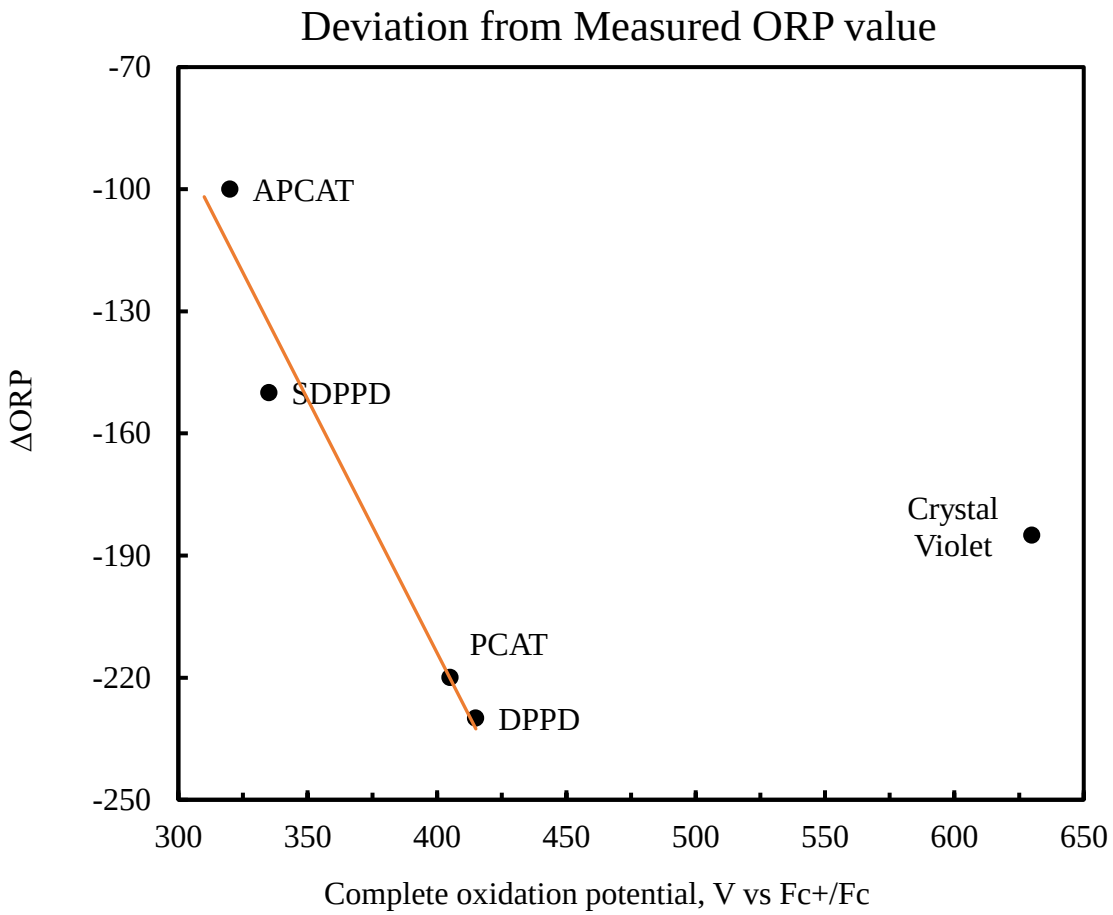

Figure 92: Relationship between the deviation from ORP and oxidation potential for measured ORP values

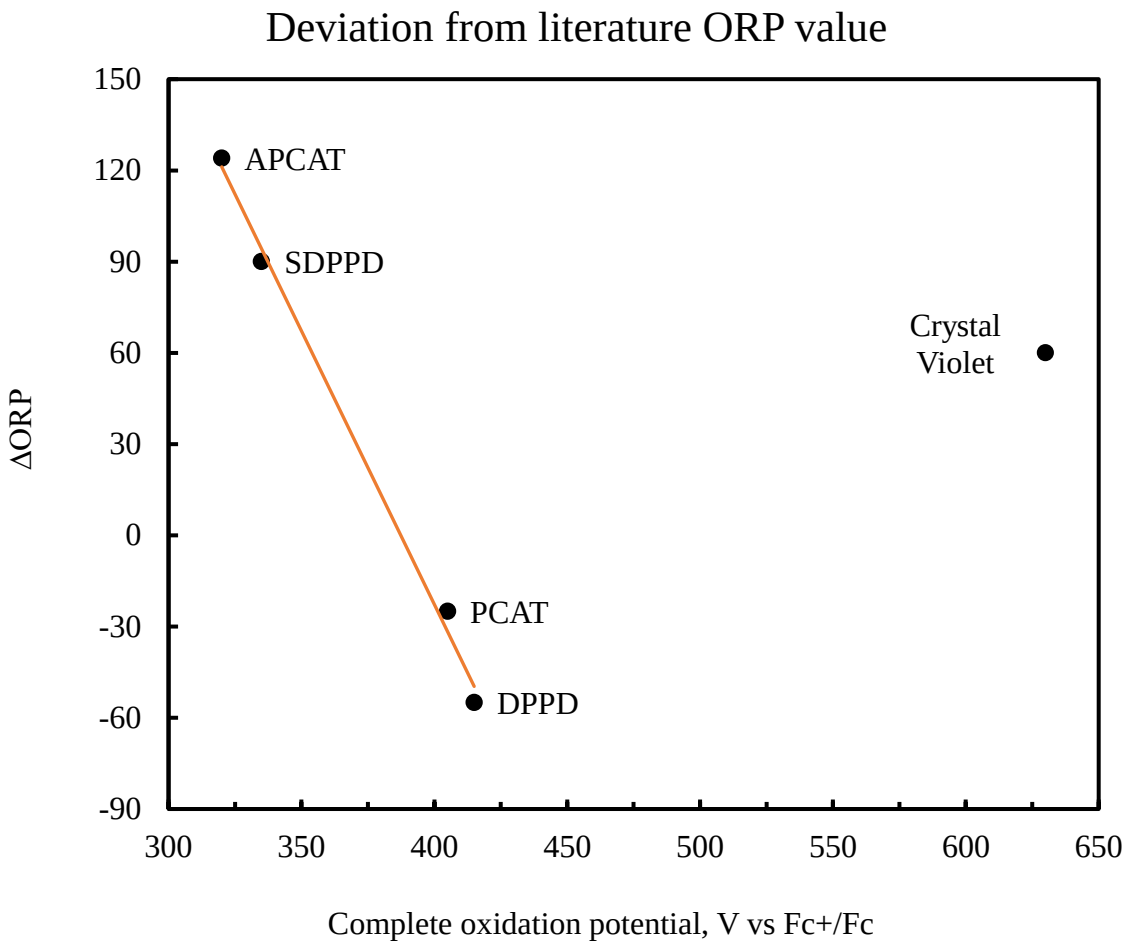

Figure 93: Relationship between the deviation from ORP and oxidation potential for literature ORP values

Even though our measured values and literature values give different deviations, overall they show a comparable trend in both cases. The crystal violet looks like an outlier in this relationship, possibly due to the structural difference compared to aniline oligomers. Crystal violet might be interacting differently with nanotubes than the aniline oligomers.

Given that our sensor is not a true ORP sensor we could utilize the deviation from the actual ORP values to identify and measure the concentration of the disinfectants. The outline for calculation is discussed below.

We tried to find a mathematical model system to fit our sensor response which can also be used to calculate the effect of molecules on the sensing response. We tried both an exponential and a Langmuir adsorption isotherm model. The Langmuir isotherm fits the sensor measurements better. This might be due to the interaction of disinfectants at the substrate surfaces and formation of a redox equilibrium between disinfectant and molecule.

For any instance, if we take the sensor signal current as I, referencing it with 0 ppm analytes we can calculate the change in conductivity signal for the sensor programmed with molecule m, which will be $I_{m.}$

$$I_m = \frac{I - I_o}{I_o} \qquad (2)$$

For any molecule, we can write the sensor response equation in the Langmuir adsorption isotherm model

$$I_m = A\frac{BC}{1+ BC} \qquad (3)$$

$$C = \frac{I_m}{(A- I_m)B} \qquad (4)$$

Where A is related to the amplitude of the sensor response for a specific sensor geometry and a specific redox molecule and disinfectant pair; B is effectively a chemical

equilibrium constant for a specific molecule and disinfectant pair; and C is the concentration of the disinfectant. For a two disinfectant system that could contain either one of two different disinfectants e.g. free chlorine and $KMnO_4$, we can calculate all the characteristic constant values (A and B) for the molecules and disinfectants such as $A_{m,Cl}$, $B_{m,Cl}$, $A_{m,Mn}$, $B_{m,Mn}$. Characteristic constants for five redox active molecules and two different disinfectants are given in Table 5. The constants were obtained by fitting the data in Figures 79-83 to equation (3). This will be our database for a two-disinfectant system.

Table 5: Characteristic constants for different disinfectants

Molecule		Characteristic Constants	
PCAT		**Free Chlorine**	**$KMnO_4$**
	A	0.375	0.175
	B	2.05	5
DPPD		**Free Chlorine**	**$KMnO_4$**
	A	0.287	0.186
	B	2.45	1.8
SDPPD		**Free Chlorine**	**$KMnO_4$**
	A	0.376	0.303
	B	3.6	2.3
APCAT		**Free Chlorine**	**$KMnO_4$**
	A	0.178	0.131
	B	1.6	2.6
Crystal Violet		**Free Chlorine**	**$KMnO_4$**
	A	0.281	0.138
	B	1	1.35

For a pair of molecules and an unknown disinfectant at a constant concentration, the following equation (5) must be true. For this case, we are showing the relation for DPPD (as D) and SDPPD (as S) molecules as they are two distinct molecules in the ORP deviation relationship.

$$C = \frac{I_S}{(A_{SX} - I_S)B_{SX}} = \frac{I_D}{(A_{DX} - I_S)B_{DX}} \qquad (5)$$

By plugging in characteristics constants in equation (5), if the above equation is true for a disinfectant we will be able to identify that disinfectant. After identifying the disinfectant, we can calculate the concentration from the following equation (6).

$$C = \frac{I_m}{(A - I_m)B} \qquad (6)$$

As an example, let's consider a DPPD and SDPPD sensor measurements for an unknown concentration. The DPPD sensor gives 14.33% sensor response and SDPPD gives 24.58% sensing response for that unknown concentration. Our disinfectant could be either free chlorine or permanganate. By plugging in characteristic for free chlorine we could see

$$\frac{I_S}{(A_{SX} - I_S)B_{SX}} = \frac{I_D}{(A_{DX} - I_S)B_{DX}} \qquad (7a)$$

$$\frac{.2458}{(0.376 - .2458)3.6} = \frac{0.1433}{(0.287 - .1433)2.45} \qquad (7b)$$

$$0.524 \neq 0.4070 \qquad (7c)$$

Therefore, it's not free chlorine. Plugging in characteristic constants for permanganate we can see that the equation is true for permanganate.

$$\frac{I_S}{(A_{SX} - I_S)B_{SX}} = \frac{I_D}{(A_{DX} - I_S)B_{DX}} \qquad (8a)$$

$$\frac{.2458}{(0.303 - .2458)2.3} = \frac{0.1433}{(0.186 - .1433)1.8} \qquad (8b)$$

$$1.868 = 1.864 \qquad (8c)$$

Now we can use the characteristic constants of permanganate to calculate the permanganate concentration from any of the sensors. The disinfectant concentration is 1.86 ppm.

Therefore, this approach will be used to identify the disinfectant and at the same time the concentration of the disinfectant. Our original goal was to make a sensor array with different redox active molecules, which seems achievable by using the characteristics of different molecules. If we know what disinfects are used for a water system, we could build our sensor characteristic constant database for that system for monitoring and identification. Our sensor measurement was done at a pH 7.5, this approach will be appropriate at constant pH. The sensor array may not be able to correctly identify when both disinfects are present. In many cases, one disinfect neutralizes the other and the remaining one will dominate the sensor signal. One such system is a dehydrochlorination unit where hydrogen peroxide is used to neutralize free chlorine.

After successfully identifying the disinfectant and measuring the disinfectant concentration we can calculate the ORP value from equation 9. X, Y, and Z are the characteristic constants for a specific disinfectant and can be easily calculated from the measured or literature ORP values of that disinfectant.

$$E_{mv} = \text{Standard reduction potential} + X \log(\text{Oxidant Concentration}) - \text{YpH} - Z \qquad (9)$$

$$X,Y,Z = \text{constants}$$

Therefore, a sensor array with just two sensors can be used to identify disinfectants and monitor disinfectant concentration. We can also calculate the ORP values of the disinfectant.

The above approach is shown at constant pH. We can possibly further extend our analysis to measure pH of the solution by adding information from one more molecule. The pH has a role in the sensing response, therefore, adding a pH factor into equation (3) will lead us to three unknowns with three equations. By solving the equations, we should be able to calculate the pH. To do the pH setting in our sensing response we need a large number of sensing response data for variable pH solutions and possibly find a coherent relationship with the pH changes.

5.5.2. DPPD AS POSSIBLE pH SENSOR

Four of our redox active molecules are aniline compounds and they are responsive to pH. The comparison of pH sensing response between a blank sensor and a DPPD sensor is shown in Figure 89. The range of pH tested here are from pH 11.26 to pH 2.37. The sensor response was plotted relative to the baseline current at pH 11.26.

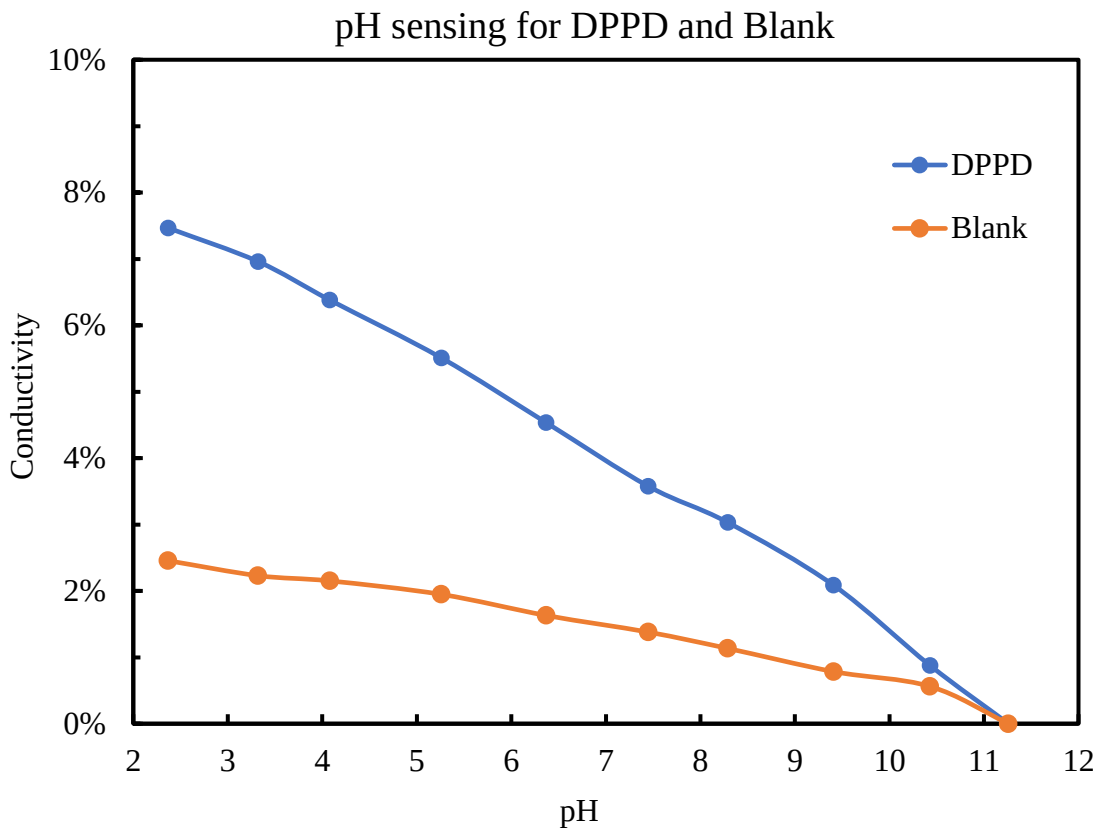

Figure 94: pH sensing comparison of DPPD sensor and pristine carbon nanotubes

The conductivity of pristine nanotubes is affected by the presence of OH^- and H_3O^+ ions and thus responds to a change in pH. The change in response for pH 2.37 was around 2.45% relative to the sensor response at pH 11.26. Aniline compounds are responsive to changes in pH due to the formation of a salt in an acidic environment and formation of a free base in a basic environment. Non-covalently functionalized DPPD shows a sensor response of 7.4% at pH 2.37. The increased pH response is coming from the synergistic effect of both pristine carbon nanotubes and the charge transfer between the salt and base formation at the surface of the carbon nanotubes. This plot shows the promise of developing a pH sensor

based on noncovalent functionalization of nanotubes with pH responsive molecules. However, we have seen that in the presence of oxidizing agents, DPPD molecules will be more responsive to oxidizing properties of the solution than pH.

5.5.3. DISTINGUISHING BETWEEN FREE CHLORINE AND HYDROGEN PEROXIDE

One of the goals of this research was to distinguish between free chlorine and hydrogen peroxide based on the simple sensing difference of two different redox molecules. Even though in theory hydrogen peroxide (E_o = 1.76 V) is a stronger oxidant than free chlorine (E_o = 1.49 V) in actual solution it works as a weaker oxidant (E_o = 0.87 V) than free chlorine. This is due to hydrogen peroxide oxidation requiring the formation of free radical activation to work as a strong oxidant. The following two experiments show a promising pathway towards distinguishing between free chlorine and hydrogen peroxide.

The PCAT sensor response is shown in Figure 95 for free chlorine and hydrogen peroxide. The redox active molecule PCAT is easier to oxidize by both the disinfectants and they both give a sensing response. The figure shows the sensing comparison for 2 ppm and 4 ppm H_2O_2 and 1 ppm free chlorine. Free chlorine is a stronger oxidant thus giving a higher sensing response compared to the H_2O_2 sensing response.

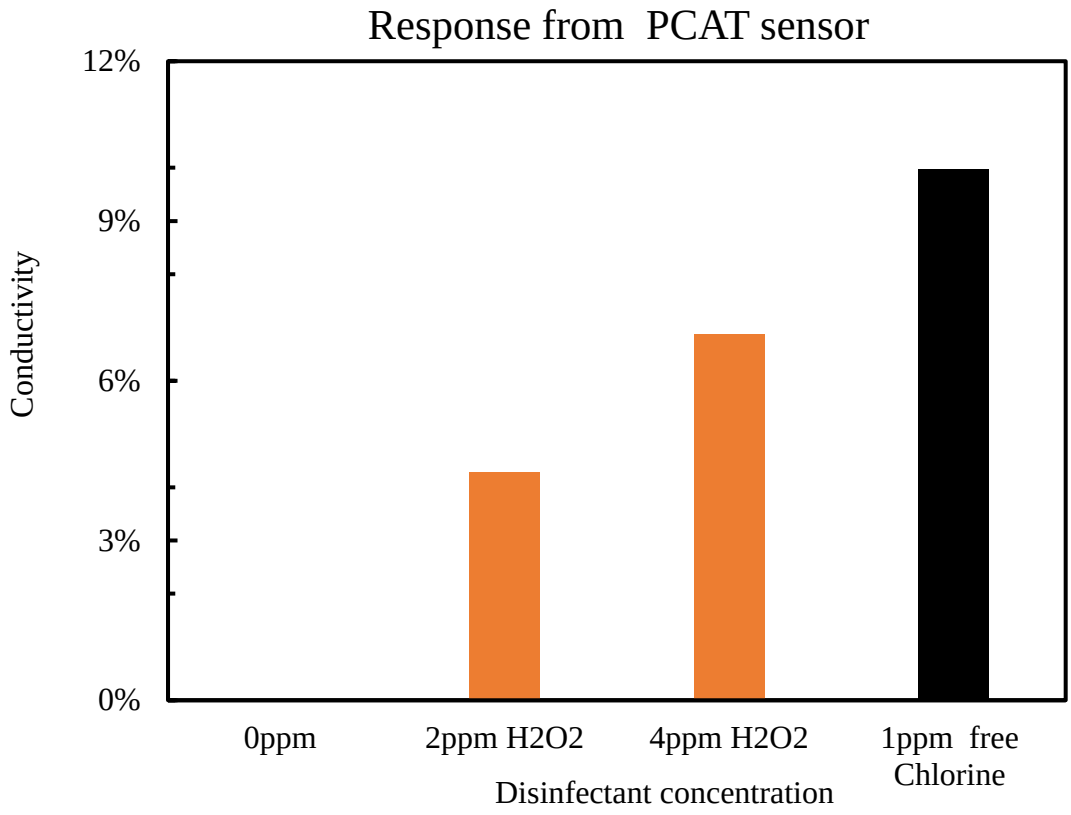

Figure 95: PCAT sensor response for hydrogen peroxide and free chlorine

The sensing responses of emeraldine APCAT is shown in Figure 96 for hydrogen peroxide and free chlorine. We know that half oxidized APCAT is relatively harder to oxidize than reduced PCAT since it was ranked 6th in our ease of oxidation ranking. So, it was a good candidate to test for distinguishing between hydrogen peroxide and free chlorine. Hydrogen peroxide doesn't show a sensing response for both 2 ppm and 4 ppm solution. On the other hand, the emeraldine APACT gives a response to 1 ppm free chlorine. The 1 ppm free chlorine response is smaller compared to PCAT response. This experiment strongly suggests that by using molecules with different redox potential it is possible to distinguish between two different oxidizing agents.

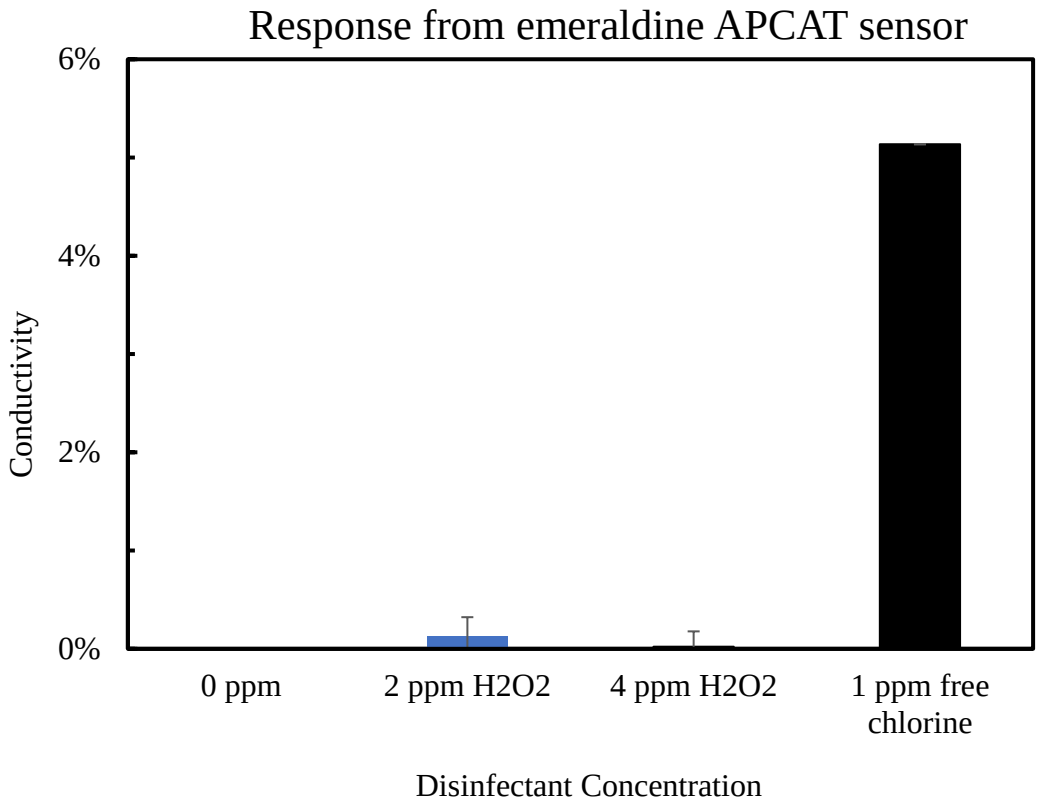

Figure 96: Emeraldine APCAT sensor response for hydrogen peroxide and free chlorine

5.6. SUMMARY

In summary, we have performed spectroscopic and electrochemical characterization of five different redox active molecules. Sensor response performance was discussed for free chlorine and $KMnO_4$ in terms of the redox potential of the molecules. We have found that the sensor response is related to the oxidation reduction potential of the analyte solutions. Change in pH has a significant effect on the oxidizing power of a disinfectant which is also related to the oxidation reduction potential of analytes. Sensor response was found to fit a Langmuir adsorption isotherm model which explains disinfectant and redox-active

molecule interaction at nanotube surfaces. For different molecules, the interactions are quantitively different and the interactions can be utilized to identify and monitor the disinfectant. We have discussed an approach to identify the disinfectant and measure the disinfectant concentration using different redox active molecules. We have also shown to differentiate between free chlorine and hydrogen peroxide using emeraldine APCAT and PCAT sensors.

CHAPTER 6: SUMMARY AND FUTURE WORK

6.1. SUMMARY

This thesis project highlights an approach of developing redox chemiresistors for continuous disinfectant monitoring and distinguishing between different disinfectants based on potentials of redox-active molecules.

In chapter 1, we discussed the motivation behind continuous disinfectant monitoring for improved disinfection of water. We introduced our sensing mechanism based on a carbon nanotube chemiresistive sensor functionalized with redox active molecule. We discussed the effect of pH in disinfection and importance of monitoring pH in addition to disinfectant concentration. Synthesis and characterization of redox-active molecules and pyrenated neutral red derivatives were presented in chapter 3. In chapter 4, different nanocarbon substrates were compared to select suitable substrate materials for studying the interactions of redox-active molecules. The sensors were fabricated and tested following the SOPs in Appendix 1 and Appendix 2. We have found that 95% semiconducting carbon nanotubes are a suitable substrate material among our tested nanocarbons. We have found that the content of metal impurities present in the substrate, the substrate film thickness and surface wetting by organic solvents all have a significant effect on the sensing response. These parameters should be controlled for better chemiresistive sensor performance. Characterization of the sensor response for different redox-active molecules was presented in chapter 5. We have found that the sensing response is directly related to the oxidation reduction potential of analytes. Three different disinfectants were tested to find the possibilities of differentiating between disinfectants. We have shown two different

approaches to distinguish between different disinfectants. Quantitatively calculated characteristic constants of molecule-disinfectant interaction were used to both identify and monitor disinfectants. We have found that to successfully differentiate between disinfectants pH monitoring must be done in addition to disinfectant monitoring.

6.2. FUTURE WORK

In this thesis, we only relied on a chemiresistive device configuration for selecting substrate material. It would be useful to compare between other device configurations i.e. FET for studying the interactions of redox-active molecules at substrate surfaces.

One of the biggest challenges of this study was to fabricate reproducible substrate films. Studies should be done on the fabrication of reproducible substrate films for better comparison of molecules at nanocarbon surfaces.

We have synthesized pyrenated neutral red derivatives for pH sensing applications. The pH indicator should be tested in a sensor for possible pH chemiresistors.

We have seen that free chlorine is very unstable at lower concentration and degrades rapidly reacting with container materials. Syringes and tube made from inert materials should be tried in the future for handling free chlorine for slower degradation.

In chapter 5, we have discussed our approach to identify and monitor disinfectants. The strategy was designed at constant pH. More experimental studies at different pH could help us to build a database system which will be able to monitor pH in addition to identification and monitoring the disinfectants.

In chapter 4 and 5, we have seen that surface wetting of a dry sensor has a significant effect on the sensing response. The surface wetting effect should be studied in the future to find suitable solvents for molecule depositions.

BIBLIOGRAPHY

(1) Hsu, L. H. H.; Hoque, E.; Kruse, P.; Ravi Selvaganapathy, P. A Carbon Nanotube Based Resettable Sensor for Measuring Free Chlorine in Drinking Water. *Appl. Phys. Lett.* **2015**, *106* (6), 63102.

(2) Srinivasan, S.; Harrington, G. W. Biostability Analysis for Drinking Water Distribution Systems. *Water Res.* **2007**, *41* (10), 2127–2138.

(3) LeChevallier, M. W.; Schneider, O. D.; Weinrich, L. A.; Jjemba, P. K.; Evans, P. J.; Hooper, J. L.; Chappell, R. W. An Operational Definition of Biostability in Drinking Water. 2015.

(4) Ueno, H.; Nakamuro, K.; Moto, T.; Sayato, Y. Disinfection by-Products in the Chlorination of Organic Nitrogen Compounds: Possible Pathways for the Formation of Disinfection by-Products. *Water Supply* **1995**, *13* (3–4), 171–176.

(5) Badawy, M. I.; Gad-Allah, T. A.; Ali, M. E. M.; Yoon, Y. Minimization of the Formation of Disinfection by-Products. *Chemosphere* **2012**, *89* (3), 235–240.

(6) Kim, H. C.; Yu, M. J. Characterization of Natural Organic Matter in Conventional Water Treatment Processes for Selection of Treatment Processes Focused on DBPs Control. *Water Res.* **2005**, *39* (19), 4779–4789.

(7) Pereira, M. A.; Lin, L. H. C.; Lippitt, J. M.; Herren, S. L. Trihalomethanes as Initiators and Promoters of Carcinogenesis. *Environmental Health Perspectives*. National Institute of Environmental Health Science December 1982, pp 151–156.

(8) Amy, G. L.; Bull, R.; Craun, G. F.; Pegram, R. a.; Siddiqui, M. Disinfectants and Disinfectant by-Products. *Environmental Health Criteria*. 2000, p 499.

(9) Yang, X.; Peng, J.; Chen, B.; Guo, W.; Liang, Y.; Liu, W.; Liu, L. Effects of Ozone and Ozone/peroxide Pretreatments on Disinfection Byproduct Formation during Subsequent Chlorination and Chloramination. *J. Hazard. Mater.* **2012**, *239–240*, 348–354.

(10) Linden, K. G.; Malley, J. P. J. *Ultraviolet Disinfection Guidance Manual for the Final Long Term 2 Enhanced Surface Water Treatment Rule*; 2006; Vol. EPA 815-R-.

(11) USEPA. National Primary Drinking Water Regulations: Long Term 2 Enhanced Surface Water Treatment Rule. *Fed. Regist.* **2006**, *71* (3), 654–786.

(12) EPA. *Water Treatment Manual : Disinfection*; 2013.

(13) Berry, D.; Xi, C.; Raskin, L. Microbial Ecology of Drinking Water Distribution Systems. *Current Opinion in Biotechnology*. June 2006, pp 297–302.

(14) Codony, F.; Morató, J.; Mas, J. Role of Discontinuous Chlorination on Microbial Production by Drinking Water Biofilms. *Water Res.* **2005**, *39* (9), 1896–1906.

(15) Gagnon, G. A.; Rand, J. L.; O'Leary, K. C.; Rygel, A. C.; Chauret, C.; Andrews, R. C. Disinfectant Efficacy of Chlorite and Chlorine Dioxide in Drinking Water Biofilms. *Water Res.* **2005**, *39* (9), 1809–1817.

(16) US EPA. *Guidance Manual - Alternative Disinfectants and Oxidants*; 1999.

(17) Harp, D. L. Current Technology of Chlorine Analysis for Water and Wastewater. *Tech. Inf. Ser.* **2002**, No. 17, 34.

(18) Salvadori, M. I.; Sontrop, J. M.; Garg, A. X.; Moist, L. M.; Suri, R. S.; Clark, W. F. Factors That Led to the Walkerton Tragedy. *Kidney Int. Suppl.* **2009**, *75* (112), S33–S34.

(19) June, T.; Brown, J. C. PPM or ORP : Which Should Be Used ? *Water* **1985**, No. November.

(20) Suslow, T. V. Oxidation-Reduction Potential (ORP) for Water Disinfection Monitoring , Control , and Documentation. *ANR Publ.* **2004**, *8149*, 1–5.

(21) Steininger, J. M.; Pareja, C. Orp Sensor Response. *NSPI Symp. Ser.* **1996**, *I*, 1–9.

(22) Joachim, C.; Gimzewski, J. K.; Aviram, A. Electronics Using Hybrid-Molecular and Mono-Molecular Devices. *Nature* **2000**, *408* (6812), 541–548.

(23) Nichols, R. J.; Gittins, D. I.; Bethell, D.; Schiffrin, D. J. A Nanometre-Scale Electronic Switch Consisting of a Metal Cluster andRedox-Addressable Groups. *Nature* **2000**, *408* (6808), 67–69.

(24) Blum, A. S.; Kushmerick, J. G.; Long, D. P.; Patterson, C. H.; Yang, J. C.; Henderson, J. C.; Yao, Y.; Tour, J. M.; Shashidhar, R.; Ratna, B. R. Molecularly Inherent Voltage-Controlled Conductance Switching. *Nat. Mater.* **2005**, *4* (2), 167–172.

(25) Chen, F.; He, J.; Nuckolls, C.; Roberts, T.; Klare, J. E.; Lindsay, S. A Molecular

Switch Based on Potential-Induced Changes of Oxidation State. *Nano Lett.* **2005**, *5* (3), 503–506.

(26) Collier, C. P.; Wong, E. W.; Belohradsky, M.; Raymo, F. M.; Stoddart, J. F.; Kuekes, P. J.; Williams, R. S.; Heath, J. R.; Chen, R. H.; Korotov, A. N.; et al. Electronically Configurable Molecular-Based Logic Gates. *Science* **1999**, *285* (5426), 391–394.

(27) Li, Q.; Surthi, S.; Mathur, G.; Gowda, S.; Misra, V.; Sorenson, T. A.; Tenent, R. C.; Kuhr, W. G.; Tamaru, S.; Lindsey, J. S.; et al. Electrical Characterization of Redox-Active Molecular Monolayers on SiO[sub 2] for Memory Applications. *Appl. Phys. Lett.* **2003**, *83* (1), 198.

(28) Liao, J.; Agustsson, J. S.; Wu, S.; Schonenberger, C.; Calame, M.; Leroux, Y.; Mayor, M.; Jeannin, O.; Ran, Y.-F.; Liu, S.-X.; et al. Cyclic Conductance Switching in Networks of Redox Active Molecular Junctions. *Nano Lett.* **2010**.

(29) Janata, J.; Josowicz, M. Conducting Polymers in Electronic Chemical Sensors. *Nat. Mater.* **2003**, *2* (1), 19–24.

(30) McQuade, D. T.; Pullen, A. E.; Swager, T. M. Conjugated Polymer-Based Chemical Sensors. *Chem. Rev.* **2000**, *100* (7), 2537вЂ“2574.

(31) Eugenii Katz; Oleg Lioubashevsky, and; Willner*, I. Electromechanics of a Redox-Active Rotaxane in a Monolayer Assembly on an Electrode. **2004**.

(32) Li, Z.; Pobelov, I.; Han, B.; Wandlowski, T.; Błaszczyk, A.; Mayor, M.; M, A. A. and R.; Joachim C, G. J. K. and A. A.; S, M. B. and W. P.; al, A. D. M. et; et al.

Conductance of Redox-Active Single Molecular Junctions: An Electrochemical Approach. *Nanotechnology* **2007**, *18* (4), 44018.

(33) Mahapatro, A. K.; Ying, J.; Ren, T.; Janes, D. B. Electronic Transport through Molecules in Metal - Molecule - Metal Nanogap Junctions. **2008**.

(34) Chen, F.; He, J.; Nuckolls, C.; Roberts, T.; Klare, J. E.; Lindsay, S. Supporting Online Information for : A Molecular Switch Based on Potential-Induced Changes of Oxidation State . **2005**, 1–5.

(35) Klinke, C.; Chen, J.; Afzali, A.; Avouris, P. Charge Transfer Induced Polarity Switching in Carbon Nanotube Transistors. *Nano Lett.* **2005**, *5* (3), 555–558.

(36) Chen, S.-A.; Chuang, K.-R.; Chao, C.-I.; Lee, H.-T. White-Light Emission from Electroluminescence Diode with Polyaniline as the Emitting Layer. *Synth. Met.* **1996**, *82* (3), 207–210.

(37) MacDiarmid, A. G. Polyaniline and Polypyrrole: Where Are We Headed? *Synth. Met.* **1997**, *84* (1–3), 27–34.

(38) Kuo, C.-T.; Chiou, W.-H. Field-Effect Transistor with Polyaniline Thin Film as Semiconductor. *Synth. Met.* **1997**, *88* (1), 23–30.

(39) Kilmartin, P. A.; Trier, L.; Wright, G. A. Corrosion Inhibition of Polyaniline and Poly(o-Methoxyaniline) on Stainless Steels. *Synth. Met.* **2002**, *131* (1), 99–109.

(40) Baughman, R. H.; Madden, J. D.; Baughman, R. H.; Hara, S.; Bar-Cohen, Y.; Smela, E.; Inganäs, O.; Lundström, I.; Smela, E.; Hara, S.; et al. Materials Science. Playing

Nature's Game with Artificial Muscles. *Science* **2005**, *308* (5718), 63–65.

(41) Monkman, A. P.; Petty, M. C.; Agbor, N. E.; Scully, M. T. Polyaniline Gas Sensor. 1996.

(42) Baughman, R. H.; Zakhidov, A. A.; de Heer, W. A.; Louie, S. G.; Liang, W.; Frank, S. P.; Poncharal, P.; Wang, Z. L.; Heer, W. A. de; Kim, P.; et al. Carbon Nanotubes--the Route toward Applications. *Science* **2002**, *297* (5582), 787–792.

(43) Lemme, M. C.; Echtermeyer, T. J.; Baus, M.; Kurz, H. A Graphene Field-Effect Device. *IEEE Electron Device Lett.* **2007**, *28* (4), 282–284.

(44) Radisavljevic, B.; Radenovic, A.; Brivio, J.; Giacometti, V.; Kis, A. Single-Layer MoS2 Transistors. *Nat. Nanotechnol.* **2011**, *6* (3), 147–150.

(45) Luo, X.; Killard, A. J.; Morrin, A.; Smyth, M. R. Enhancement of a Conducting Polymer-Based Biosensor Using Carbon Nanotube-Doped Polyaniline. *Anal. Chim. Acta* **2006**, *575* (1), 39–44.

(46) He, L.; Jia, Y.; Meng, F.; Li, M.; Liu, J. Gas Sensors for Ammonia Detection Based on Polyaniline-Coated Multi-Wall Carbon Nanotubes. *Mater. Sci. Eng. B* **2009**, *163* (2), 76–81.

(47) Srivastava, S.; Sharma, S. S.; Agrawal, S.; Kumar, S.; Singh, M.; Vijay, Y. K. *Study of Chemiresistor Type CNT Doped Polyaniline Gas Sensor*; 2010; Vol. 160.

(48) Kim, T. Y.; Yang, S. Fabrication Method and Characterization of Electrodeposited and Heat-Treated Iridium Oxide Films for pH Sensing. *Sensors Actuators B Chem.*

2014, *196*, 31–38.

(49) Sheppard Jr., N. F.; Lesho, M. J.; McNally, P.; Shaun Francomacaro, A. Microfabricated Conductimetric pH Sensor. *Sensors Actuators B Chem.* **1995**, *28* (2), 95–102.

(50) Zhujun, Z.; Seitz, W. R. A Fluorescence Sensor for Quantifying pH in the Range from 6.5 to 8.5. *Anal. Chim. Acta* **1984**, *160*, 47–55.

(51) Saari, L. A.; Seitz, W. R. pH Sensor Based on Immobilized Fluoresceinamine. *Anal. Chem.* **1982**, *54* (4), 821–823.

(52) Lin, J. Recent Development and Applications of Optical and Fiber-Optic pH Sensors. *TrAC - Trends in Analytical Chemistry*. 2000, pp 541–552.

(53) Zoski, C. G. *Handbook of Electrochemistry. 4th Ed.*; Elsevier, 1985.

(54) Bard, A. J.; Faulkner, L. R. *Fundamentals and Fundamentals and Applications*; 2015; Vol. 8.

(55) Kissinger, P. T.; Heineman, W. R. Cyclic Voltammetry. *J. Chem. Educ.* **1983**, *60* (9), 702.

(56) Gary A. Mabbott. An Introduction to Cyclic Voltammetry. *J. Chem. Educ.* **1983**, *60* (9), 697.

(57) Aoki, K.; Tokuda, K.; Matsuda, H. Theory of Differential Pulse Voltammetry at Stationary Planar Electrodes. *J. Electroanal. Chem. Interfacial Electrochem.* **1984**, *175* (1–2), 1–13.

(58) Wang, W.; MacDiarmid, A. G. New Synthesis of Phenyl/phenyl End-Capped Tetraaniline in the Leucoemeraldine and Emeraldine Oxidation States. *Synth. Met.* **2002**, *129* (2), 199–205.

(59) Singh, Y. Electrical Resistivity Measurements: A Review. *India Int. J. Mod. Phys. Conf. Ser.* **2013**, *22*, 745–756.

(60) Dunlap, W. C.; Matare, H. F. An Introduction to Semiconductors. *J. Electrochem. Soc.* **1957**, *104* (9), 201C.

(61) Grundmann, M. *The Physics of Semiconductors: An Introduction Including Devices and Nanophysics*; 2006.

(62) Wolfe, J. P.; Wagaw, S.; Marcoux, J.-F.; Buchwald, S. L. Rational Development of Practical Catalysts for Aromatic Carbon-Nitrogen Bond Formation. *Acc. Chem. Res.* **1998**, *31* (12), 805–818.

(63) Surry, D. S.; Buchwald, S. L.; Echavarren, A. M.; Yamamoto, A.; Lemaire, M.; Spannenberg, A.; Neumann, H.; Borner, A.; Beller, M.; Joffe, M.; et al. Dialkylbiaryl Phosphines in Pd-Catalyzed Amination: A User's Guide. *Chem. Sci.* **2011**, *2* (1), 27–50.

(64) Hartwig, J. F. Transition Metal Catalyzed Synthesis of Arylamines and Aryl Ethers from Aryl Halides and Triflates: Scope and Mechanism. *Angew. Chemie Int. Ed.* **1998**, *37* (15), 2046–2067.

(65) Surry, D. S.; Buchwald, S. L. Biaryl Phosphane Ligands in Palladium-Catalyzed

Amination. *Angew. Chemie Int. Ed.* **2008**, *47* (34), 6338–6361.

(66) Hartwig, J. F. Evolution of a Fourth Generation Catalyst for the Amination and Thioetherification of Aryl Halides. *Acc. Chem. Res.* **2008**, *41* (11), 1534–1544.

(67) Evano, G.; Blanchard, N.; Toumi, M. Copper-Mediated Coupling Reactions and Their Applications in Natural Products and Designed Biomolecules Synthesis. *Chem. Rev.* **2008**, *108* (8), 3054–3131.

(68) Monnier, F.; Taillefer, M. Catalytic C-C, C-N, and C-O Ullmann-Type Coupling Reactions. *Angewandte Chemie - International Edition*. September 7, 2009, pp 6954–6971.

(69) Beletskaya, I. P.; Cheprakov, A. V. Copper in Cross-Coupling Reactions. *Coord. Chem. Rev.* **2004**, *248* (21–24), 2337–2364.

(70) Old, D. W.; Wolfe, J. P.; Buchwald, S. L. A Highly Active Catalyst for Palladium-Catalyzed Cross-Coupling Reactions: Room-Temperature Suzuki Couplings and Amination of Unactivated Aryl Chlorides. *J. Am. Chem. Soc.* **1998**, *120* (37), 9722–9723.

(71) Yin, J.; Buchwald, S. L. Palladium-Catalyzed Intermolecular Coupling of Aryl Halides and Amides. *Org. Lett.* **2000**, *2* (8), 1101–1104.

(72) Castillo, J. C.; Orrego-Hernndez, J.; Portilla, J. Cs2CO3-Promoted Direct N-Alkylation: Highly Chemoselective Synthesis of N-Alkylated Benzylamines and Anilines. *European J. Org. Chem.* **2016**, *2016* (22), 3824–3835.

(73) Salvatore, R. N.; Nagle, A. S.; Jung, K. W. Cesium Effect: High Chemoselectivity in Direct N-Alkylation of Amines.

(74) Rebourt, E.; Joule, J. A.; Monkman, A. P. Polyaniline Oligomers; Synthesis and Characterisation. *Synth. Met.* **1997**, *84* (1–3), 65–66.

(75) Wang, F.; Gu, H.; Swager, T. M. Carbon Nanotube/Polythiophene Chemiresistive Sensors for Chemical Warfare Agents. *J. Am. Chem. Soc.* **2008**, *130* (16), 5392–5393.

(76) Shirsat, M. D.; Bangar, M. A.; Deshusses, M. A.; Myung, N. V.; Mulchandani, A. Polyaniline Nanowires-Gold Nanoparticles Hybrid Network Based Chemiresistive Hydrogen Sulfide Sensor. *Appl. Phys. Lett.* **2009**, *94* (8), 83502.

(77) Cella, L. N.; Chen, W.; Myung, N. V.; Mulchandani, A. Single-Walled Carbon Nanotube-Based Chemiresistive Affinity Biosensors for Small Molecules: Ultrasensitive Glucose Detection. *J. Am. Chem. Soc.* **2010**, *132* (14), 5024–5026.

(78) Tlili, C.; Cella, L. N.; Myung, N. V.; Shetty, V.; Mulchandani, A. Single-Walled Carbon Nanotube Chemoresistive Label-Free Immunosensor for Salivary Stress Biomarkers. *Analyst* **2010**, *135* (10), 2637.

(79) Kolmakov, A.; Moskovits, M. Chemical Sensing and Catalysis By One-Dimensional Metal-Oxide Nanostructures. *Annu. Rev. Mater. Res.* **2004**, *34* (1), 151–180.

(80) Hangarter, C. M.; Bangar, M.; Mulchandani, A.; Myung, N. V. Conducting Polymer Nanowires for Chemiresistive and FET-Based Bio/chemical Sensors. *J. Mater.*

Chem. **2010**, *20* (16), 3131.

(81) Meng, F. L.; Guo, Z.; Huang, X. J. Graphene-Based Hybrids for Chemiresistive Gas Sensors. *TrAC - Trends in Analytical Chemistry*. May 2015, pp 37–47.

(82) Nikolaev, P.; Bronikowski, M. J.; Bradley, R. K.; Rohmund, F.; Colbert, D. T.; Smith, K. .; Smalley, R. E. Gas-Phase Catalytic Growth of Single-Walled Carbon Nanotubes from Carbon Monoxide. *Chem. Phys. Lett.* **1999**, *313* (1–2), 91–97.

(83) Bronikowski, M. J.; Willis, P. A.; Colbert, D. T.; Smith, K. A.; Smalley, R. E. Gas-Phase Production of Carbon Single-Walled Nanotubes from Carbon Monoxide via the HiPco Process: A Parametric Study. *J. Vac. Sci. Technol. A Vacuum, Surfaces, Film.* **2001**, *19* (4), 1800–1805.

(84) Liu, X.; Pichler, T.; Knupfer, M.; Fink, J.; Kataura, H. Electronic Properties of FeCl3-Intercalated Single-Wall Carbon Nanotubes. *Phys. Rev. B* **2004**, *70* (20), 205405.

(85) Moonoosawmy, K. R.; Kruse, P. To Dope or Not To Dope: The Effect of Sonicating Single-Wall Carbon Nanotubes in Common Laboratory Solvents on Their Electronic Structure. *J. Am. Chem. Soc.* **2008**, *130* (40), 13417–13424.

(86) Greiner, M. T.; Festin, M.; Kruse, P. Investigation of Corrosion-Inhibiting Aniline Oligomer Thin Films on Iron Using Photoelectron Spectroscopy. *J. Phys. Chem. C* **2008**, *112* (48), 18991–19004.

(87) Mohtasebi, A.; Chowdhury, T.; Hsu, L. H. H.; Biesinger, M. C.; Kruse, P. Interfacial

Charge Transfer between Phenyl-Capped Aniline Tetramer Films and Iron Oxide Surfaces. *J. Phys. Chem. C* **2016**, *120* (51), 29248–29263.

(88) Chowdhury, T.; Mohtasebi, A.; Kruse, P. Nature of the Interaction of N , N ′-Diphenyl-1,4-Benzoquinonediimine with Iron Oxide Surfaces and Its Mobility on the Same Surfaces. *J. Phys. Chem. C* **2017**, *121* (4), 2294–2302.

(89) Sun, W.; Wang, Y.; Lu, Y.; Hu, A.; Shi, F.; Sun, Z. High Sensitive Simultaneously Electrochemical Detection of Hydroquinone and Catechol with a Poly(crystal Violet) Functionalized Graphene Modified Carbon Ionic Liquid Electrode. *Sensors Actuators B Chem.* **2013**, *188*, 564–570.

(90) Tang, J.; Jin, B. Poly (Crystal Violet) - Multi-Walled Carbon Nanotubes Modified Electrode for Electroanalytical Determination of Luteolin. *J. Electroanal. Chem.* **2016**, *780* (Complete), 46–52.

(91) Shao, Z.; Rannou, P.; Sadki, S.; Fey, N.; Lindsay, D. M.; Faul, C. F. J. Delineating Poly(Aniline) Redox Chemistry by Using Tailored Oligo(Aryleneamine)s: Towards Oligo(Aniline)-Based Organic Semiconductors with Tunable Optoelectronic Properties. *Chem. - A Eur. J.* **2011**, *17* (44), 12512–12521.

(92) Gou, P.; Kraut, N. D.; Feigel, I. M.; Bai, H.; Morgan, G. J.; Chen, Y.; Tang, Y.; Bocan, K.; Stachel, J.; Berger, L.; et al. Carbon Nanotube Chemiresistor for Wireless pH Sensing. *Sci. Rep.* **2014**, *4*, 4468.

(93) Copeland, A.; Lytle, D. A. Measuring the Oxidation-Reduction Potential of

Important Oxidants in Drinking Water. *Journal - American Water Works Association*. 2014, pp E10–E20.

APPENDIX 1: STANDARD OPERATING PROCEDURE FOR SENSOR FABRICATION

(The Appendix 1 is reprinted from the work of Dr. Aditya Aryasomayajula with his permission.)

8.1.1. Materials required:

- 3M sheet (#M, product # 9795R)
- Kapton double-sided adhesive roll (2-mil Polyimide (Kapton) Tape Silicone Adhesive Double-Sided) Caplinq, Product # PIT2SD/50.8
- 75 mm x 25 mm frosted glass slides (Corning® Frosted End, One Side, 75 x 25mm) TedPella, Product # 26003
- Deluxe diamond scribing pen, TedPella, Product # 54468
- PDMS and curing agent (Dow Corning, Sylgard 184 silicone elastomer kit)
- 1.5 mm biopsy punch (TedPella product # 15110-15)
- Carbon nanotubes (CNI, Grade/Lot # P0343)
- Tubing (Cole Palmer item # 0641731)
- Petri dish with lid, glass pipette, cotton sticks, scalpel, tweezers.

8.1.2. Equipment required:

- Cricut explore one machine (www.cricut.com)

- PVD sputtering machine (Torr international)
- Desiccator (Bel art products)
- Vacuum pump (Marathon electric, G588DX)
- Hot plate/oven (Corning PC-620-D)

8.1.3. Fabrication steps:

1. **Cutting electrode mask**

   Step 1: Upload image of the electrode mask in www.cricut.com

   Step 2: Load the 3M sheet on the loading paper.

   Step 3: Cut the design on the 3M sheet using Cricut machine.

   The tolerance of cutting machine is within 0.25 mm of the dimensions.

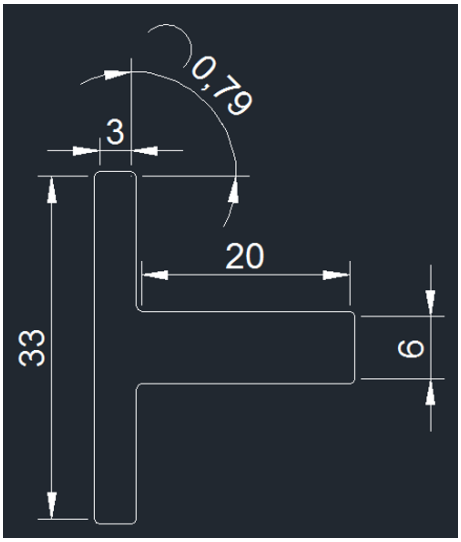

Design with dimensions for electrode mask (all dimensions in mm).

2. **Cutting adhesive channel**

Step 1: Upload image of the adhesive channel in www.cricut.com

Step 2: Load Kapton double sided tape on the loading paper.

Step 3: Cut the design on the Kapton tape using Cricut machine.

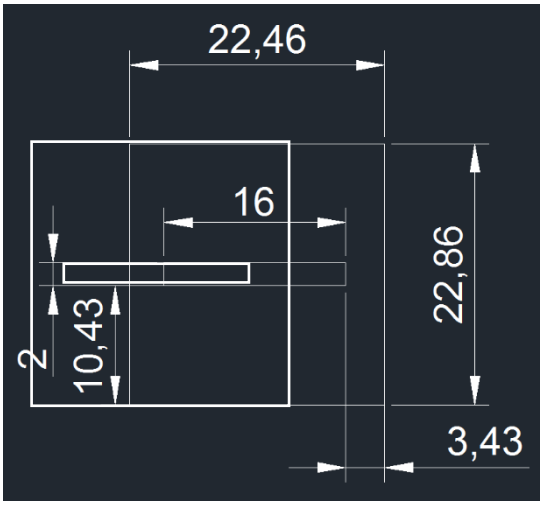

Design with dimensions for Kapton double sided adhesive tape (all dimensions in mm).

3. **Glass slides**

Step 1: Cut 30 x 25 mm on the frosted side of a glass slide as shown in figure 1.

Step 2: Clean the glass slide using ethanol.

Step 3: Bond the electrode mask to the glass slide as shown in figure 2.

Step 4: Make sure the edges are covered by the adhesive tape.

Step 5: Store the glass slides in a petri dish with a sealed lid to avoid any dust.

a)

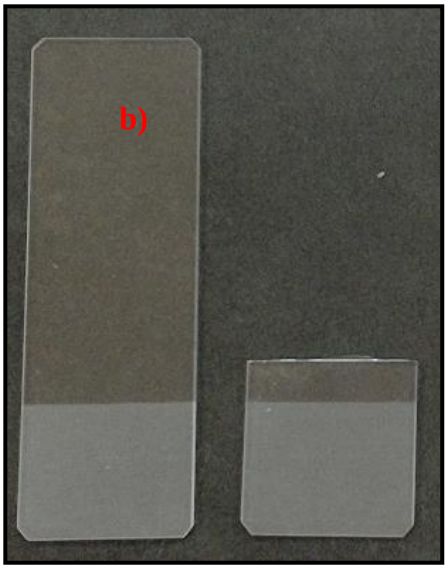

Figure 1: Frosted glass slides (a) before and (b) after cutting.

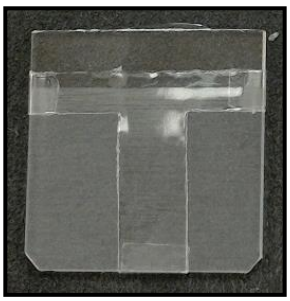

Figure 2: Frosted glass slide bonded to the electrode mask.

4. Electrode sputtering

Step 1: Deposit Chromium at 90 W and 20 SCCM argon gas for a thickness of 200 nm.

Step 2: Deposit Gold at 60 W and 20 SCCM argon gas for a thickness of 2000 nm.

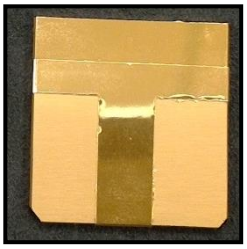

5. PDMS preparation

Step 1: Mix 25 gms of PDMS and 2.5 gms of curing agent in a plastic bowl.

Step 2: Place it in a vacuum desiccator for 10 mins.

Step 3: Pour 25 grams of PDMS mixture into the mold.

Step 4: Place the mold in the oven at 65 °C for 4 hours.

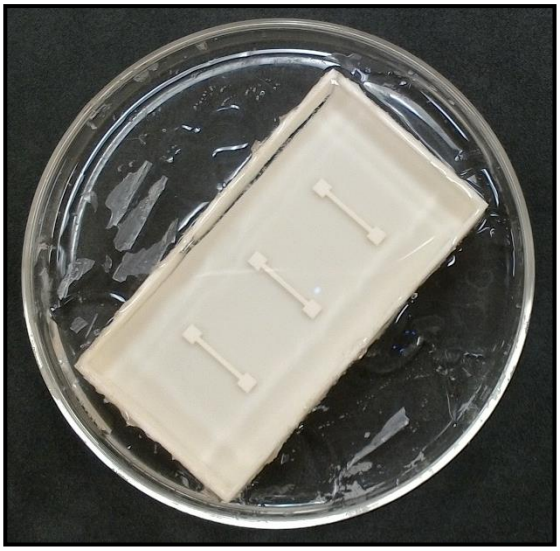

3D printed mold with cured PDMS.

6. Microfluidic chip fabrication

Step 1: Cut 25 mm x 25 mm PDMS blocks from the cured mold such that the microfluidic channel is aligned at the center of the block.

Step 2: Using 1.5 mm biopsy punch holes for inlet and outlet in the PDMS chip.

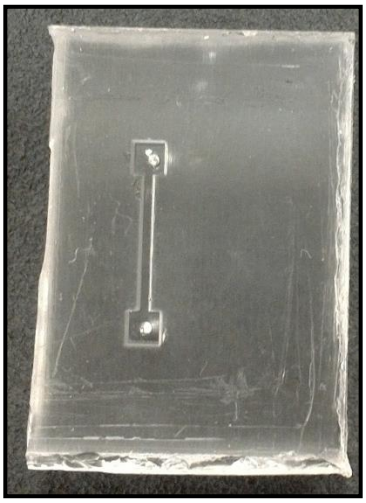

Cut PDMS microfluidic chip with holes punched in the inlet and outlet.

7. Carbon nanotube preparation

Step 1: Take 5 grams of single wall carbon nanotube powder and mix it in 20 ml of methanol.

Step 2: Sonicate the CNT-methanol mixture in a water bath for 30 minutes.

Step 3: Wait for at least 1 hour for the CNT to settle down before using.

8. Carbon nanotube (CNT) deposition

Step 1: Remove the 3M adhesive to expose the electrodes.

Step 2: Using the glass pipette suck 30 ml of CNTs and methanol mixture.

Step 3: Slowly drag the pipette releasing drops of CNT and methanol mixture to form a line between the two gold electrodes.

Step 4: Wait for few seconds for the methanol to evaporate.

Step 5: Repeat step 3 two or three times until a thick layer of CNT forms like a bridge between the electrodes.

Step 6: Wait for 5-10 minutes for the methanol to completely dry out.

Step 7: Using a standard multimeter, measure the resistance between the two gold electrodes.

Step 8: If the resistance is more than 400 Ohms repeat steps 3 to 7 again. The accepted resistance value is between 150 and 250 Ohms.

Step 9: Use a cotton stick to clean the scattered CNTs from the glass surface so that the CNTs are deposited in a neat line.

9. Assembling the device

Step 1: Peel one side of the Kapton adhesive tape and attach it to the bottom of the PDMS chip such that the channel is aligned inside the groove of the adhesive.

Step 2: Apply hand pressure all over the PDMS chip to ensure good bonding of adhesive and PDMS chip.

Step 3: Peel the bottom of the adhesive tape and carefully place the PDMS chip on top of the glass slide such that the channel is aligned in between the gold electrodes and

there is at least a 5 mm gap between the PDMS chip and the bottom edge of the gold electrodes.

Step 4: Apply medium pressure all over the PDMS chip to ensure good bonding between the Kapton tape and glass slide.

Step 5: Use a multimeter to measure the resistance between the two gold electrodes. It should not be more than 300 Ohms. If the resistance is in kiloohms discard the chip.

APPENDIX 2: STANDARD OPERATING PROCEDURE FOR SENSOR MEASUREMENT

9.1.1. Materials and Equipment

1. Polytetrafluoroethylene (PTTF) Tubing
2. 10 ml Syringe
3. Needle
4. 50 ml Centrifuge tube
5. Syringe pump
6. Keithley 2450 SourceMeter
7. Phenyl Capped Aniline Tetramer (PCAT) solution in methanol
8. Sodium Hypochlorite solution reagent grade, available chlorine 10-15% (Sigma-Aldrich)
9. Methanol solvent

9.1.2. Sensor Preparation:

Step 1: Measure and record the resistance of carbon nanotubes film using a multimeter. The resistance of carbon nanotube films may change after placing the tape and PDMS microchannel. The purpose of this step is to characterize the sensor.

Step 2: Take two pieces of PTTF tubing and cut in a way so that it has a sharp cone at the end. It will be easier to attach to the PDMS microchannel. Attach an inlet and an

outlet tube to the sensor using a tweezer. PDMS is may tear due to excessive pressure. Take extra care.

Step 3: Attach a needle to the inlet of the PTTF tube. Inserting needle tip will be enough. Take extra care while handling sharps.

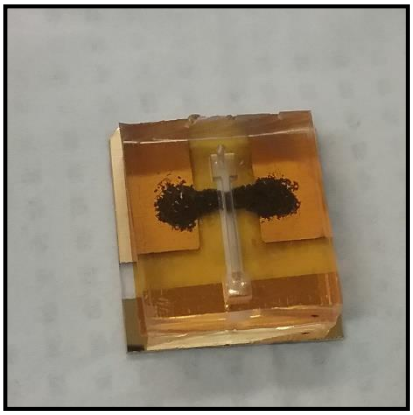

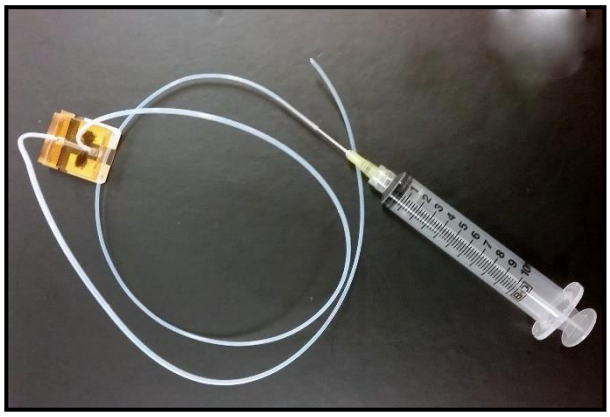

Figure: Bare Sensor and Sensor with tubing and analyte syringe

Step 4: Set the sensor in a fixed position. You can use stand and clamp to set the sensor like shown in the picture below.

Step 5: Load about 10 ml methanol into a syringe and attach it to the inlet of the sensor.

Step 6: Set the analyte syringe into your syringe pump. Follow the instructions provided by syringe pump manufacturer to set the syringe into the pump.

Figure: Sensor set onto a stand

Step 7: Attach the two test lead clips to the two gold electrodes connected by carbon nanotube films.

Step 8: Plug the test lead set into FORCE HI and FORCE LO at the front panel of your Keithley 2450 SMU and turn on the Keithley. You can also use a tri-axial cable to connect to the rear panel of your SMU. In that case, follow the instructions given with the SMU.

Step 9: Turn on the syringe pump and set the flow rate at 0.2 ml/min and volume at 10ml. You may set a different volume following the requirement of your experiment, but the recommended flow rate is 0.2 ml/min. Once you set the conditions, run your syringe pump. Also, put a beaker at the outlet of your sensor to collect the effluents from the sensor.

Step 10: Check the sensor for any leakage. If there is a leakage at any of the inlet or outlet joint, put some PDMS to block the leakage and leave the sensor until the PDMS cures. It will be better to take leakage preventive steps while fabricating the sensor. When you are going to attach the PTTF tube to the PDMS microchannel, it's better to seal your joint with some PDMS.

Step 11: While running the methanol, record the conductivity data measurement for the methanol rinse. Follow the data acquisition procedure at the end of this SOP. Run about 4-5ml methanol to clean the sensor.

Step 12: Load 10 ml PCAT solution into another syringe and replace the methanol solution syringe with PCAT solution. Run PCAT solution and record the data following the data acquisition procedure. Run the PCAT solution until the conductivity measurement gives a stable current value or a decrease in a stable slope (in this case run PCAT solution at least for 20 min).

Step 13: Replace the PCAT solution syringe with a methanol syringe and run about 4-5ml methanol again to rinse any extra PCAT deposited onto the nanotube film. Record the conductivity measurement data following the data acquisition procedure.

Step 14: Load DI water into a new syringe and replace the methanol syringe with DI water. The conductivity should increase with DI water. Run the DI water to get a stable base line or current increase with a constant slope (In this case run at least 10ml DI water). Don't forget to record the measurement data.

At this point, you will have a sensor that is programmed with PCAT and ready to test with your desired analyte solution. For a test, you can run 1ppm of free chlorine solution and record the conductivity data measurement.

9.1.3. Data acquisition

Step 1: Set the measurement parameters on Keithley:

1. Go to **Menu** (physical button on the left-hand side of the touchscreen)>**Quickset** (under the Source and Measure column, shown in the picture below)> Set Function to SrcV MeasI, Set Resolution 5 readings/s. Click on **Power Supply**, Set Source **voltage** to **5mV**, **Maximum allowed source current** to **0.1A** and **2-wire sense** mode.

Figure 97: Keithley 2450 SourceMeter user interface

2. Go to **Menu** > **Graph** (under the Views column) to see the data recording. There will be too many data points and the graph will look a little bit messy due to the high signal to noise ratio. To reduce the noise, you will need to set optimal integration value and filter parameters.

3. To set integration, go to **Menu**> **Settings** (under the Measure column)> Set **NPLCs** (upper corner of the right side of screen) to **10**

4. To add filter, go to **Menu> Calculations>** Set **Filter** to **On**> **Config**, set filter type **Repeat**, Filter count to **3**

5. Go to **Menu**> **Graph** to see the real-time data measurement, data should look less noisy. To delete the noisy data from the graph, Go to **Reading Buffers** (under the measure column) and press **Clear.** New data acquisition will start from this point.

Step 2: Once the measurement is done save the data into a USB key. Go **Menu**> **Reading buffers** > **Save to USB**